Inkjet Printed Energy Storage Systems for Electrochemical Testing and *In-Situ* TEM Analysis

A thesis presented to the University of Dublin, Trinity College for the degree of
Doctor of Philosophy in Physics

By

Lorcan McKeon

Under the supervision of Prof. Valeria Nicolosi

2019

Declaration

I declare that this thesis has not been submitted as an exercise for a degree at this or any other university and it is entirely my own work.

I agree to deposit this thesis in the University's open access institutional repository or allow the library to do so on my behalf, subject to Irish Copyright Legislation and Trinity College Library conditions of use and acknowledgement.

Lorcan McKeon, January 2019

It's still magic, even if you know how it's done.

-Terry Pratchett

Abstract

Understanding of how materials store charge in supercapacitor and battery systems is fundamental to improving these classes of energy storage devices. While materials can be analysed and examined before they are incorporated into a device and again after they have been cycled, this leaves a large gap in the intervening period during which many assumptions about the function of the device must be made. *In-situ* TEM analysis of materials is a technique that could allow for the accurate imaging of materials in this intervening stage, directly visualising the chemical and physical changes that occur in supercapacitor and battery electrodes as they charge and discharge.

In this work, a robust, rapid and accurate method of fabricating microelectrodes for *in-situ* TEM study is presented. Inkjet printing is used to deposit discrete lines of material from solution processed nanomaterial inks. The characteristic coffee staining effect that is observed in the patterns produced by drying droplets is utilised to deposit narrow paths of material along a pre-fabricated metallic electrode. These lines can be reliably printed repeatably with ≈10 µm accuracy. Initial in situ tests were conducted with a single MnO_2-graphene electrode, which stores charge in a pseudocapacitive manner. When this electrode was immersed in aqueous electrolyte, and cycled with typical MnO_2 cycling parameters, dendritic formations were observed through the liquid growing outwards from the electrode edge.

Following on from these initial tests, Si nanoparticles, a battery anode which displays a large volumetric change during its lithiation process, were then deposited. These electrodes were deposited in the same manner, utilising inkjet printing, along with a counter electrode of $LiFePO_4$. The particles were observed during their cycling process through STEM imaging, successfully resolving individual nanoparticles at the metallic electrode edge through the liquid electrolyte layer. Due to electrolyte beam degradation, an electrolyte study was conducted, settling on a 0.1 M $LiClO_4$ in EC:DMC as an appropriate electrolyte for long term study.

The final section of the work sought to utilise the same methods of deposition and the same methods of ink synthesis, Liquid Phase Exfoliation, to fabricate larger

scale flexible devices. A MXene material, $Ti_2C_3T_X$ in a variety of organic solvents was used as a base printing ink. Using these inks, planar supercapacitors were printed onto a flexible coated PET substrate. No further treatment of fabrication processes were required after the initial printing, apart from the drop casting of gel electrolytes. These devices showed excellent charge storage ability, with the NMP based ink printed to 25 print passes displaying an areal capacitance of 12mF cm^{-2} and the onset of resistive behaviour was not observed until a scan rate of 500 mV s^{-1} was reached. These devices were then integrated into larger systems, with devices printed in both series and parallel showing higher voltage capabilities and current responses respectively.

In summary, this work intends to show inkjet printing as robust deposition platform, capable of creating micron accurate TEM samples, and using the same materials and techniques, larger scale flexible integrated circuitry. This allows for the same materials to be used in both processes allowing for a full characterisation of the material on a nanoscale, which can then be deposited into a working device.

Acknowledgements

First and foremost, I would like to thank my supervisor Prof. Valeria Nicolosi for offering me the wonderful opportunity of working as a part of her research group for the past 4 years. I would to specifically thank her for being as supportive as you could hope a supervisor to be, from the very first day to the very last. On both a personal and professional level I must sincerely thank Dr. Joao Coelho, who offered help and advice on every aspect of this work. No question or idea I had was ever too stupid and he kept patience with me for all this time. He has shown a dedication and diligence to not only his own work but to that of others that has helped more than just myself over the last four years. I would like to thank the following people with whom I worked very closely and without whom this work would not be possible; Dr. Edmund Long, who really laid the foundations of the in-situ work presented in this thesis and was instrumental in achieving the first breakthroughs of imaging cycling materials through liquid, Richard Coull for showing me the ropes on printing and always being there to answer any questions I had, Dr John CF Zhang, who drove the project relating to MXene printing, synthesised all MXene inks and never allowed me to get lazy or complacent, Dr Sang Hoon Park for assisting in the initial electrochemistry tests, Oskar Ronan for the electrolyte synthesis and imaging of Si Nanoparticles, Dr. Matthias Kremer for numerous discussions on printing techniques, devices, methods of thickness measurement and football, and finally Dr Sonia Metel for assisting a physicist in a chemistry lab any time I needed it and for making me fear the game of Ludo.

On a personal level I would like to thank my parents, Marie and John, who have stood by me throughout my education and supported me every step of the way. I am eternally grateful for everything you have done for me I have no doubt that I would never have reached this stage without the care and support you have provided. I would like to thank my girlfriend Aisling for supporting me and putting up with me through the entirety of this process. Everything you have done, from our trips away to calls in the evening, have made this process even more enjoyable and I am eternally grateful to my much smarter and cooler best friend.

Finally, I would like to thank the friends in the office and in CRANN that have shared this journey with me. While nobody could say we got more work done by sitting together, we certainly had fun.

Publications

Papers

Chuanfang (John) Zhang, **Lorcan McKeon**, Matthias P. Kremer, Sang-Hoon Park,Oskar Ronan, Andrés Seral-Ascaso, Sebastian Barwich, Cormac Ó Coileáin, Niall McEvoy, Hannah C. Nerl, Babak Anasori, Jonathan N. Coleman, Yury Gogotsi and Valeria Nicolosi. *Additive-free MXene inks and direct printing of micro-supercapacitors* (Submitted for publication)

Conference Posters and Talks

Lorcan McKeon, Edmund Long, João Coelho, Chuanfang Zhang, Sang Hoon Park, Richard Coull, Aleksey Shmelov, Valeria Nicolosi, *In-Situ TEM Analysis of Ink-Jet Printed MnO_2-Graphene for Supercapacitor Electrodes*, (Poster) ECS Prime 2016, Honolulu, Hawaii, USA

Lorcan McKeon, João Coelho, Edmund Long, Oskar Ronan, Chuanfang (John) Zhang, Valeria Nicolosi, *Inkjet Printed Energy Storage Systems for Electrochemical Testing and In Situ TEM Analysis* (Presentation), MRS Fall Meeting 2017, Boston, MA, USA

Contents

Table of Figures

Chapter 1: Introduction and Basic Theory

1.1: Introduction and Motivation

Energy has been the prime concern of technology and innovation in the modern era. Beginning with steam powered engines, continuing with the internal combustion engines of the 20th century, atomic energy and nuclear power in the mid to late 20th century and now the move towards green and renewable systems- energy, its production and its storage, has been at the forefront of human technological innovation[1]. This process has primarily been driven by new materials. Coal drove the pumps and engines of the mines and ships of the steam age[2,3], followed by the oil fuelled 20th century, and these have given way to the silicon-based computer age. It is not a leap to state that the age of renewable energy harvesting and storage will be an age of nano-materials, just as much as the Industrial Revolution was an age of coal.

With the effects of fossils fuels and pollution on the planet becoming more evident with each passing year,[4] cleaner energy alternatives are not just desirable - they are an absolute necessity. Alongside this, the base demand for energy storage systems has increased astronomically. While often decried as a buzzword, the Internet of Things (IoT) is a reality that we now live in. Small, internet-connected electronics surround us; smartphones are now ubiquitous, with Ericsson predicting there being 7.2 billion smartphones in the market by 2023.[5] Internet connected smartwatches are increasingly common[6] as are smaller internet-enabled fitness trackers[7]. In reality, technology has moved past the internet of things, and into the realm of the Internet of Everything (IoE) where increasingly products outside traditional consumer electronics will have basic internet functionality. Clothing and product packaging are widely seen as being the next groups of products to contain internet-connected electronics.[8–14] These new connected devices must be powered, however it is clear that the secondary Li^+ ion battery used in a smartphone is impractical for use in food packaging or in clothing. As such, new kinds of storage systems must be designed that are simultaneously smaller, more flexible, and more efficient, with an

awareness of the potential environmental impact the materials used to fabricate the devices may have. The problem is twofold; increasing the absolute number of devices powered, while also increasing the efficiency of energy use.

It is not just small consumer items that require improved energy storage systems. Renewable energy sources now make up an increasingly large share of generated power with 17% of the consumer energy in the European Union in 2016 coming from renewable sources[15] and in the same year almost two thirds of new power-generating infrastructure constructed worldwide (~165 GW) being renewable power generation.[16] Renewable energy sources are both intermittent and decentralised, with solar power generation being particularly affected by intermittency. There is no way to avoid the simple fact that most energy is generated from these sources during the day when power use is lower.

The decentralised nature of this kind of power generation also means that often the power is being generated in the same location where it is needed, separate from larger grid infrastructure. This energy requires on-site storage unless large scale changes are made to how energy grids operate. Supercapacitors, which excel at rapidly charging and discharging energy stored and have very long theoretical lifetimes, are widely seen as being key in overcoming these fundamental limitations with renewable power.[17–19] Nano-materials have the potential to revolutionise the way that energy is harvested and stored. Fine control over the atomic structure, and thus the electronic and physical behaviours of small particles, provides scientists with an invaluable tool for improving the way that technology uses and stores energy.

A range of materials have been investigated in recent years such as graphene[20,21], MnO_2 [22–25]and Mxenes[26–29] for supercapacitor electrodes, and materials such as Si nanoparticles and nanowires have been presented as viable alternative to the now ubiquitous graphite anodes found in Li ion batteries.[30–35] These materials have impressive energy storage capabilities with certain MnO_2-Graphene hybrids displaying a capacitance of 217 F g^{-1}.[36] Many of these materials have been combined as part of composite electrodes, either for mechanical stability as is the case for Si nanowires and nanoparticles, or to provide desired electronic properties as is the case for graphene or CNT- MnO_2 electrodes. If the energy densities, power densities and lifetimes of these materials are to be fully realised, how they perform as part of

composite electrodes and as part of full energy storage devices must be fully understood.

Since the first TEM was developed in 1931[37], electron microscopy has become the standard method of analysing the structure of materials at the nano-scale. With the development of more advanced detectors and spectroscopy suites,[38] a comprehensive range of physical and chemical characterisation is available for materials at the nano scale. However, these tests are performed at what might be considered "ideal" conditions; in the high vacuum of the TEM column, with few other particles around to interfere and no external stimuli (apart from the electron beam, which is not negligible[39–41]). While important and fundamental chemical and morphological information about these materials can be obtained from standard TEM, they are of limited value for the next step in the development cycle, when these materials or indeed when composites consisting of multiple nano-materials, are combined and used as electrodes in energy storage devices. The interaction of these materials with each other, metallic electrodes and with liquid electrolytes creates a system that cannot be fully understood from simply observing what the material looks like before it is deposited. *Post-mortem* studies can reveal some of this information, however it is still incapable of fully showing the exact process that occurs during the charge-discharge process. For example, *post-mortem* study only has the capability of showing the final state of the material. How these materials store energy, change and potentially degrade is vital to their development as feasible materials for commercial devices and so *post-mortem* testing is insufficient for a comprehensive analysis. *In-situ* testing of materials is the ideal situation to analyse the intermediate stage that cannot be probed by conventional microscopy techniques.

In-situ testing (also referred to as *operando testing*) is the real time measurement of a material or system as a stimulus is applied within the system, or from an external source. A simple example is the heating of particles to observe the dynamics of annealing processes.[42,43] *In-situ* Raman spectroscopy and *in-situ* AFM have been possible for a number of years,[44–48] however the recent development of commercial *in-situ* TEM holders have opened up electron microscopy as a method of *in-situ* analysis. Heating holders, standard liquid holders and liquid electrochemistry holders are now available, allowing for the combination of the imaging, diffraction analysis and spectroscopy analyses available within the TEM with the induced

heated or liquid environments that materials may experience in devices. Liquid cell electrochemistry is the analysis method that will be demonstrated in this work.

This technique allows for the imaging of materials immersed in liquid, while simultaneously subjecting these materials to voltage sweeps from an external voltage source. This allows for an imitation of the conditions that materials may experience during the cycling process. This level of analysis is vital, particularly in regards to how these materials fail and degrade. The dynamics and kinetics of material failure is one of the most important factors in increasing efficiency of batteries and supercapacitors. We must first know how these materials fail and degrade, and why, in order to improve them and ultimately make better devices.

In order to fully analyse and characterise materials with *in-situ* TEM testing, it is essential that we understand on a fundamental level how. In addition, it is also vital to understand what makes these nanomaterials desirable to use as energy storage media in the first place. Knowing why nanomaterials can be more efficient than their bulk counterparts is important to improving both the materials and the devices as a whole. The next section aims to explain firstly how the devices in this work function, and secondly the physical and electronic properties of the nanomaterials that are used. This information is fundamental to fully utilising *in-situ* TEM imaging and electrochemistry.

1.2 Energy Storage Devices

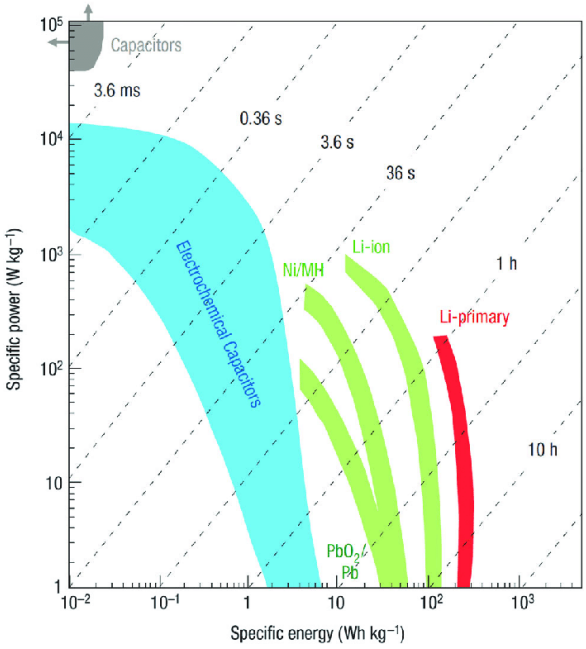

Figure 1.1: A Ragone Plot plotting specific power (or power density) versus specific energy (or specific energy). The coloured regions indicate the specific power and energy domains with which kinds of energy storage devices operate. Adapted with permission from Ref (49).

Commercial energy storage devices can broadly be characterised by how they store energy, be it through lithium ion intercalation, alloying or double layer formation, how much energy they can store (energy density), and how fast they can deliver and gather that energy (power density). A Ragone Plot (shown in figure 2.1)[49] is the traditionally used method of visualising the comparison between different types of energy storage systems.

The relative amount of energy that a device can store and the time it takes to discharge that energy is clear from the Ragone plot. For example, simple electrical computer switches fall in the capacitor section of the top left-hand side of the graph, having a tiny specific energy, but being able to charge and discharge rapidly. The state of the art Li ion batteries have a specific energy in the area of ≈ 150 Wh kg^{-1}.[50] The intermediate range of this graph is occupied by the devices known as Electrochemical Capacitors, variously also referred to as supercapacitors or ultracapacitors. These devices are of significant interest due to their very high

specific power, which results in far faster charging times than more conventional forms of energy storage.[51]

With further development, electrochemical capacitors and Li ion batteries can be seen to be complimentary technologies, with electrochemical capacitors providing rapid charging in situations where Li ion technology is unsuited (such as energy reclamation in car or train braking systems)[52]. Conversely Li ion provide larger power stores in situations where charging times are not of a concern, but energy density is. The following section will detail the operating theory of both kinds of devices.

1.2.1 Electrochemical capacitors and the Electrochemical Double Layer

Fundamentally an electrochemical capacitor consists of two electrodes separated by an ion-conducting dielectric, the electrolyte, and a non-conductive, ion-permeable membrane. The electrolytes used in these devices can be aqueous[53], organic[54,55] or ionic liquids[56,57] and may be found in a liquid, solid or semi-solid gel-like state[58,59]. Figure 1.2 shows the basic schematic of a typical electrochemical capacitor.[60]

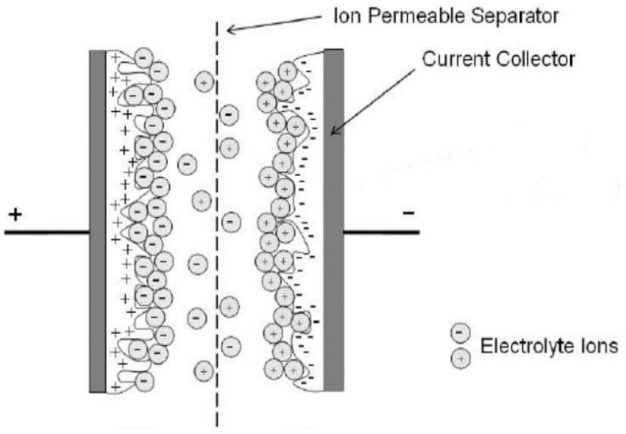

Figure 1.2: Schematic diagram of a typical electrochemical capacitor. Adapted from Ref (60).

The energy stored in an electrochemical capacitor is given by the equation: [61]

$$E = \frac{1}{2}CV^2 \tag{1.1}$$

Where E is the energy density of the system, C is the capacitance of the device and V is the operating voltage of the device.[61] In this case the C value will be largely

determined by the double layer, and V, the operating voltage will be determined by the properties of the electrolyte used in the system, as discussed later.

An electrochemical capacitor stores energy through the action of an electrochemical double layer at the electrode/electrolyte interface. Hermann von Helmholtz first described the phenomenon where an interface is formed when an electrical conductor (electrode) comes into contact with an ionic conductor (electrolyte)[62]. When the electrical conductor is charged, positive and negative ionic charges from the electrolyte accumulate at the Electrode/Electrolyte interface. The capacitance of an electrochemical double layer as described by Helmholtz is given by Equation (1.2); [51]

$$C = \frac{\epsilon_r \, \epsilon_o A}{d} \tag{1.2}$$

Where C is the capacitance of the double layer, ϵ_r is the dielectric constant of the electrolyte, ϵ_o is the dielectric constant of free space, A is the total surface area of the double layer, and d is the thickness of the double layer.[51] Key to this storage method is the fact that the mechanism is electrostatic, not chemical. No chemical changes occur within either the electrode or the electrolyte due to this charge or discharge.

This basic theory presented by Helmholtz in 1853 has been iterated upon numerous times since its first introduction, most notably by Gouy and Chapman, in 1910 and 1913 respectively,[63–65] Stern in 1924,[66] and there have been numerous contributions by B.E Conway,[62,67] Taken together, these theoretical refinements and iterations provide us with the overview of the electrochemical double layer given in Figure 1.3.[68]

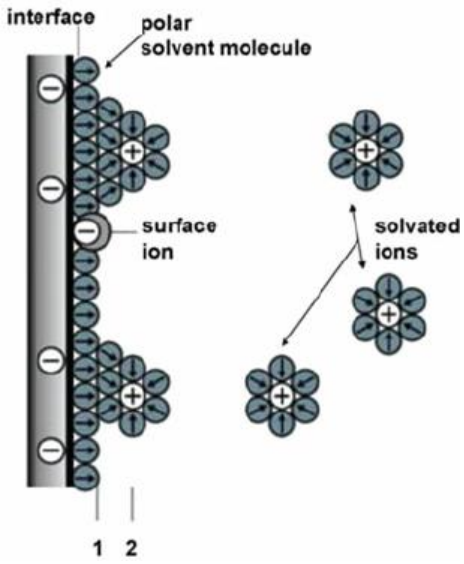

Figure 1.3: The Electrode/Electrolyte Interface with 1 demarcating the Inner Helmholtz Plane and 2 demarcating the Outer Helmholtz Plane. Adapted from Ref (68)

This combined model presents several distinct parts and contributions to the overall capacitance of the double layer. Gouy and Chapman proposed the concept of a diffuse model of charge storage, where Maxwell-Boltzmann statistics can be applied.[69,70] Stern integrated this model into the conventional Helmholtz model, resulting in the total capacitance of the layer being given by Equation (1.3)[62];

$$\frac{1}{C} = \frac{1}{C_{Diff}} + \frac{1}{C_{DL}} \tag{1.3}$$

Where C is the total capacitance of the system, C_{Diff} is the capacitance of the diffuse layer and C_{DL} is the capacitance of the double layer.

Most of the surface of the electrode is occupied by aligned solvent molecules, but also may contain ions that have lost their solvation shell and become directly adsorbed to the surface.[71] This is the inner helmholtz plane (IHP). The next layer consists of solvated ions drawn to the charged electrode and is known as the Outer Helmholtz Plane (OHP). Finally, we have an outer diffuse layer of solvated ions.

While most electrochemical double layers store their energy in the manner described above, some store energy in a fundamentally different way. In pseudocapacitance situations, the applied potential induces a Faradic response in the electrode

material. This response can take the form of electrosorption, intercalation or redox reactions.[72,73] The electrosorption method of pseudocapacitance functions by a two dimensional deposition (sometimes referred to a as an Underpotential Deposition, or UPD) of metals and/or adatoms onto the electrode.[74,75] Pseudocapacitance can occur due to ions intercalating and de-intercalating within the crystal lattice structure of the electrode. This process is distinct from the process upon which Li ion battery technology works due to the fact that there is no phase change involved in the process.[29,72,76] Finally, this pseudocapacitance can occur as a result of rapid redox reactions within the electrode. This behaviour has been seen to occur in a range of Transition Metal Oxides (TMOs), most notably in RuO_2, MnO_2, TiO_2 and conducting polymers.[77,78] The theoretical pseudocapacitance contribution for metal oxides can be calculated by[79]

$$C = \frac{n * F}{M * V} \tag{1.4}$$

Where C is the Capacitance, n is the number of electrons transferred during the redox reaction, F is Faraday's constant, M is the Molar Mass of the electrode material and V is the operating voltage window the device has been charged at.[79] Almost all pseudocapacitors will have both a Double Layer capacitance contributing to the overall capacitance in addition to the faradaic contributions, although in most cases this Double Layer contribution will be miniscule in comparison to the full pseudocapacitance contribution.

Key to the overall capacitance of a device utilising electrochemical double layers are the thickness of the double layer (t) and the surface area of the electrode (A) as shown in Equation 1.2. The thickness of the double layer is the distance from the electrode surface to the Outer Helmholtz Plane. This space is small, consisting only of polarised solvent molecules and the layer of solvated ions which have been drawn to the electrode (typically, t≈1 nm). With t representing the charge separation distance, the primary avenue available to improving supercapacitor performance lies within maximising A, the available surface area for electrolyte ions to occupy. Many layered, two-dimensional nanomaterials have been found to have exceedingly high specific surface areas. Graphene has a theoretical specific surface area of ≈2620 m^2 /g when sheets have been completely isolated and exfoliated.[80] Coupled with their

varied electrical properties, this presents nanomaterials as prime candidates for increasing the capacitance of double layer capacitors.

While for the most part regular electrochemical double layer capacitors and pseudocapacitors can be considered equivalent in terms of their capacitive contribution to a device, a key difference between them lies in the total number of charge and discharge cycles that they can sustain. Due to their electrostatic nature, double layer capacitors can sustain very high numbers of cycles, from 100000 to upwards of 10^6 cycles.[62] Pseudocapacitors do not attain this same long life cycle due to the charge storage mechanism being chemical rather than physical. While the rapid redox processes occurring in pseudocapacitors are in general thermodynamically reversible, there can be irreversible chemical reactions over prolonged cycling which in turn results in less material available for use in redox reactions and so a diminishing capacitance.[81,82]

The performance of electrochemical capacitors is further determined by the type of electrolyte that is used in the system. Electrolytes can be aqueous, organic or (less commonly) ionic. The choice of electrolyte will affect the operating voltage window of the system, which following the square power term in the equation will greatly affect the total energy density of the final device. As shown previously in Equation 1.1, the total energy stored in an electrochemical capacitor is determined chiefly by the capacitance and the voltage range the device is used at. The main concerns for electrolyte selection are stability and ionic conductivity. Aqueous electrolytes tend to be highly conductive, but are primarily limited due to their low operating voltage window of approximately 1 V.[83,84] This low voltage is due to the low thermodynamic stability of water molecules within the electrolyte.[85]

Organic electrolytes tend to have a higher stable voltage window[54] and therefore a higher total energy density, but lower ionic conductivity. Most organic electrolytes consist of a salt dissolved in either acetonitrile[86] or propylene carbonate[87] solvents . Acetonitrile, however, is highly flammable and propylene carbonate has been found to be quite sensitive to temperature variations.[85,86,88] These properties that are common in organic solvents make them unsuitable when a more robust device is required.

1.2.2 Lithium Ion Batteries

A battery is a device consisting of one, or a number of cells that convert chemical energy into electrical energy. The high energy density of these devices has led to their ubiquity in the consumer electronics industry. Commercial Li ion batteries were first developed by Sony in the 1980's, after years of development in the field of primary, non-rechargeable batteries such as Ni-Cd and lead acid[89,90]. They are widely regarded as being the keystone in modern, post-fossil fuel energy systems. An extraordinarily large body of research has been undertaken in recent years to elevate Li^+ ion batteries to a point where they can be used in a practical manner in larger electric systems such as Plug-in and hybrid electric vehicles and for energy grid storage. For Li ion based storage systems to be feasible for use in these larger applications, costs must be lowered, capacity retention must be increased and the efficiency of the device as a whole must be increased.[91–93] As renewable energy forms an increasingly large share of how we meet our domestic energy needs, energy storage becomes an increasingly important issue.

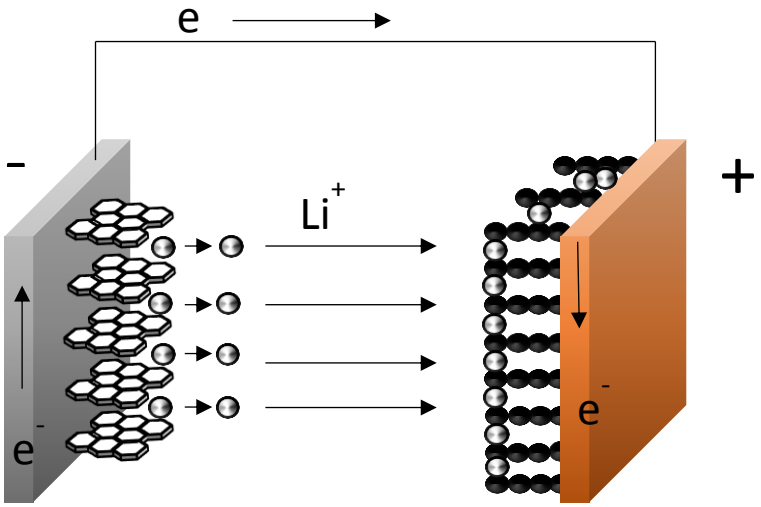

Figure 1.4: A schematic diagram of a conventional Li ion battery showing the discharge cycle, with Li ions returning to the cathode.

A Li ion battery is an asymmetric device, that is, the cathode and anode materials are different. For the cathode material, a Lithium metal oxide (LMO) is usually used, and the anode is a high surface area material that provides intercalation sites, such as graphite.[94–96] The electrodes are immersed in a Li ion conducting electrolyte,

which is traditionally a solution consisting of a lithium salt dissolved in an organic solvent. $LiPF_6$, $LiClO_4$ and $LiAsF_6$ are common salts, with Ethylene Carbonate (EC), Propylene Carbonate (PC), Dimethoxyethane (DME), and Dimethyl Carbonate (DMC) are common solvents.[97,98] Figure 1.4 gives the schematic of what could be considered a typical commercial Li ion battery system utilising an intercalation anode.

As the device charges, Li ions migrate from the lithium metal oxide cathode to the intercalation sites in the anode. When the device discharges, the ions de-intercalate from the anode and migrate back to the metal oxide. This is a diffusion limited process, so in these devices materials with efficient and rapid diffusion pathways are desirable.

A range of electrode materials and electrolytes are available and are used in the construction for Li^+ ion batteries. Each anode-electrolyte-cathode selection will provide a unique lithiation charge storage mechanism, resulting in a very deep well of potential research into possible working combinations. A sample reaction is given below, for a Lithium Metal Oxide ($LiMO_2$) cathode and carbon anode with $LiPF_6$ salt mixed into Ethylene Carbonate–Dimethyl Carbonate (EC-DMC) solvent.[95]

$$yC + LiMO_2 \leftrightarrows Li_xC_y + Li_{(1-x)}MO_2 \tag{1.5}$$

Where $x = 0.5$, $y = 6$ and the operating voltage of the device is 3.7 V.[95]

Lithium Ion Batteries store energy in a manner that looks familiar when compared with the charge storage mechanisms of pseudocapacitors and where one begins and the other ends has been hotly debated within the academic community for quite some time. For the purposes of this work, the dividing line between what constitutes pseudocapacitor behaviour and what constitutes battery behaviour will be given below. These definitions are based mainly on work by Brousse,[99] in turn based on the work of Conway,[62] and by Simon and Gogotsi.[100]

In a pseudocapacitor, the device undergoes a rapid redox reaction at the surface, with one electrode reducing and the other oxidising. While charge is passing across the double layer, similar to the process in a battery, the exchange of electrons is between the electrode and the electrolyte and so the electrons themselves need not pass the entire distance between one electrode and the other. Brousse makes the argument that the key defining factor in what makes a pseudocapacitor is that it mimics capacitance as described by Conway; that is, it exhibits a linear dependence

of stored charge with of the given voltage window, but arises not from electrostatic interactions but from other Faradic reaction mechanisms.[62,99] Using our previously detailed definition for capacitance from Equation 1.1, we can see in Equation 1.6 that the charge stored in a super or pseudo capacitor should remain constant over a given voltage window[99]

$$\Delta Q = C * \Delta V \tag{1.6}$$

Where ΔQ is the charge stored, C is the capacitance of the electrode and ΔV is the voltage window used. When this equation is differentiated with respect to time, we are given the relationship between current and voltage for a supercapacitor[89]

$$i = C\frac{dV}{dt} \tag{1.7}$$

Where i is the current, C is the capacitance and V is the voltage of the capacitor.[89] These two equations provide us with a fundamental framework to describe capacitive behaviour and differentiate it from other charge storage behaviours.

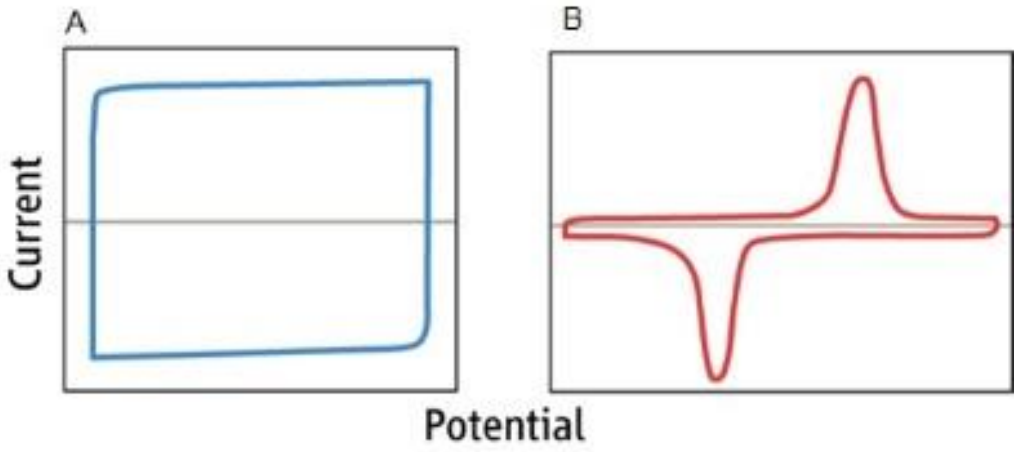

Figure 1.5: A sample CV curve for (A) a supercapacitive material and (B) a battery material. The linear response to rate of change of voltage can be seen in (A) and the characteristic redox peaks with a significant voltage gap of battery materials can be seen in (B). Adapted from Ref (100)

A comparison between the CV curves distinguishing capacitor and battery materials is shown in Figure 1.5. As can be seen from CV curves A, the charge stored in a device will be constant for a given voltage window, and the current will exhibit

a linear response to the rate of change of that voltage.[62,89,99,100]

The relationship showing the constant current response in reaction to a constant rate of change can clearly be seen in Figure 1.5 (A), and is clearly not the case for Figure 1.5 (B). In addition, when the area below the curves is integrated providing the charge, it is clear that the stored charge is not constant across the entirety of the voltage window in (B), again breaking one of our defined conditions for capacitive behaviour.

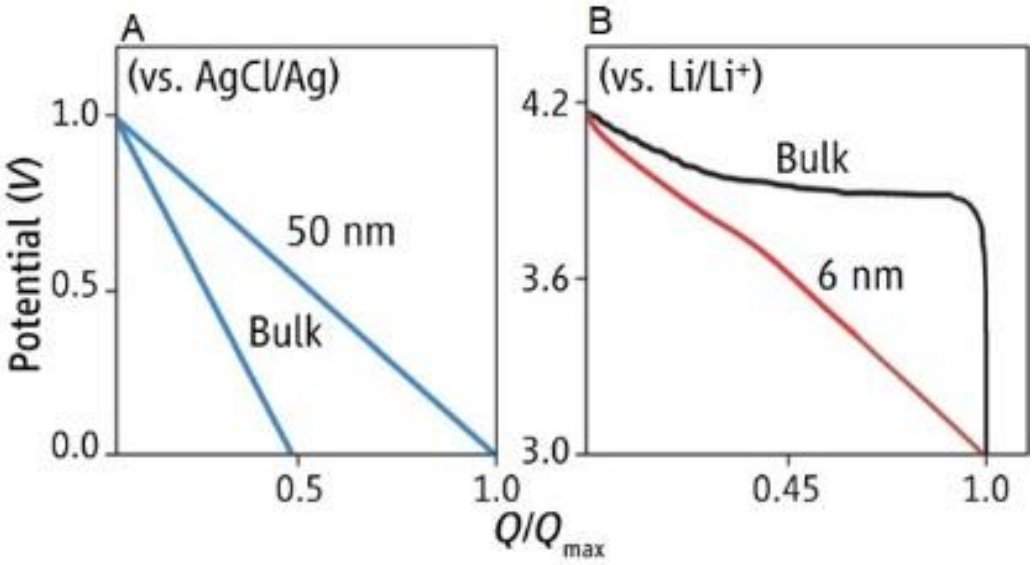

Figure 1.6: Characteristic Galvanostatic profiles for pseudocapacitive materials (A) and battery materials (B). The Pseudocapacitive materials exhibit a linear response at all crystallite length scales, which is not the case for the Battery materials shown in (B). This shows the need for the definitions of "intrinsic" and "extrinsic" capacitance. Adapted from Ref (100)

The clear-cut definitions by which we determine capacitance from battery storage begin to break down when we examine the two types of devices in the galvanostatic regime, i.e. under constant current conditions. When supercapacitive material is analysed under constant current charging and discharging, i.e. Galvanostatic conditions, the response from a supercapacitive material is linear. However, Li ion battery materials exhibit a flat voltage plateau in the Galvanostatic profile, indication a phase change is occurring. This phase change occurs throughout the electrode and is believed to be a diffusion limited process.

It is well documented that as the electrode itself becomes thinner, the diffusion lengths that the Li^+ ions are required to move are then decreased.[101,102] As the

electrode size decreases, the characteristic voltage plateau is seen to diminish until finally a critical size is reached in which the linear response is observed. For the sample shown in Figure 1.6 (B) this critical size is 6 nm. When this critical size is reached, almost all of the Li^+ ion intercalation is occurring on the surface of the electrode, as there is no longer any bulk to diffuse through. In this case the battery reactions will closely resemble pseudocapacitance. At this point it is necessary to introduce another condition that will define the behaviour of the two kinds of energy storage, that of either intrinsic or extrinsic pseudocapacitance.

For intrinsic pseudocapacitive materials, the pseudocapacitive effect is an intrinsic material property; it can be observed at all times in a functional device. For materials that we term "extrinsic" pseudocapacitors, the effect is not an intrinsic property of the material, it is only obtained after external modification of the material, such as creating a nano-scale electrode architecture.

A clear definition of the operating principles of these devices is vital to a comprehensive experimental analysis of the materials used. Having a clear idea of the expected range of power and energy densities of a set of materials is fundamental to designing experiments that can give genuine insight into how these materials can be improved.

1.3 Electrode materials for energy storage devices

In this section the various materials that are to be used throughout the following experiments are detailed. This will include a review of both capacitive and battery type materials as well as standard materials that were utilised as simple current collectors. The electrical and mechanical properties will be reviewed where relevant to the scope of this work. Where relevant synthesis will be explained, although most of the exfoliation steps relevant to liquid phase exfoliated materials will be explained in Chapter 2.

1.3.1 Two Dimensional Materials (2D materials)

Nanomaterials are subject of immense interest for increasing the storage abilities of both batteries and supercapacitors. Many nanomaterials show high surface to volume ratios and porosity that theoretically increase their ability to store charge. In addition to this, shorter electrode material length scales result in shorter

diffusion lengths for the ions that store the charge.[77,103–105] One of the most impactful developments in the use of nanomaterials for energy storage technology has been the discovery and practical synthesis of two-dimensional materials. Graphene, which was first experimentally isolated in 2004[106], was the first in what would become a range of 2D materials to be discovered. 2D materials are of interest to researchers in the field of energy storage since they tend to have different and unusual electronic and mechanical properties when compared to their bulk properties. Due to their nature as nanosheets, 2D materials tend to have very high specific surface areas, rendering them particularly useful for use in supercapacitors (according to Equation 1.1 in section 1.2.1) and as Li^+ storing anodes for batteries. In addition, as was discussed in section 1.2.2, materials that in bulk display battery-type behaviour can display supercapacitive behaviour when nano-engineered. A very large number of 2D materials have now been successfully identified and isolated, providing researchers with a large "toolbox" of materials with which to develop the next generation of materials. Materials previously dismissed as being inefficient or unfeasible for use in supercapacitors or batteries are now being investigated once again in their two-dimensional forms. A range of two-dimensional materials were used through the of this work, and the physical and electronic properties that make them relevant for energy storage and interesting for the purposes of in-situ TEM analysis are given in the following pages.

1.3.2 Manganese Dioxide (MnO_2)

The pseudocapacitive material primarily used through the experimentation detailed in this work is Manganese Dioxide (MnO_2). MnO_2 is pseudocapacitive transition metal oxide that has been the subject of intense study over recent years as a replacement material for RuO_2, the traditionally used commercial pseudocapacitive material. MnO_2 has attracted this attention due to its natural abundance[107], low cost[108,109], low toxicity and low environmental impact[110,111] when compared with other Transition Metal oxides, particularly RuO_2. Most importantly from an energy storage point of view is the very high theoretical capacitance the material displays, ~ 1370 F g^{-1}.[23]

MnO_2 has attracted a large attention in no small part due to its interesting crystallographic structure. MnO_2 forms a general group of materials all based upon a base MnO_6 octahedra.[112] These octahedra can share vertices and edges to give a

range of materials with different crystallographic structures and properties. These different structures allow for selective synthesis with an aim towards making the material more amenable towards energy storage. In nature, these octahedral base blocks form tunnel structures that are occupied by other cations, from minerals or water, but with a view towards energy storage, these tunnels are perfect sites for ions during the energy storage process.[23]

In general, for use in an aqueous electrolyte, the charge storage of MnO_2 will occur in the redox between the IV and III oxidation states. This charge storage is as a result of the intercalation of protons (H^+) or alkali metal cations (C^+) into the bulk of the material during oxidation and de-intercalation during reduction.[111]

$$MnO_2 + H^+ + e^- \leftrightarrow MnOOH \quad (1.8)$$

$$MnO_2 + C^+ + e^- \leftrightarrow MnOOC \quad (1.9)$$

Where C represents some kind of electrolyte cation such as K^+, Na^+, or Li^+.[23] The processes described in the above equations refer largely to reactions happening at the surface of the material.[113–115]

One of the traditional roadblocks in utilising MnO_2 as an effective pseudocapacitive material is that it has a very low conductivity. In bulk MnO_2 the conductivity can be anything between 10^{-7} S m^{-1} and 10^{-3} S m^{-1} depending on the crystal structure of the bulk material chosen.[116,117] This low conductivity means that it is only usually surface material that is available to undergo the charge storage process, for the most part the bulk of the material remains unused.[111] This results in a much lower theoretical capacitance when compared the far more conductive RuO_2, and a specific capacitance that dramatically falls off with increasing film thickness. An MnO_2 film between tens and hundreds of nanometres thick would be expected to exhibit a specific capacitance in the range 700 to 1300 F g^{-1}.[118,119] When the films increase in thickness to the micrometre range, the specific capacitance drops to 150 to 250 F g^{-1}. While this is usually seen as a limitation on the use of MnO_2 as a capacitor electrode, with the advent of research into layered 2D materials, it has once again been brought to the forefront.

2D sheets of MnO_2, like all 2D materials when compared to their bulk, have an incredibly high specific surface area. A higher specific surface area will provide more locations for the faradic charge transfer required for pseudocapacitance to occur. It is therefore hoped that 2D layered MnO_2 will provide the means to overcome the fundamentally limiting factor of low conductivity and increase the overall utilisation of the active material.

1.3.3 MXenes

MXenes are a new class of two-dimensional inorganic compounds first discovered and isolated in 2011. MXenes begin as a $M_{n+1}AX_n$ phase, where *M* is an early Transition Metal (Ti, V, Nb, Ta)[120,121] *A* is an A group element (such as Al, Ga, Si or Ge)[29] usually taken from groups 13 or 14, and *X* is either C or N.[122] The MX phases are very chemically stable; however, the A phase is not, affording an opportunity to modify the structure by removing the A phase from the structure. Unlike the weak interlayer Van der Waals bonds of graphene for example, the M-A and A-X bonds are relatively strong, so simple mechanical exfoliation is not appropriate.[27] The primary method that has been reliably used is to etch the bulk material using HF. A simple series of reactions given below was the first reported method of isolating the MX phases from the A phase[122]

$$Ti_3AlC_2 + 3HF = AlF_3 + 3/2H_2 + Ti_3C_2 \quad (1.10)$$

$$Ti_3C_2 + 2H_2O = Ti_3C_2(OH)_2 + H_2 \quad (1.11)$$

$$Ti_3C_2 + 2HF = Ti_3C_2F_2 + H_2 \quad (1.12)$$

By this process a number of different MXene types can be synthesised such as Ti_2C, Ta_4C_3, Ti_3CN.[123] After the wet etching step, the material is usually sonicated to delaminate the Mxenes, resulting in suspensions consisting of single flakes in solvent. Some alternative delamination steps have been investigated such as pH level alterations followed by simple hand shaking of the dispersion.[124] Some synthesis with no delamination step has also been reported.[125]

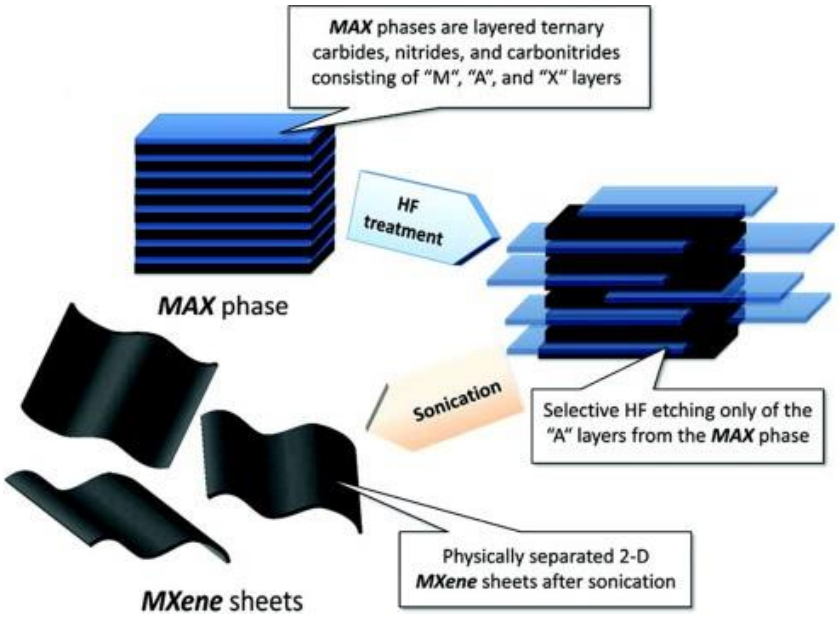

Figure 1.7: Processing and synthesis of MXene nanosheets. Some publications (as referenced above) have reported higher quality MXenes by limiting the intensity of the delamination step. Others have found etching methods that do not require delamination due to the intercalation that occurs during etching. Adapted from Ref (121)

When MXenes are synthesised using an acidic-fluoride containing solution, they will have a mix of -O, -OH and -F terminations[28] These surface terminations change how the end material will behave, with different preparation methods producing MXenes that range from metallic to semi-conducting.[28] As is the case with most nanosheet materials, sheets with fewer defects and larger flake size will result in material exhibiting a higher conductivity.

MXenes are of interest to researchers in the field of energy storage for largely the same reason graphene is. MXenes represent a broad class of nanosheets that exhibit high specific surface area and high conductivity, the two main parameters that are sought after for supercapacitor electrodes (As described in section 1.2.1 previously). Ti_3C_2 has been found to exhibit volumetric capacitances of up to 900 F cm^{-3}.[29,122] The material itself $Ti_3C_2T_x$ (T_x representing the surface termination) has been to exhibit standalone pseudocapacitance depending on the type of electrolytes used. Simple double layer capacitance is observed when cycled using $(NH_4)_2SO_4$. However, the observed capacitance is much higher when the same material was tested with H_2SO_4. This was attributed to pseudocapacitive redox reactions occurring involving the bonding of Hydronium in the electrolyte to the O terminating the $Ti_3C_2T_x$. The bonding occurs during the charge cycle, with the hydronium debonding during the

discharge cycle. This changes the oxidation state of the Ti[126], allowing for a further method of energy storage when the device is engineered in this particular manner.

Due to its layered nature, it is also of interest as an anode material in Li^+ ion batteries for its large number of available intercalation sites.[127,128] In addition MXene surfaces are chemically active and so have potential for use in Hybrid devices with one electrode consisting of a battery like material and the other consisting of a supercapacitive material.[29] Hybridisation of the material itself has also been investigated with materials such as Reduced Graphene Oxide (RGO)[129] and Carbon Nanotubes (CNTs).[130] These hybridisations serve to increase conductivity, provide mechanical stability to the layers and to increase the interlayer spacing, improving electrolyte accessibility and preventing restacking of the delaminated layers.[130]

MXenes have also been shown to be stable in a range of solvents, including many commonly used organic solvents including Dimethylformamide (DMF), Dimethyl Sulfoxide (DMSO), Ethanol and N-Methyl-2-pyrrolidone (NMP) but also importantly in water.[131] This solvent stability presents a unique opportunity for these materials to be utilised in a variety of deposition systems such as ultrasonic spray deposition, inkjet printing, and aerosol jet printing.

1.3.3 Carbon Nanotubes (CNTs)

Carbon nanotubes are one dimensional allotrope of Carbon that are identified by their cylindrical nanostructure. Depending on their physical structure, CNTs can be metallic, semi-metallic or semiconducting. A seamless defect free carbon nanotube consists of a rolled sheet of carbon sp^2 bonded forming a hexagonal lattice that is open at both ends.[132] This cylinder can consist of a single sheet or rolled carbon, a Single Walled Nanotube (SWNT) or can consist of multiple concentric rolled sheets, a Multiwalled Nanotube (MWNT). While the existence of CNTs, then known as carbon filaments, was first reported in 1952[133] and variously re-reported again over the years leading up to the early 1990's[134]. Interest in the material took hold with confirmed isolation and measurement of SWNTs in 1993[135,136] and since then an enormous body of research has focussed on the material.[137–141]

CNTs are useful for their nature as both a metallic and a semiconducting material, depending on the structure. The nature of a CNT will be controlled by the chiral vector. This represents how the sheet of carbon has been rolled to form the tube

itself. The chiral vector is usually represented with a pair of integers n and m which represent the possibilities in the structure of the rolled tube. The diameter, d_t, of the rolled tube can be related to the chiral vector by, [142]

$$d_t = \frac{0.246}{\pi}\sqrt{n^2 + nm + m^2} \tag{1.13}$$

where 0.246 is the unit cell distance in nm.[142]

An m value =0 will result in what is known as a "zig-zag" nanotube and n = m will result in an "armchair" nanotube. Any other combination will result in a chiral nanotube. The formation of the tubes is shown in Figure 1.8.

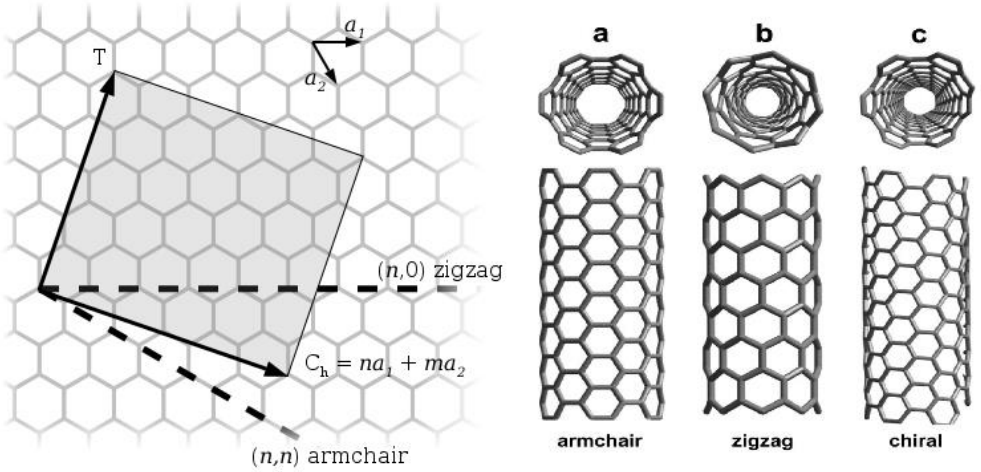

Figure 1.8: Carbon sheets rolled to form different forms of CNTs. The effect of chiral vector and angle on the structure of the final tube. Right, three types of CNTs possible from different chiral vectors. Adapted from Ref (139).

The electronic transport properties of CNTs are found to be heavily dependent on their structure. In general, it has been found that all armchair type CNTs are metallic. In addition to this, any zigzag CNTs with m and n values that occur in multiples of threes are also metallic. This can be generalised by Equation 1.12[142]

$$\frac{2m + n}{3} = integer \tag{1.14}$$

It is interesting that the change between metallic behaviour and semiconducting behaviour occurs with no difference in the strength of the chemical bonds and no

doping or impurities are added. The only change is how the chiral vector effects the band structure of the tube[132].

CNTs are of great interest in the field of flexible and printed electronics due to their high conductivity and their high tensile strength. This combination of properties has led to them being used as a standalone electrode material, but also as an additive to other materials that have low conductivity or structures that require extra mechanical strength.[143–145]

1.3.4 Graphene

Graphene is a allotrope of carbon that consists of an sheet of sp^2 bonded carbon atoms arranged in a hexagonal lattice that is a single atom thick which was originally experimentally isolated in 2004,[106] and the discovery of which was awarded the Nobel Prize for Physics in 2010. Key to the definition of graphene is that it is sufficiently isolated from the environment around it to be considered free standing.[146] Bulk graphite, from which graphene is derived is characterised by the very strong in-plane sp^2 bonds and the very weak inter-plane van der Waals bonds. This interplane weakness allows for monolayers to be separated from the bulk.

Graphene has been the subject of an enormous amount of research since its discovery for a variety of reasons relating to its odd and impressive properties; electrical, optical, mechanical and thermal. Graphene is a zero-bandgap semiconductor that displays electron mobilities of up to 15,000 $cm^2 V^{-1} s^{-1}$ at ambient temperatures.[147,148] Electrons propagating through the structure of a graphene layer lose their effective mass, and behave in a manner more suitable to be described by a Dirac-like equation rather than the standard Schrödinger equation.[147,149,150] These "massless" electrons are often described as massless Dirac Fermions.[147] These electronic properties arise due to the material's unique crystal structure. The graphene lattice is composed of two separate sublattices.[151] The energy bands of these sublattices intersect at the edges of the Brillouin Zone at Dirac points K and K'. At the Dirac points, the valence and conduction bands of converge to form what is known as a Dirac cone. (Shown in Figure 1.9) It is at these Dirac points that the charge carriers behave as massless Dirac Fermions, as described before. The presence of the Dirac fermions as charge carriers result in ballistic transport over

sub-micron distances, and are the primary source of the high carrier mobilities measured in graphene samples.[147,151,152]

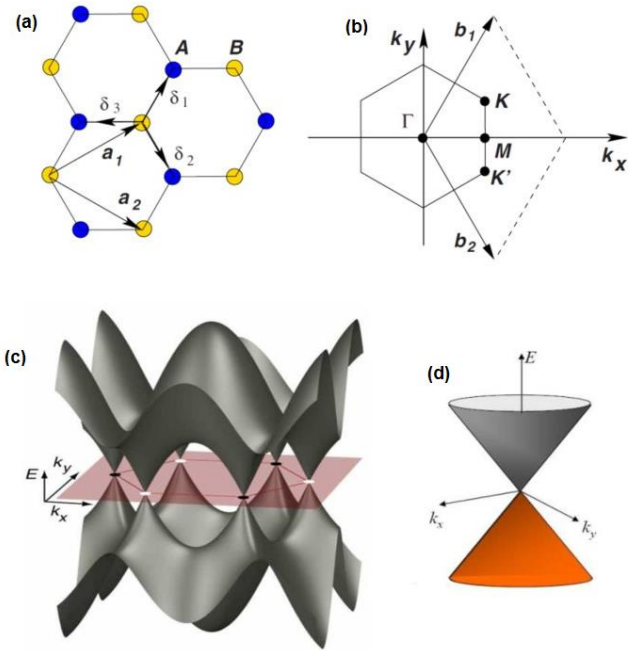

Figure 1.9: The crystal structure and resulting electronic properties of Graphene. The crystal structure of graphene is shown in (a) with the triangular sub lattices denoted by A and B. a_1 and a_2 are the lattice unit vectors. The corresponding Brillouin Zone is shown in (b) with the Dirac points located at K and K'. The electronic dispersion of the Brillouin Zone is shown in (c), the six points where the bands intersect are the Dirac points. The red plane represents the Fermi Energy. A zoomed in image of the Dirac points is shown in (d), showing the characteristic "Dirac Cone" (a) and (b) adapted from Ref (150), (c) and (d) adapted from Ref (151)

While it is primarily the electronic properties of graphene that are of interest in this work, it is still necessary to note the other properties the material displays. Monolayer graphene displays an optical absorption of ≈ 2.3%,[153,154] a remarkably high absorbance despite only being a single atom thick. Graphene also exhibits a high mechanical strength with a reported Young's modulus of 1 TPa and a failure strain of up to 12%.[155] These mechanical properties have positioned graphene as an extremely attractive additive not just for mechanical strength but in particular to materials that require both mechanical stability and conductivity, a particular concern in the field of flexible electronics and for energy storage materials that undergo mechanical deformation as they charge and discharge such as Si.[156–158]

Graphene exhibits a very high thermal conductivity(~ 3000 W m^{-1} K^{-1} for free standing graphene)[159], another feature which makes it particularly attractive for electronics where the dissipation of heat away from devices and parts is always a

concern. The high thermal conductivity of graphene allows for it to be used in higher power devices than other, less thermally conductive materials.

Due to the fact that graphene is a two-dimensional material it also exhibits a very large specific surface area, reported to be 2630 m^2 g^{-1}. [80] While the specific advantages of a material with very high specific surface area in relation to energy storage devices has been discussed previously, it also can be used for a number of other processes, such as gas and chemical sensing.[160–163]

A final note to the attractive nature of graphene for future electronics is its environmental impact. Graphene is simply single atomic layers of carbon. It does not require intensive or dangerous synthesis processes and can be produced from very commonly found materials.[164] As electronics are increasingly designed with a view on minimising the environmental impact of their production, use and eventual disposal, it is preferable that devices are manufactured from materials such as graphene that have a lessened environmental impact in their synthesis and disposal than materials used in older electronics.

1.3.5 Si Nanoparticles

Silicon has been one of the prime candidate materials to replace graphite as the standard anode material for next generation Li ion secondary batteries for quite some time. This is almost entirely due to Si's massive theoretical capacitance (3500 mA h g^{-1} compared to 372 mA h g^{-1}compared to a graphite anode).[33,34,165] Despite this high theoretical capacitance, bulk Si and Si particles on the micrometre scale provide a much lower capacitance than expected (800 mA h^{-1} g^{-1}).[33,166,167] In addition to this, Si based electrodes show huge irreversible capacity loss over multiple cycles.[168] The primary reasons for this low capacitance and poor cyclability are the large volumetric changes Si undergoes during charging and discharging and its inherently low conductivity. Si materials undergo a process of alloying, rather than intercalation, in order to store Li ions during the charge discharge cycle. While this alloying process allows for a far higher amount of lithium ions stored (maximum Li uptake 4.4/1 of Li/Si),[30,167] the Si itself undergoes significant volume changes during the charge-discharge cycle.[168–170] Due to the high amount of Li uptake per Si atom,

volumetric expansions of up to 400% are expected during a charge-discharge cycle.[34,165,171]

This volumetric expansion of Si is the primary contributing factor to the rapid decay of capacitance after the initial charge-discharge cycle. While there are numerous specific consequences of this volumetric expansion and contraction, three of the most destructive results of this process are as follows; firstly the integrity of the electrode structure is severely compromised to the repeated stresses that it is subjected to during these expansion and contraction cycles.[34] The expansion and contraction result in eventual fracturing or pulverisation of the material/electrode inhibiting its ability to store charge.[32,35,172] Secondly, due to this expansion and eventual pulverisation, material disconnects from the current collector. Once material detaches from the electrode it becomes useless and unable to effectively store charge due to silicon's very low bulk conductivity (6.7 x 10^{-4} S m^{-1}).[168,172,173]

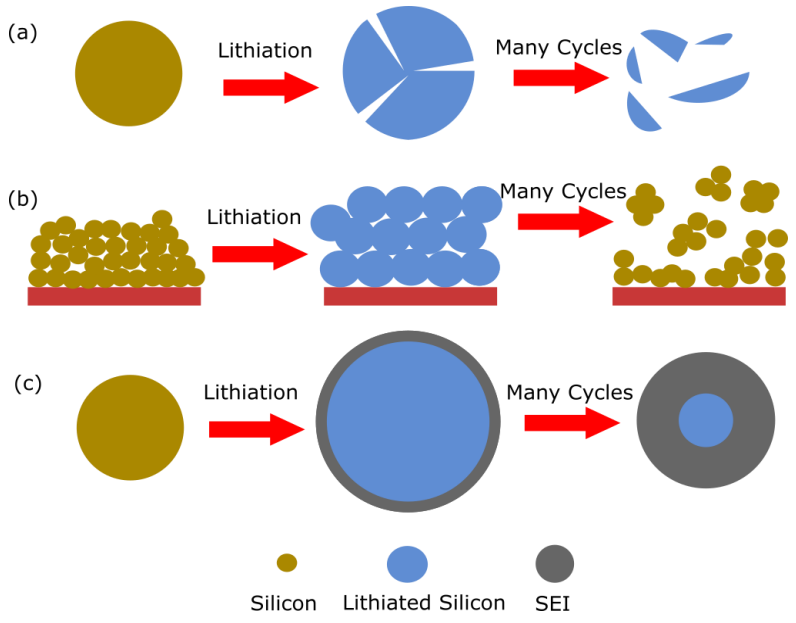

Figure 1.10: The lithiation processes observed in Silicon; (a) the swelling and eventual fracture of Si particles, (b) the swelling and detachment of Si from the current collector and (c) the formation of a thick SEI on lithiating Si.

The third process relates to the repeated formation of the solid electrolyte interphase (SEI). The SEI is an interfacial layer that forms on the anode during the first charge cycle. It is usually composed of a mix of inorganic products that result from the degradation of the electrolyte, and will contain some amount of the Li salt from the electrolyte itself.[174–177] Normally this layer stabilises after the first charge cycle,[175] however this is not the case for Si materials. As the materials swell during the

alloying process of the charging cycle, the SEI that forms at the beginning is fractured and broken. On subsequent cycles, the SEI attempts to reform, only to be disrupted by the continued swelling of the Si. It is important to note that the SEI is not totally destroyed by the swelling, resulting in each alloying cycle producing a thicker and thicker SEI. This constant formation, fracturing and reformation of the SEI consumes solvent and Li from the electrolyte in a non-reversible manner and also serves to limit the overall working surface area of the SI electrode.[34,168,172,174–177] A basic overview of these three processes is given in Figure 1.10.

Research into Si anodes therefore seeks to mitigate and possibly reverse the effects previously described and reach capacitance values much closer to silicon's theoretical maximum with a much higher number of cycles sustained. Very thin films of Si deposited onto porous metallic electrodes have been seen to display improved cycling performance, however the areal capacity of these electrodes is far too low to be of real practical benefit.[170,178] The use of Si nanoparticles and combining Si into a composite with other materials have so far proven to be the most effective way of limiting particle fracture, low electrode conductivity and repeated SEI growth.

One and two-dimensional Si nanoparticles have been seen to have different swelling and fracture dynamics to bulk Si, [32,34,165,179] and size dependent fracture has been an area of considerable interest.[180] Nanowires have been seen to be more resistant to the fracturing seen in bulk Si, due to the small diameter of the nanowire being able to accommodate the volumetric expansion of the lithiation. Nanowires grown directly onto the metallic current collector also display more efficient current carrying pathways, meaning the charge storing material remains in better contact with the electrode during the charge and discharge process. However despite the initial belief that Si nanowires were totally resistant to the fracture observed in bulk and micro-scale Si electrodes, *in-situ* TEM testing has revealed this to not be the case.[181] In addition forests of Si nanowires would have to be grown directly onto metallic substrates in order to ensure they are anchored and in good electrical contact with the current collector. While this is certainly possible, Si nanoparticles usually in the range ≈ 50-100 nm in diameter have been similarly investigated. While the conductivity pathways of an electrode composed on spherical nanoparticles are not as good (relying on the physical contact of the particles compared to the more efficient 1-D pathways of the wires), if particles are small

enough, below 100nm, they have been shown to be very resilient against cracking and fracturing.[182,183]

Si nanoparticles still suffer from poor conductivity and offer a larger available surface area upon which the SEI can form (and eventually fracture and reform). In short, nanowires and nanoparticles solve some of the intrinsic issues that hold Si electrodes back, but not all of them. Combining them with other materials (including novel combinations of Si nanospheres and Si nanowires)[184] has been an effective way to enhance to enhance the cyclability of Si electrodes without compromising their energy storage capabilities. The main material that forms these composites with Si nanostructures are carbon allotropes, with the aim of giving both additional conductivity but also mechanical strength over multiple charge discharge cycles.[185–190] Unfortunately the lithiation dynamics of these complex systems are still poorly understood and so one of the primary aims of the *in-situ* TEM portion of this work is to visualise the initial volumetric expansion of Si nanoparticles in a liquid environment, and then to investigate the effects of various additives such as polymers, binders, carbon black, graphene and CNTs.

1.3.6 Lithium Iron Phosphate ($LiFePO_4$)

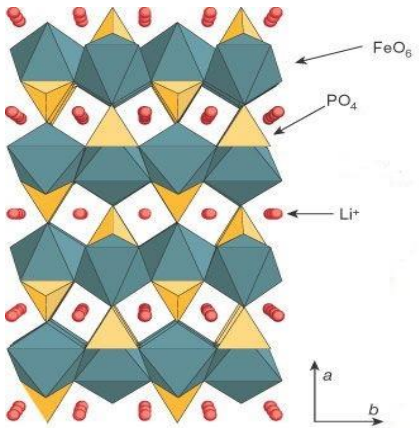

Figure 1.11: The crystal structure of $LiFePO_4$ in projection along [001]. Adapted from Ref (191)

For quite some time $LiCoO_2$ has been the cathode material of choice for small handheld consumer electronics. It has a number of drawbacks that limit its potential use in larger cells, such as those used for renewable energy storage or for plug-in electric vehicles. The specific capacity of $LiCoO_2$ cell is quite low, ≈ 140 mAh g^{-1}, Co itself is not particularly abundant, constituting only about 20ppm in the Earth's crust and additionally Co is quite toxic.[191] $LiFePO_4$ has been suggested as a suitable

cathode material for these kind of energy storage needs. Lithium iron phosphate ($LiFePO_4$) was first proposed as a cathode material for batteries by Goodenough *et al* in 1996,[192] and since then has been the subject of intense research. The olivine structure of the $FePO_4$ allows for a consistently reversible insertion and de-insertion of Li, providing a theoretical capacity of 170 mAh g^{-1}.[90,191,193] The material itself is also non-toxic and the natural abundance of iron results in a low cost.

The crystal structure of $LiFePO_4$ and $FePO_4$ are very similar and the volumetric changes observed during the insertion/de-insertion of the Li ions has been measured to be 6.81%.[191] This small volumetric change and structural similarity give the material excellent electrochemical cyclability. The major drawback to the use of $LiFePO_4$ as a cathode material is its relatively low conductivity, (~ 10^{-9} S cm^{-1}).[90,194] Conductive additives are commonly used to increase the electrochemical capabilities of the material. The most common of these additives is carbon which can produced to coat the material *in-situ* during its synthesis. There are several methods of adding carbon to the material, depending on the chosen method of synthesis, be it solid-state reactions, co-precipitation or spray pyrolysis.[115,195–198]

The many synthesis routes and carbon based additives used are outside the scope of this work, but from a practical point of view the addition of high quality carbon coatings has a very large effect on the performance of $LiFePO_4$ as a cathode material.[191] Relevant to this work is the fact that $LiFePO_4$ that synthesised with carbon shows a decreased final particle size as the carbon acts as a nucleating agent.[191] The small particle size also creates shorter Li diffusion lengths and a larger surface area of the material, allowing for increased contact with the electrolyte. An added benefit of smaller particle size for this work is the advantage of both printing small particles and depositing small particles into liquid TEM cells. Smaller particles mean less agglomeration and clogging during the printing process and reduces window breakages during the assembly of the electrochemical cells to be described in later chapters of this work.

1.4 Outlook and overview

Understanding how batteries and supercapacitors function on a fundamental level is vital for making informed decisions on how to improve their efficiency. Similarly,

understanding the many physical and electric properties of nanomaterials assists us in selecting the correct material to help improve these devices further. This work aims to develop a system whereby liquid cell TEM will allow for materials to be analysed in conditions similar to those found in the internal structure of a battery or supercapacitor. This kind of analysis will give a new, and fundamentally different insight into the behaviour of these devices and materials. Focussed Ion beam and photolithography have been the primary methods used to fabricate cells for in situ TEM up to this point. However, these processes can be limited by materials and may not accurately represent the structure of an electrode as it would be found in a real device. Inkjet printing serves to overcome both limitations.

This chapter aims to provide a theoretical foundation to this work. The principles and materials described here will be found repeatedly through the following chapters.

Chapter 2 aims to broadly describe the experimental methods and techniques used through the experiments that compose this work. Owing to the technical nature of this work and the process development that was required to achieve some of the later results, these methods are vital to the overall conclusions of the work. Where techniques are highly detailed or specific, some methods and techniques are explained further in subsequent chapters.

Chapter 3 details the development of the printing process as it was used for fabricating microelectrodes for use in an *in-situ* TEM holder. Inkjet printing was used to deposit small amounts of material across narrow conductive electrodes with the intention of cycling these electrodes in a liquid environment. Included in this chapter is a full characterisation of how IPA based material inks interact with pre-fabricated SiN_x cells and how the printing process, normally used for creating large macroscale structures ≥ 1mm, was adapted for depositing much smaller electrodes with micron scale accuracy.

Chapter 4 details the process of electrochemical cycling of both supercapacitor and battery materials within the *in-situ* TEM holder. The process of holder assembly and electrode cycling for aqueous electrolytes is described. A sequence of dendritic formation on MnO_2-Graphene electrodes that was observed through liquid is presented. A short study of the beam effects on organic electrolytes is included and the process of imaging printed electrodes through liquid layers and the technical

difficulties of this process are detailed. Finally, the cycling and imaging of two electrode systems consisting of a Si nanoparticle working electrode and a $LiFePO_4$ counter is presented. These cells are then imaged and cycled within the electron microscope. The work presented in chapters 3 and 4 are fundamentally linked and can be considered the core sections of the work.

Chapter 5 details the printing process of flexible supercapacitors. These devices are primarily composed of a single MXene material, $Ti_3C_2T_X$, printed onto a flexible, coated PET sheet. A number of material inks were used, and the effect of device thickness and number of printed passes on the conductivity and charge storing ability of these inks. Some description of multi material electrodes that are used for less conductive materials will also be included in this chapter and how what has been learned from both single material tests and these initial multi-material studies can be implemented to design effective multi-material, flexible supercapacitors.

Chapter 6 will contain a brief summary of the work, the conclusions that can be drawn and the impact of what has been seen. It will also contain an outline of how the work can potentially progress and build upon what this been learned to this point.

Bibliography

1. Smil, V. *Energy in world history*. (Westview Press, 1994).

2. Hills, R. L. *Power from steam : a history of the stationary steam engine*. (Cambridge University Press, 1989). at <https://www.cambridge.org/ie/academic/subjects/general-science/history-science/power-steam-history-stationary-steam-engine?format=PB&isbn=9780521458344>

3. Dickinson, H. W. *A Short History of the Steam Engine*. (Cambridge University Press, 2011). at <https://www.cambridge.org/ie/academic/subjects/engineering/engineering-design-kinematics-and-robotics/short-history-steam-engine?format=PB&isbn=9781108012287>

4. *Climate Change 2013 - The Physical Science Basis*. (Cambridge University Press, 2014). doi:10.1017/CBO9781107415324

5. Ericsson. Ericsson Mobility Report June 2015 - ericsson-mobility-report-june-2015.pdf. *Ericsson* (2015). at <http://www.ericsson.com/res/docs/2015/ericsson-mobility-report-june-2015.pdf>

6. Statistica. • Global smartwatch unit sales 2014-2018 | Statistic. *Statistica* (2018). at <https://www.statista.com/statistics/538237/global-smartwatch-unit-sales/>

7. Fitness & activity tracker - Statistics & Facts | Statista. at <https://www.statista.com/topics/4393/fitness-and-activity-tracker/>

8. Kim, J., Kumar, R., Bandodkar, A. J. & Wang, J. Advanced Materials for Printed Wearable Electrochemical Devices: A Review. *Adv. Electron. Mater.* **3,** 1600260 (2017).

9. Honda, W., Harada, S., Arie, T., Akita, S. & Takei, K. Printed wearable temperature sensor for health monitoring. in *IEEE SENSORS 2014 Proceedings* 2227–2229 (IEEE, 2014). doi:10.1109/ICSENS.2014.6985483

10. Carey, T. *et al.* Fully inkjet-printed two-dimensional material field-effect heterojunctions for wearable and textile electronics. *Nat. Commun.* **8,** 1202 (2017).

11. Ren, J. *et al.* Environmentally-friendly conductive cotton fabric as flexible strain sensor based on hot press reduced graphene oxide. *Carbon N. Y.* **111,** 622–630 (2017).

12. Croux, D. *et al.* Molecular imprinted polymer films on RFID tags: A first step towards disposable packaging sensors. *Phys. Status Solidi Appl. Mater. Sci.* **210,** 938–944 (2013).

13. Duncan, T. V. Applications of nanotechnology in food packaging and food safety: Barrier materials, antimicrobials and sensors. *J. Colloid Interface Sci.* **363,** 1–24 (2011).

14. Kuswandi, B. *et al.* Smart packaging: Sensors for monitoring of food quality and safety. *Sens. Instrum. Food Qual. Saf.* **5,** 137–146 (2011).

15. Eurostat - No defined author. Renewable energy statistics - Statistics Explained. (2016). at <http://ec.europa.eu/eurostat/statistics-explained/index.php/Renewable_energy_statistics>

16. Lewis, N. S. & Nocera, D. G. Powering the planet: Chemical challenges in solar energy utilization. *Proceedings of the National Academy of Sciences* **103,** 15729–15735 (2006).

17. Thounthong, P. Model based-energy control of a solar power plant with a supercapacitor for grid-independent applications. *IEEE Trans. Energy Convers.* **26,** 1210–1218 (2011).

18. Qu, L. & Qiao, W. Constant power control of DFIG wind turbines with supercapacitor energy storage. *IEEE Trans. Ind. Appl.* **47,** 359–367 (2011).

19. Carrasco, J. M. *et al.* Power-electronic systems for the grid integration of renewable energy sources: A survey. *IEEE Trans. Ind. Electron.* **53,** 1002–1016 (2006).

20. Le, L. T., Ervin, M. H., Qiu, H., Fuchs, B. E. & Lee, W. Y. Graphene supercapacitor electrodes fabricated by inkjet printing and thermal reduction of graphene oxide. *Electrochem. commun.* **13,** 355–358 (2011).

21. Zhang, L. L., Zhou, R. & Zhao, X. S. Graphene-based materials as supercapacitor electrodes. *J. Mater. Chem.* **20,** 5983–5992 (2010).

22. Yan, J. *et al.* Fast and reversible surface redox reaction of graphene-MnO2composites as supercapacitor electrodes. *Carbon N. Y.* **48,** 3825–3833 (2010).

23. Dubal, D. P., Chodankar, N. R., Gomez-Romero, P. & Kim, D.-H. in *Metal Oxides in Supercapacitors* 79–98 (Elsevier, 2017). doi:10.1016/B978-0-12-810464-4.00004-8

24. Xu, C., Kang, F., Li, B. & Du, H. Recent progress on manganese dioxide based supercapacitors. *J. Mater. Res.* **25,** 1421–1432 (2010).

25. Coelho, J. *et al.* Manganese oxide nanosheets and a 2D hybrid of graphene-manganese oxide nanosheets synthesized by liquid-phase exfoliation. *2D Mater.* **2,** 025005 (2015).

26. Peng, Y. Y. *et al.* All-MXene (2D titanium carbide) solid-state microsupercapacitors for on-chip energy storage. *Energy Environ. Sci.* **9,** 2847–2854 (2016).

27. Sun, S., Liao, C., Hafez, A. M., Zhu, H. & Wu, S. Two-dimensional MXenes for energy storage. *Chem. Eng. J.* **338,** 27–45 (2018).

28. Anasori, B., Lukatskaya, M. R. & Gogotsi, Y. 2D metal carbides and nitrides (MXenes) for energy storage. *Nat. Rev. Mater.* **2,** 16098 (2017).

29. Lukatskaya, M. R. *et al.* Cation intercalation and high volumetric capacitance of two-dimensional titanium carbide. *Science (80-.).* **341,** 1502–1505 (2013).

30. Besenhard, J. O., Yang, J. & Winter, M. Will advanced lithium-alloy anodes have a chance in lithium-ion batteries? *J. Power Sources* **68,** 87–90 (1997).

31. Yang, J., Winter, M. & Besenhard, J. O. Small particle size multiphase Li-

alloy anodes for lithium-ionbatteries. *Solid State Ionics* **90,** 281–287 (1996).

32. Kasavajjula, U., Wang, C. & Appleby, A. J. Nano- and bulk-silicon-based insertion anodes for lithium-ion secondary cells. *J. Power Sources* **163,** 1003–1039 (2007).

33. Hu, L. *et al.* Si nanoparticle-decorated Si nanowire networks for Li-ion battery anodes. *Chem. Commun.* **47,** 367–369 (2011).

34. Zuo, X., Zhu, J., Müller-Buschbaum, P. & Cheng, Y.-J. Silicon based lithium-ion battery anodes: A chronicle perspective review. *Nano Energy* **31,** 113–143 (2017).

35. Chan, C. K. *et al.* High-performance lithium battery anodes using silicon nanowires. *Nat. Nanotechnol.* **3,** 31–35 (2008).

36. Mendoza-Sánchez, B., Coelho, J., Pokle, A. & Nicolosi, V. A 2D graphene-manganese oxide nanosheet hybrid synthesized by a single step liquid-phase co-exfoliation method for supercapacitor applications. *Electrochim. Acta* **174,** 696–705 (2015).

37. Ruska, E. & Knoll, M. Die magnetische Sammelspule für schnelle Elektronenstrahlen. *Z. Tech. Phys.* **12,** 389 (1931).

38. Egerton, R. Electron energy-loss spectroscopy. *Phys. World* **10,** 47–51 (1997).

39. Smeeton, T. M., Kappers, M. J., Barnard, J. S., Vickers, M. E. & Humphreys, C. J. Electron-beam-induced strain within InGaN quantum wells: False indium 'cluster' detection in the transmission electron microscope. *Appl. Phys. Lett.* **83,** 5419–5421 (2003).

40. Williams, D. B. & Carter, C. B. in *Transmission Electron Microscopy* 53–71 (Springer US, 2009). doi:10.1007/978-0-387-76501-3_4

41. Reyes-Gasga, J. & García-García, R. Analysis of the electron-beam radiation damage of TEM samples in the acceleration energy range from 0.1 to 2MeV using the standard theory for fast electrons. *Radiat. Phys. Chem.* **64,** 359–367 (2002).

42. Simonsen, S. B. *et al.* Direct observations of oxygen-induced platinum nanoparticle ripening studied by in situ TEM. *J. Am. Chem. Soc.* **132,** 7968–7975 (2010).

43. Zink, N. *et al.* In situ heating TEM study of onion-like WS2 and MoS2 nanostructures obtained via MOCVD. *Chem. Mater.* **20,** 65–71 (2008).

44. Cheng, Z. & Liu, M. Characterization of sulfur poisoning of Ni-YSZ anodes for solid oxide fuel cells using in situ Raman microspectroscopy. *Solid State Ionics* **178,** 925–935 (2007).

45. Lucas, I. T., Pollak, E. & Kostecki, R. In situ AFM studies of SEI formation at a Sn electrode. *Electrochem. commun.* **11,** 2157–2160 (2009).

46. Inaba, M. In Situ Raman Study on Electrochemical Li Intercalation into Graphite. *J. Electrochem. Soc.* **142,** 20 (1995).

47. Ramesha, G. K. & Sampath, N. S. Electrochemical reduction of oriented Graphene oxide films: An in situ Raman spectroelectrochemical study. *J. Phys. Chem. C* **113,** 7985–7989 (2009).

48. Beaulieu, L. Y., Hatchard, T. D., Bonakdarpour, A., Fleischauer, M. D. & Dahn, J. R. Reaction of Li with Alloy Thin Films Studied by In Situ AFM. *J. Electrochem. Soc.* **150,** A1457 (2003).

49. Simon, P. & Gogotsi, Y. Materials for electrochemical capacitors. *Nat. Mater.* **7,** 845–854 (2008).

50. Thackeray, M. M., Wolverton, C. & Isaacs, E. D. Electrical energy storage for transportation - Approaching the limits of, and going beyond, lithium-ion batteries. *Energy Environ. Sci.* **5,** 7854–7863 (2012).

51. Kötz, R. & Carlen, M. Principles and applications of electrochemical capacitors. *Electrochim. Acta* **45,** 2483–2498 (2000).

52. Lhomme, W., Delarue, P., Barrade, P., Bouscayrol, A. & Rufer, A. Design and control of a supercapacitor storage system for traction applications. in *Conference Record - IAS Annual Meeting (IEEE Industry Applications Society)* **3,** 2013–2020 (IEEE, 2005).

53. Khomenko, V., Raymundo-Piñero, E., Frackowiak, E. & Béguin, F. High-voltage asymmetric supercapacitors operating in aqueous electrolyte. *Appl. Phys. A Mater. Sci. Process.* **82,** 567–573 (2006).

54. Lewandowski, A., Olejniczak, A., Galinski, M. & Stepniak, I. Performance of carbon-carbon supercapacitors based on organic, aqueous and ionic liquid electrolytes. *J. Power Sources* **195,** 5814–5819 (2010).

55. Morimoto, T., Hiratsuka, K., Sanada, Y. & Kurihara, K. Electric double-layer capacitor using organic electrolyte. *J. Power Sources* **60,** 239–247 (1996).

56. Chen, Y., Zhang, X., Zhang, D., Yu, P. & Ma, Y. High performance supercapacitors based on reduced graphene oxide in aqueous and ionic liquid electrolytes. *Carbon N. Y.* **49,** 573–580 (2011).

57. Balducci, A. *et al.* High temperature carbon-carbon supercapacitor using ionic liquid as electrolyte. *J. Power Sources* **165,** 922–927 (2007).

58. Meng, C., Liu, C., Chen, L., Hu, C. & Fan, S. Highly flexible and all-solid-state paperlike polymer supercapacitors. *Nano Lett.* **10,** 4025–4031 (2010).

59. Kang, Y. J., Chung, H., Han, C. H. & Kim, W. All-solid-state flexible supercapacitors based on papers coated with carbon nanotubes and ionic-liquid-based gel electrolytes. *Nanotechnology* **23,** 065401 (2012).

60. Knight, C., Davidson, J. & Behrens, S. Energy options for wireless sensor nodes. *Sensors* **8,** 8037–8066 (2008).

61. Van Aken, K. L., Beidaghi, M. & Gogotsi, Y. Formulation of ionic-liquid electrolyte to expand the voltage window of supercapacitors. *Angew. Chemie - Int. Ed.* **54,** 4806–4809 (2015).

62. Conway, B. E. *Electrochemical Supercapacitors. Kluwer Academic/Plenum* (Springer US, 1999). doi:10.1007/978-1-4757-3058-6

63. Walbran Sean & Halley J. W. Solid-Liquid Interface Theory. **789,** 10–25 (2001).

64. Chapman, D. L. LI. *A contribution to the theory of electrocapillarity*. *Philos.*

Mag. Ser. 6 **25,** 475–481 (1913).

65. Oldham, K. B. A Gouy-Chapman-Stern model of the double layer at a (metal)/(ionic liquid) interface. *J. Electroanal. Chem.* **613,** 131–138 (2008).

66. Stern, O. Zur Theorie der Elektrolytischen Doppelschicht. *Zeitschrift fur Elektrochemie* **30,** 508–516 (1924).

67. Conway, B. E., Bockris, J. O. M. & Ammar, I. A. The dielectric constant of the solution in the diffuse and Helmholtz double layers at a charged interface in aqueous solution. *Trans. Faraday Soc.* **47,** 756–766 (1951).

68. Klösgen, B., Rümenapp, C. & Gleich, B. in *BetaSys* 241–271 (Springer New York, 2011). doi:10.1007/978-1-4419-6956-9_11

69. Anderson, G. M. Theory of the diffuse double layer in liquids. *J. Chem. Phys.* **40,** 628–633 (1964).

70. Bolt, G. H. Analysis of the validity of the Gouy-Chapman theory of the electric double layer. *J. Colloid Sci.* **10,** 206–218 (1955).

71. Bockris, J. O., Devanathan, M. A. V. & Muller, K. On the Structure of Charged Interfaces. *Proc. R. Soc. A Math. Phys. Eng. Sci.* **274,** 55–79 (1963).

72. Conway, B. E., Birss, V. & Wojtowicz, J. The role and utilization of pseudocapacitance for energy storage by supercapacitors. *J. Power Sources* **66,** 1–14 (1997).

73. Lubimtsev, A. A., Kent, P. R. C., Sumpter, B. G. & Ganesh, P. Understanding the origin of high-rate intercalation pseudocapacitance in Nb2O5 crystals. *J. Mater. Chem. A* **1,** 14951–14956 (2013).

74. Girija, T. C. & Sangaranarayanan, M. V. Underpotential deposition of Tl on Ag in the presence of bromide ions - Estimation of specific capacitance for design of electrochemical supercapacitors. *J. Appl. Electrochem.* **36,** 531–538 (2006).

75. Kolb, D. M., Przasnyski, M. & Gerischer, H. Underpotential deposition of metals and work function differences. *J. Electroanal. Chem.* **54,** 25–38 (1974).

76. Augustyn, V. *et al.* High-rate electrochemical energy storage through Li + intercalation pseudocapacitance. *Nat. Mater.* **12,** 518–522 (2013).

77. Zhao, X., Sánchez, B. M., Dobson, P. J. & Grant, P. S. The role of nanomaterials in redox-based supercapacitors for next generation energy storage devices. *Nanoscale* **3,** 839–855 (2011).

78. Conway, B. E. & Pell, W. G. Double-layer and pseudocapacitance types of electrochemical capacitors and their applications to the development of hybrid devices. *J. Solid State Electrochem.* **7,** 637–644 (2003).

79. Zhi, M., Xiang, C., Li, J., Li, M. & Wu, N. Nanostructured carbon-metal oxide composite electrodes for supercapacitors: A review. *Nanoscale* **5,** 72–88 (2013).

80. Stankovich, S. *et al.* Synthesis of graphene-based nanosheets via chemical reduction of exfoliated graphite oxide. *Carbon N. Y.* **45,** 1558–1565 (2007).

81. Kierzek, K., Frackowiak, E., Lota, G., Gryglewicz, G. & Machnikowski, J. Electrochemical capacitors based on highly porous carbons prepared by KOH activation. *Electrochim. Acta* **49,** 515–523 (2004).

82. Pandolfo, A. G. & Hollenkamp, A. F. Carbon properties and their role in supercapacitors. *J. Power Sources* **157,** 11–27 (2006).

83. Ruiz, V., Santamaría, R., Granda, M. & Blanco, C. Long-term cycling of carbon-based supercapacitors in aqueous media. *Electrochim. Acta* **54,** 4481–4486 (2009).

84. Lehtimäki, S. *et al.* Performance, stability and operation voltage optimization of screen-printed aqueous supercapacitors. *Sci. Rep.* **7,** 46001 (2017).

85. Reber, D., Kühnel, R.-S. & Battaglia, C. High-voltage aqueous supercapacitors based on NaTFSI. *Sustain. Energy Fuels* **1,** 2155–2161 (2017).

86. Arulepp, M. *et al.* Influence of the solvent properties on the characteristics of a double layer capacitor. *J. Power Sources* **133,** 320–328 (2004).

87. Ue, M. Mobility and Ionic Association of Lithium and Quaternary Ammonium Salts in Propylene Carbonate and γ-Butyrolactone. *J. Electrochem. Soc.* **141,** 3336 (1994).

88. Liu, P., Verbrugge, M. & Soukiazian, S. Influence of temperature and electrolyte on the performance of activated-carbon supercapacitors. *J. Power Sources* **156,** 712–718 (2006).

89. Conway, B. E. Transition from "Supercapacitor" to "Battery" Behavior in Electrochemical Energy Storage. *J. Electrochem. Soc.* **138,** 1539 (1991).

90. Li, H., Wang, Z., Chen, L. & Huang, X. Research on advanced materials for Li-ion batteries. *Adv. Mater.* **21,** 4593–4607 (2009).

91. Wood, D. L., Li, J. & Daniel, C. Prospects for reducing the processing cost of lithium ion batteries. *J. Power Sources* **275,** 234–242 (2015).

92. Li, J., Armstrong, B. L., Daniel, C., Kiggans, J. & Wood, D. L. Optimization of multicomponent aqueous suspensions of lithium iron phosphate (LiFePO4) nanoparticles and carbon black for lithium-ion battery cathodes. *J. Colloid Interface Sci.* **405,** 118–124 (2013).

93. Li, J., Daniel, C. & Wood, D. Materials processing for lithium-ion batteries. *J. Power Sources* **196,** 2452–2460 (2011).

94. Megahed, S. & Scrosati, B. Lithium-ion rechargeable batteries. *J. Power Sources* **51,** 79–104 (1994).

95. Scrosati, B. & Garche, J. Lithium batteries: Status, prospects and future. *J. Power Sources* **195,** 2419–2430 (2010).

96. Nitta, N., Wu, F., Lee, J. T. & Yushin, G. Li-ion battery materials: Present and future. *Mater. Today* **18,** 252–264 (2015).

97. Aurbach, D. *et al.* Design of electrolyte solutions for Li and Li-ion batteries: a review. *Electrochim. Acta* **50,** 247–254 (2004).

98. Morita, M., Ishikawa, M. & Matsuda, Y. in *Lithium Ion Batteries* 156–180 (Wiley-VCH Verlag GmbH). doi:10.1002/9783527612000.ch7

99. Brousse, T., Belanger, D. & Long, J. W. To Be or Not To Be Pseudocapacitive? *J. Electrochem. Soc.* **162,** A5185–A5189 (2015).

100. Simon, P., Gogotsi, Y. & Dunn, B. Where do batteries end and supercapacitors begin? *Science (80-.).* **343,** 1210–1211 (2014).

101. Okubo, M. *et al.* Nanosize effect on high-rate Li-ion intercalation in LiCoO2 electrode. *J. Am. Chem. Soc.* **129,** 7444–7452 (2007).

102. Sathiya, M., Prakash, A. S., Ramesha, K., Tarascon, J. M. & Shukla, A. K. V2O5-anchored carbon nanotubes for enhanced electrochemical energy storage. *J. Am. Chem. Soc.* **133,** 16291–16299 (2011).

103. Bruce, P. G., Scrosati, B. & Tarascon, J.-M. Nanomaterials for Rechargeable Lithium Batteries. *Angew. Chemie Int. Ed.* **47,** 2930–2946 (2008).

104. Jiang, C., Hosono, E. & Zhou, H. Nanomaterials for lithium ion batteries. *Nano Today* **1,** 28–33 (2006).

105. Su, X. *et al.* Silicon-Based Nanomaterials for Lithium-Ion Batteries: A Review. *Adv. Energy Mater.* **4,** 1300882 (2014).

106. Novoselov, K. S. *et al.* Electric field in atomically thin carbon films. *Science (80-.).* **306,** 666–669 (2004).

107. Post, J. E. Manganese oxide minerals: Crystal structures and economic and environmental significance. *Proc. Natl. Acad. Sci.* **96,** 3447–3454 (1999).

108. Zheng, J. P. Hydrous Ruthenium Oxide as an Electrode Material for Electrochemical Capacitors. *J. Electrochem. Soc.* **142,** 2699 (1995).

109. Yang, P. *et al.* Low-Cost High-Performance Solid-State Asymmetric Supercapacitors Based on MnO $_2$ Nanowires and Fe $_2$ O $_3$ Nanotubes. *Nano Lett.* **14,** 731–736 (2014).

110. Lee, H. Y., Kim, S. W. & Lee, H. Y. Expansion of Active Site Area and Improvement of Kinetic Reversibility in Electrochemical Pseudocapacitor Electrode. *Electrochem. Solid-State Lett.* **4,** A19 (2001).

111. Toupin, M., Brousse, T. & Bélanger, D. Charge storage mechanism of MnO2 electrode used in aqueous electrochemical capacitor. *Chem. Mater.* **16,** 3184–3190 (2004).

112. Dubal, D. P. & Gomez-Romero, P. *Metal Oxides in Supercapacitors*. (Elsevier, 2017). at <https://www.sciencedirect.com/science/book/9780128111697#book-description>

113. Ghodbane, O., Pascal, J.-L. & Favier, F. Microstructural Effects on Charge-Storage Properties in MnO 2 -Based Electrochemical Supercapacitors. *ACS Appl. Mater. Interfaces* **1,** 1130–1139 (2009).

114. Mao, L., Zhang, K., On Chan, H. S. & Wu, J. Nanostructured MnO 2 /graphene composites for supercapacitor electrodes: the effect of morphology, crystallinity and composition. *J. Mater. Chem.* **22,** 1845–1851 (2012).

115. Yang, M.-R., Teng, T.-H. & Wu, S.-H. LiFePO4/carbon cathode materials prepared by ultrasonic spray pyrolysis. *J. Power Sources* **159,** 307–311 (2006).

116. Augustyn, V., Simon, P. & Dunn, B. Pseudocapacitive oxide materials for high-rate electrochemical energy storage. *Energy Environ. Sci.* **7,** 1597–1614 (2014).

117. Ghodbane, O., Pascal, J. L. & Favier, F. Microstructural effects on charge-storage properties in MnO 2-based electrochemical supercapacitors. *ACS Appl. Mater. Interfaces* **1,** 1130–1139 (2009).

118. Pang, S. C. & Anderson, M. A. Novel electrode materials for electrochemical capacitors: Part II. Material characterization of sol-gel-derived and electrodeposited manganese dioxide thin films. *J. Mater. Res.* **15,** 2096–2106 (2000).

119. Nagarajan, N., Cheong, M. & Zhitomirsky, I. Electrochemical capacitance of MnOx films. *Mater. Chem. Phys.* **103,** 47–53 (2007).

120. Naguib, M., Mochalin, V. N., Barsoum, M. W. & Gogotsi, Y. 25th Anniversary Article: MXenes: A New Family of Two-Dimensional Materials. *Adv. Mater.* **26,** 992–1005 (2014).

121. Naguib, M. *et al.* Two-Dimensional Transition Metal Carbides. *ACS Nano* **6,** 1322–1331 (2012).

122. Naguib, M. *et al.* Two-dimensional nanocrystals produced by exfoliation of Ti3AlC2. *Adv. Mater.* **23,** 4248–4253 (2011).

123. Anasori, B. *et al.* Two-Dimensional, Ordered, Double Transition Metals Carbides (MXenes). *ACS Nano* **9,** 9507–9516 (2015).

124. Halim, J. *et al.* Synthesis and Characterization of 2D Molybdenum Carbide (MXene). *Adv. Funct. Mater.* **26,** 3118–3127 (2016).

125. Lipatov, A. *et al.* Effect of Synthesis on Quality, Electronic Properties and Environmental Stability of Individual Monolayer Ti3C2MXene Flakes. *Adv. Electron. Mater.* **2,** 1600255 (2016).

126. Hu, M. *et al.* High-Capacitance Mechanism for $Ti_3C_2T_x$ MXene by *in Situ* Electrochemical Raman Spectroscopy Investigation. *ACS Nano* **10,** 11344–11350 (2016).

127. Mashtalir, O. *et al.* Intercalation and delamination of layered carbides and carbonitrides. *Nat. Commun.* **4,** 1716 (2013).

128. Tang, Q., Zhou, Z. & Shen, P. Are MXenes Promising Anode Materials for Li Ion Batteries? Computational Studies on Electronic Properties and Li Storage Capability of Ti_3C_2 and $Ti_3C_2X_2$ (X = F, OH) Monolayer. *J. Am. Chem. Soc.* **134,** 16909–16916 (2012).

129. Zhao, C., Wang, Q., Zhang, H., Passerini, S. & Qian, X. Two-Dimensional Titanium Carbide/RGO Composite for High-Performance Supercapacitors. *ACS Appl. Mater. Interfaces* **8,** 15661–15667 (2016).

130. Zhao, M. Q. *et al.* Flexible MXene/carbon nanotube composite paper with high volumetric capacitance. *Adv. Mater.* **27,** 339–345 (2015).

131. Maleski, K., Mochalin, V. N. & Gogotsi, Y. Dispersions of Two-Dimensional Titanium Carbide MXene in Organic Solvents. *Chem. Mater.* **29,** 1632–1640 (2017).

132. Harris, P. J. F. *Carbon Nanotube Science. Synthesis, Properties and Applications*. (Wiley-Blackwell, 2009). doi:10.1002/anie.201000314

133. Radushkevich, L. O strukture ugleroda, obrazujucegosja pri termiceskom razlozenii okisi ugleroda na zeleznom kontakte. *Zhurnal Fiz. Khimii* **26,** 88–95 (1952).

134. Monthioux, M. & Kuznetsov, V. L. Who should be given the credit for the discovery of carbon nanotubes? *Carbon N. Y.* **44,** 1621–1623 (2006).

135. Bethune, D. S. *et al.* Cobalt-catalysed growth of carbon nanotubes with single-atomic-layer walls. *Nature* **363,** 605–607 (1993).

136. Iijima, S. & Ichihashi, T. Single-shell carbon nanotubes of 1-nm diameter. *Nature* **363,** 603–605 (1993).

137. Srivastava, D., Wei, C. & Cho, K. Nanomechanics of carbon nanotubes and composites. *Appl. Mech. Rev.* **56,** 215 (2003).

138. Dimitrios Tasis, *,†, Nikos Tagmatarchis, ‡, Alberto Bianco, § and & Maurizio Prato*, ⦀. Chemistry of Carbon Nanotubes. (2006). doi:10.1021/CR050569O

139. Ajayan, P. M. Nanotubes from Carbon. (1999). doi:10.1021/CR970102G

140. Lacerda, L., Bianco, A., Prato, M. & Kostarelos, K. Carbon nanotubes as nanomedicines: From toxicology to pharmacology. *Adv. Drug Deliv. Rev.* **58,** 1460–1470 (2006).

141. Harris, P. J. F., Hernández, E. & Yakobson, B. I. Carbon Nanotubes and Related Structures: New Materials for the Twenty-First Century. *Am. J. Phys.* **72,** 415–415 (2004).

142. Terrones, M. Science and Technology of the Twenty-First Century: Synthesis, Properties, and Applications of Carbon Nanotubes. *Annu. Rev. Mater. Res.* **33,** 419–501 (2003).

143. Li, G. Y., Wang, P. M. & Zhao, X. Mechanical behavior and microstructure of cement composites incorporating surface-treated multi-walled carbon nanotubes. *Carbon N. Y.* **43,** 1239–1245 (2005).

144. Musso, S., Tulliani, J.-M., Ferro, G. & Tagliaferro, A. Influence of carbon nanotubes structure on the mechanical behavior of cement composites. *Compos. Sci. Technol.* **69,** 1985–1990 (2009).

145. Fakhru'l-Razi, A. *et al.* Effect of multi-wall carbon nanotubes on the mechanical properties of natural rubber. *Compos. Struct.* **75,** 496–500 (2006).

146. Geim, A. K. Graphene: Status and prospects. *Science (80-.).* **324,** 1530–1534 (2009).

147. Geim, A. K. & Novoselov, K. S. The rise of graphene. *Nat. Mater.* **6,** 183–191 (2007).

148. Zhang, Y., Tan, Y. W., Stormer, H. L. & Kim, P. Experimental observation of the quantum Hall effect and Berry's phase in graphene. *Nature* **438,** 201–204 (2005).

149. Neto, A. H. C., Guinea, F., Peres, N. M. R., Novoselov, K. S. & Geim, A. K. The electronic properties of graphene. *Rev. Mod. Phys.* **81,** 109–162 (2007).

150. Beenakker, C. W. J. Colloquium: Andreev reflection and Klein tunneling in graphene. *Rev. Mod. Phys.* **80,** 1337–1354 (2008).

151. Novoselov, K. S. *et al.* Electronic properties of graphene. *Phys. Status Solidi Basic Res.* **244,** 4106–4111 (2007).

152. Morozov, S. V. *et al.* Giant intrinsic carrier mobilities in graphene and its bilayer. *Phys. Rev. Lett.* **100,** 016602 (2008).

153. Falkovsky, L. A. Optical properties of graphene. *J. Phys. Conf. Ser.* **129,** 012004 (2008).

154. Nair, R. R. *et al.* Fine structure constant defines visual transparency of graphene. *Science (80-.).* **320,** 1308 (2008).

155. Lee, C., Wei, X., Kysar, J. W. & Hone, J. Measurement of the elastic properties and intrinsic strength of monolayer graphene. *Science (80-.).* **321,** 385–388 (2008).

156. Dong, Y., Wu, Z. S., Ren, W., Cheng, H. M. & Bao, X. Graphene: a promising 2D material for electrochemical energy storage. *Sci. Bull.* **62,** 724–740 (2017).

157. Wu, Z. S. *et al.* Graphene/metal oxide composite electrode materials for energy storage. *Nano Energy* **1,** 107–131 (2012).

158. Chen, H., Müller, M. B., Gilmore, K. J., Wallace, G. G. & Li, D. Mechanically strong, electrically conductive, and biocompatible graphene paper. *Adv. Mater.* **20,** 3557–3561 (2008).

159. Balandin, A. A. Thermal properties of graphene and nanostructured carbon materials. *Nat. Mater.* **10,** 569–581 (2011).

160. Schedin, F. *et al.* Detection of individual gas molecules adsorbed on graphene. *Nat. Mater.* **6,** 652–655 (2007).

161. Rumyantsev, S., Liu, G., Shur, M. S., Potyrailo, R. A. & Balandin, A. A. Selective gas sensing with a single pristine graphene transistor. *Nano Lett.* **12,** 2294–2298 (2012).

162. Wang, C. *et al.* A novel hydrazine electrochemical sensor based on the high specific surface area graphene. *Microchim. Acta* **169,** 1–6 (2010).

163. Ning, G. *et al.* High capacity gas storage in corrugated porous graphene with a specific surface area-lossless tightly stacking manner. *Chem. Commun.* **48,** 6815–6817 (2012).

164. Varrla, E. *et al.* Turbulence-assisted shear exfoliation of graphene using household detergent and a kitchen blender. *Nanoscale* **6,** 11810–11819 (2014).

165. Park, M. H. *et al.* Silicon nanotube battery anodes. *Nano Lett.* **9,** 3844–3847

(2009).

166. Maranchi, J. P., Hepp, A. F., Evans, A. G., Nuhfer, N. T. & Kumta, P. N. Interfacial Properties of the a-Si/Cu:Active–Inactive Thin-Film Anode System for Lithium-Ion Batteries. *J. Electrochem. Soc.* **153,** A1246 (2006).

167. Liu, W. R. *et al.* Effect of electrode structure on performance of Si anode in Li-ion batteries: Si particle size and conductive additive. *J. Power Sources* **140,** 139–144 (2005).

168. Oumellal, Y. *et al.* The failure mechanism of nano-sized Si-based negative electrodes for lithium ion batteries. *J. Mater. Chem.* **21,** 6201–6208 (2011).

169. Obrovac, M. N. & Christensen, L. Structural Changes in Silicon Anodes during Lithium Insertion/Extraction. *Electrochem. Solid-State Lett.* **7,** A93 (2004).

170. Takamura, T., Uehara, M., Suzuki, J., Sekine, K. & Tamura, K. High capacity and long cycle life silicon anode for Li-ion battery. *J. Power Sources* **158,** 1401–1404 (2006).

171. Yin, Y. X., Wan, L. J. & Guo, Y. G. Silicon-based nanomaterials for lithium-ion batteries. *Chinese Sci. Bull.* **57,** 4104–4110 (2012).

172. Beaulieu, L. Y., Eberman, K. W., Turner, R. L., Krause, L. J. & Dahn, J. R. Colossal Reversible Volume Changes in Lithium Alloys. *Electrochem. Solid-State Lett.* **4,** A137 (2001).

173. Ryu, J. H., Kim, J. W., Sung, Y.-E. & Oh, S. M. Failure Modes of Silicon Powder Negative Electrode in Lithium Secondary Batteries. *Electrochem. Solid-State Lett.* **7,** A306 (2004).

174. An, S. J. *et al.* The state of understanding of the lithium-ion-battery graphite solid electrolyte interphase (SEI) and its relationship to formation cycling. *Carbon N. Y.* **105,** 52–76 (2016).

175. Verma, P., Maire, P. & Novák, P. A review of the features and analyses of the solid electrolyte interphase in Li-ion batteries. *Electrochim. Acta* **55,** 6332–6341 (2010).

176. Aurbach, D. Review of selected electrode–solution interactions which determine the performance of Li and Li ion batteries. *J. Power Sources* **89,** 206–218 (2000).

177. Nie, M., Abraham, D. P., Chen, Y., Bose, A. & Lucht, B. L. Silicon Solid Electrolyte Interphase (SEI) of Lithium Ion Battery Characterized by Microscopy and Spectroscopy. *J. Phys. Chem. C* **117,** 13403–13412 (2013).

178. Ohara, S., Suzuki, J., Sekine, K. & Takamura, T. A thin film silicon anode for Li-ion batteries having a very large specific capacity and long cycle life. *J. Power Sources* **136,** 303–306 (2004).

179. Yao, Y. *et al.* Interconnected silicon hollow nanospheres for lithium-ion battery anodes with long cycle life. *Nano Lett.* **11,** 2949–2954 (2011).

180. Liu, X. H. *et al.* Size-dependent fracture of silicon nanoparticles during lithiation. *ACS Nano* **6,** 1522–1531 (2012).

181. Liu, X. H. *et al.* Anisotropic swelling and fracture of silicon nanowires during

lithiation. *Nano Lett.* **11,** 3312–3318 (2011).

182. Liu, X. H. *et al.* Size-Dependent Fracture of Silicon Nanoparticles During Lithiation. *ACS Nano* **6,** 1522–1531 (2012).

183. Graetz, J., Ahn, C. C., Yazami, R. & Fultz, B. Highly Reversible Lithium Storage in Nanostructured Silicon. *Electrochem. Solid-State Lett.* **6,** A194 (2003).

184. Wang, C. M. *et al.* In situ transmission electron microscopy and spectroscopy studies of interfaces in Li ion batteries: Challenges and opportunities. *J. Mater. Res.* **25,** 1541–1547 (2010).

185. Cui, L.-F., Hu, L., Choi, J. W. & Cui, Y. Light-Weight Free-Standing Carbon Nanotube-Silicon Films for Anodes of Lithium Ion Batteries. *ACS Nano* **4,** 3671–3678 (2010).

186. Fan, Y. *et al.* High performance carbon nanotube–Si core–shell wires with a rationally structured core for lithium ion battery anodes. *Nanoscale* **5,** 1503 (2013).

187. Wang, X., Sun, L., Agung Susantyoko, R., Fan, Y. & Zhang, Q. Ultrahigh volumetric capacity lithium ion battery anodes with CNT–Si film. *Nano Energy* **8,** 71–77 (2014).

188. Luo, J. *et al.* Crumpled Graphene-Encapsulated Si Nanoparticles for Lithium Ion Battery Anodes. *J. Phys. Chem. Lett.* **3,** 1824–1829 (2012).

189. Zhao, X., Hayner, C. M., Kung, M. C. & Kung, H. H. In-Plane Vacancy-Enabled High-Power Si-Graphene Composite Electrode for Lithium-Ion Batteries. *Adv. Energy Mater.* **1,** 1079–1084 (2011).

190. Lee, J. K., Smith, K. B., Hayner, C. M. & Kung, H. H. Silicon nanoparticles–graphene paper composites for Li ion battery anodes. *Chem. Commun.* **46,** 2025 (2010).

191. Yuan, L.-X. *et al.* Development and challenges of LiFePO $_4$ cathode material for lithium-ion batteries. *Energy Environ. Sci.* **4,** 269–284 (2011).

192. Padhi, A.K., Nanjundaswamy, K.S. Goodenough, J. . LiFePO4: a novel cathode material for rechargeable batteries. in *Electrochemical Society Meeting Abstracts* (1996).

193. Huang, H., Yin, S.-C. & Nazar, L. F. Approaching Theoretical Capacity of LiFePO[sub 4] at Room Temperature at High Rates. *Electrochem. Solid-State Lett.* **4,** A170 (2001).

194. Tarascon, J. M. & Armand, M. Issues and challenges facing rechargeable lithium batteries. *Nature* **414,** 359–367 (2001).

195. Zheng, J., Li, X., Wang, Z., Guo, H. & Zhou, S. LiFePO4 with enhanced performance synthesized by a novel synthetic route. *J. Power Sources* **184,** 574–577 (2008).

196. L. Laffont, *,† *et al.* Study of the LiFePO4/FePO4 Two-Phase System by High-Resolution Electron Energy Loss Spectroscopy. (2006). doi:10.1021/CM0617182

197. Zaghib, K. *et al.* Optimized electrochemical performance of LiFePO4 at 60 °C

with purity controlled by SQUID magnetometry. *J. Power Sources* **163,** 560–566 (2006).

198. Wang, K. *et al.* Process investigation, electrochemical characterization and optimization of LiFePO4/C composite from mechanical activation using sucrose as carbon source. *Electrochim. Acta* **54,** 2861–2868 (2009).

Chapter 2: Experimental Methods and Techniques

In this chapter, the experimental techniques and methods used within this thesis will be described. This will include microscopy techniques, (primarily focussing on transmission electron microscopy (TEM)), the methods of synthesis or exfoliation of the materials used, the inkjet printing process in general, and electrochemistry analysis. This section is intended as a general overview of methods used. Experimental procedures that require a depth of treatment will be presented in later chapters where relevant.

2.1 Electron Microscopy

In this section various features of electron microscopy will be discussed with a primary focus on Transmission Electron Microscopy, Scanning Transmission Electron Microscopy and their functions within this work. In microscope spectroscopic techniques will also be described where relevant.

2.1.1 Transmission Electron Microscopy (TEM)

Electron microscopy is the most important method of morphological analysis available to modern scientists. The primary driving force behind the development of the first electron microscopes were the fundamental physical limits of traditional optical microscopes. The minimum resolution for an optical microscope is diffraction limited, and given by the classical Rayeleigh Criterion given in Equation 2.1[1] which relates the wavelength of light used to create an image with the resolution possible.[1]

$$\delta = \frac{0.61\lambda}{\mu Sin\beta} \tag{2.1}$$

Where δ is the minimum distance that can be resolved, λ is the wavelength of the radiation used to create the image, μ is the refractive index of the viewing medium and β is the semi-angle of collection of the magnifying lens.[1] The collective term $\mu Sin\beta$ is also known as the Numerical Aperture (NA) when talking about lens systems and microscopes. The NA for an optical or visible light microscope can be

approximated to unity, and so for a microscope using radiation in the middle of the visible spectrum (≈550nm) the minimum distance that can be resolved is ≈ 300nm.

This was widely seen as a fundamental viewing limit in microscopy until 1925 when Louis de Broglie theorised wave-particle duality and the relationship between the energy and wavelength of a particle.[2] According to the de Broglie equation, the wavelength of an accelerated particle is related to its accelerating voltage V by[3]

$$\lambda = \frac{h}{(2m_0 eV)^{\frac{1}{2}}} = \frac{1.22nm}{V^{\frac{1}{2}}} \tag{2.2}$$

Where m_0 is the mass of the particle, eV is the particle's kinetic energy and h is Planck's constant. For a transmission electron microscope, μ≈1 and Sinß≈ß due to the small angle approximation (In the case of most aperture systems ß≈10 mrad)[3]. When this is brought back into Equation 2.1 we finally obtain our resolution limit for a TEM; [3]

$$\delta = \frac{0.74}{\beta V^{\frac{1}{2}}} \tag{2.3}$$

An electron accelerated using a voltage of 300kV therefore has a wavelength of 4 pm and a theoretical resolution of 3 pm. It is important to note that the preceding definitions and explanations ignore relativistic effects, which is not sufficient once the accelerating voltage > ≈100 kV. We term this as a "theoretical" limit because even modern TEMs cannot come close to this limit. The achievable resolution is limited due to lens imperfections.

Very soon after de Broglie's breakthrough, the first TEM was developed by Ruscka *et al.*[4] At a basic level, a TEM consists of an electron source, a condenser lens, a specimen, an objective lens and some kind of viewing mechanism. The images are formed by detecting the changes in the electrons that pass through the specimen. The lenses in a TEM are usually electromagnetic coils with which the deflection of the electron beam can be changed by varying the current through the coil. Almost all focus and magnification operations in a TEM are controlled by manipulating the lens coil current.

The electron guns used in modern TEMs come in many forms divided largely into thermionic guns and field emission guns. The exact differences and operating principles are outside the scope of this work, but the information, like much of the

contents of this section can be found in great detail in Transmission Electron Microscopy, by Williams and Carter.[5] The electron gun consists of a source that emits electrons when a high current is passed through it. The gun assembly then focusses the emitted stream of electrons.[5] In standard operating mode, the Condenser lens serves to illuminate the specimen with a parallel electron beam. This beam passes through the sample and an image is formed on a detector by the objective lens below the sample. A number of different electron signals can be processed from the beam passing through the thin sample, as shown in Figure 2.2

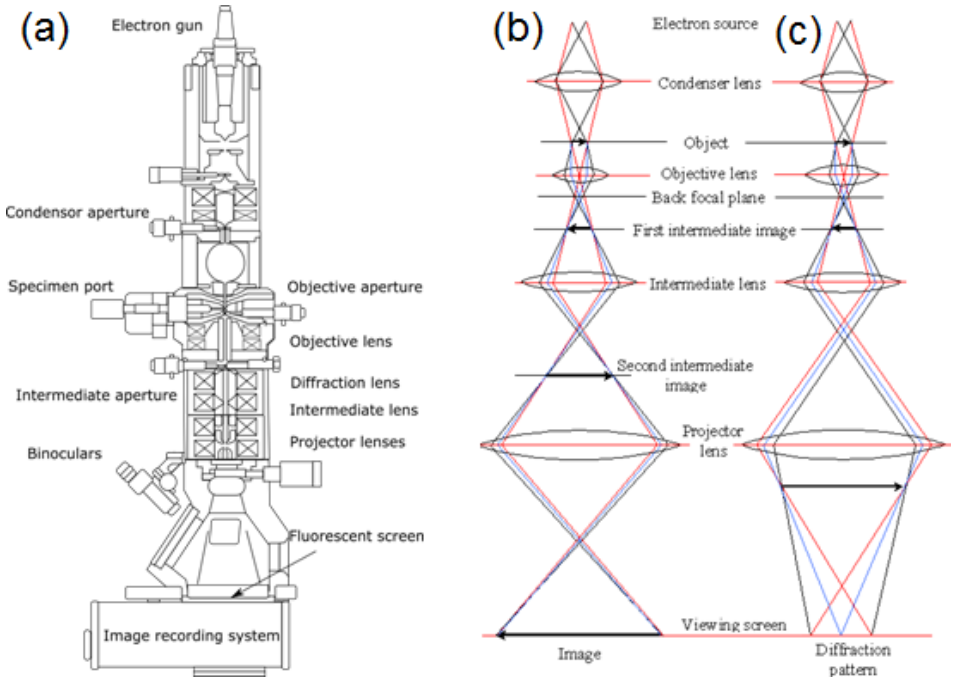

Figure 2.1: (a) Schematic diagram of typical TEM showing electron gun, lens apparatus and imaging system, Ray Diagrams showing the two primary imaging functions of a TEM (a) the lens apparatus for standard Bright Field imaging and (c) ray diagram for producing diffraction patterns through selected area electron diffraction (SAED). Adapted from Ref (1).

While not every type of signal shown in Figure 2.2 can be captured by every TEM, it gives a reasonable idea of the scale of characterisation methods that can be conducted. Emitted x-rays and Electron Energy Loss Spectroscopy (EELS) can be used to conduct chemical composition analysis on different materials, diffraction patterns can identify fine crystal structure and direct imaging provides morphological information -making the TEM a very powerful tool for material analysis.

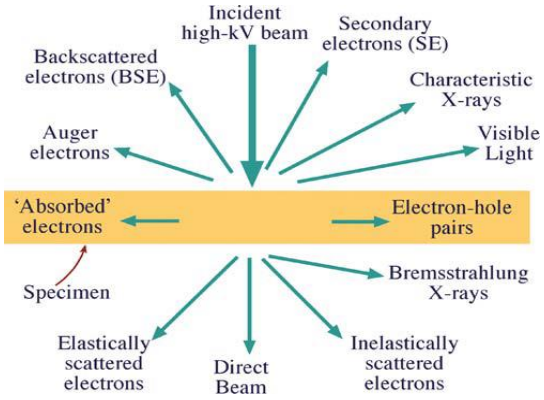

Figure 2.2: The range of signals that occur and can be processed within a TEM system. Adapted from Ref (1).

The electromagnetic lenses of the TEM are imperfect, limiting the resolution of the acquired image and create a number of types of aberrations that must be accounted for. The primary types of aberrations are astigmatism, spherical aberration and chromatic aberration. Astigmatism is caused by a non-uniform magnetic field acting upon the spiralling electrons as they pass through the lens. This non-uniform magnetic field can be caused by incorrect operating parameters or contamination but is also inherent to a certain extent to the metal of the lens' themselves. It is not possible to mill a perfectly symmetrical iron pole piece and micro-structural defects can cause small but noticeable astigmatism within the beam. Fortunately, this is the easiest of the aberrations to fix, with stigmators in the illumination systems introducing compensating fields. Ray diagrams of the different kinds of aberration described are shown in Figure 2.3.

Spherical aberration occurs when electrons entering the lens system off-axis are deflected more than required. The wave-front from a point to be imaged are spherically distorted so that the image projected is not a point but a disk of varying intensity. This aberration can be corrected by a complex series of computer controlled octo-, hexa- and quadrupoles in more expensive aberration-corrected microscopes.

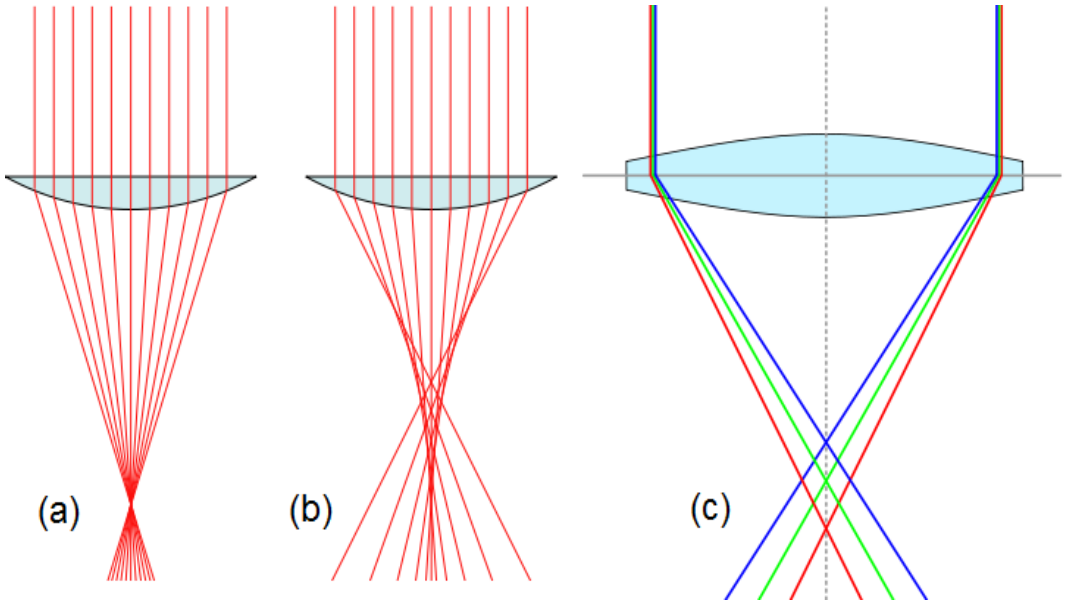

Figure 2.3: Ray diagrams of (a) an ideal image formation with no aberration, (b) spherical aberration where a coherent wavefront has been spherically distorted resulting in a distorted signal in the image plane and (c) chromatic aberration where electrons of lower energies have been deflected more by the objective lens.

Chromatic aberration occurs due to differences in how the pole pieces bend electrons whose energies and therefore wavelengths, differ. The actual energy variances within electron guns is at most 1eV for a 100 keV beam. If there was no sample present, chromatic aberration would not present a substantial issue. However, a very large range of electron energies are produced when the electrons interact with a sample, particularly if the sample is not sufficiently thin enough. Monochromators or Energy Filtering can offer a solution to this particular abberation[3]. It is key to note at this point that the prevalence of chromatic aberration in thick samples will be an important limiting factor on resolution later in this work. TEM will be conducted on very thick, liquid samples. Chromatic aberration is one of many reasons why resolution is limited, and focus is difficult to achieve in these situations.

Above all else, useful TEM data relies on electron scattering to create an image in the imaging system. A uniform intensity of electrons enters the sample and a non-uniform intensity of electrons emerge; all data obtained, morphological and chemical, relies on these varying intensities. While single scattering is the ideal scattering event to occur, providing the least ambiguous information about the sample, multiple scattering events can and do occur. It is for this reason that sample thickness is important. While the information provided from a single scattering event is easily interpreted, this becomes much more difficult as the number of

scattering events increase. The probability of an electron scattering event occurring p as an electron passes through a sample of thickness t is given in Equation 2.4[6];

$$p = \frac{N_0 \sigma_{atom} \rho t}{A} \tag{2.4}$$

Where N_0 is Avogadro's number, σ_{atom} is the scattering cross section of the atoms of the sample, ρ is the density of the atoms in the sample and A is the atomic weight of the atoms of the sample. From this we can clearly see that the number of expected scattering events is very much dependant on sample thickness and the atomic weight of the specimen. This represents the key limiting factor in this work as later TEM will be conducted using layers of liquid encapsulated by SiN_x layers, where the minimum sample thickness exceeds the traditionally recommended sample thickness for TEM analysis.

Energy filtered transmission electron microscopy (EFTEM) has proven quite useful in obtaining useful data for in-situ experiments.[7] In this process, the kinetic energy of the transmitted electrons are determined. This is usually used as the first step in Electron Energy Loss Spectroscopy (EELS) where electrons of differing energies are used to form spectra from which elemental information can be determined, but it can also be used to generate images on its own. A filter or slit can be applied to the transmitted electrons allowing only electrons of a particular kinetic energy to form the image. Using this process can be very useful for determining chemical changes in a material, such as those seen in supercapacitive or battery materials, but it is important that the selected kinetic energy is appropriate. If an incorrect energy is selected, no usable information will be transmitted to the image forming detector. In addition, this process will filter out most other signals, resulting in a lower overall intensity. It is useful if the mechanism or chemical process that is to be imaged is very well-known and predictable.

2.1.2 Scanning Transmission Electron Microscopy

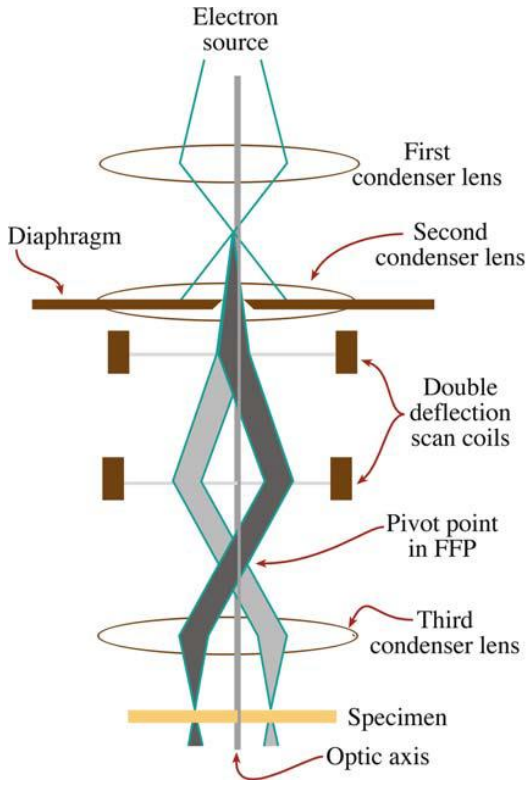

Figure 2.4: General outline of the operating principles of the microscope in STEM mode. The beam is concentrated to a point probe and is rastered across the specimen by a series of deflection coils. Note that there are no further lenses after the specimen, the transmitted signal is sent straight to the electron detection system. Diagram adapted from Ref (8)

Scanning transmission electron microscopy or STEM is another imaging mode available to TEM operators. In this configuration, the parallel beam of the conventional mode TEM is changed to a tightly converging beam, illuminating a much smaller area. This is primarily controlled by the C_1 and C_3 condenser lenses and a pair of scanning coils after the specimen. Since the illuminated area is far smaller, in order to create useable contrasts and images the scan coils are used to raster the converging electron probe across the area of interest. This beam scans parallel to the optical axis of the microscope at all times, mimicking the operation of the conventional parallel beam. No post-specimen lenses are used, and this signal is directly displayed. The general schematic of the interaction of the beam and the lens coils is given in Figure 2.4.

The images of STEM are detected using a bright field (BF) detector, usually collecting direct beam electrons, and an annular dark field (ADF) detector, which is concentric around the BF detector. A further detector, the high angle annular dark

field detector (HAADF) lies outside the ADF detector, collecting highly scattered signals. The HAADF detector is particularly sensitive to changes in the atomic number of the material, Z, as it collects Rutherford scattered electrons.[8] In general BF STEM images have a higher contrast but poorer resolution than their BF TEM counterparts.[9] Dark Field (DF) signals are superior in STEM mode however as the ADF detector can detect a large number of scattered signals compared to a DF TEM detection system which relies on a small signal selected by the objective aperture.

Due to the fact that there are no post-specimen lenses, STEM images formed in this way do not suffer from lens aberration. This is particularly useful in thicker samples where chromatic aberration can severely limit the contrast and resolution achievable. Due to this, significant improvement in image acquisition and resolution can be achieved using STEM mode while imaging liquid cell TEM samples. In addition the scanning STEM beam allows the user to control the extent of the irradiated region to a much greater degree than in conventional TEM mode. This is an important feature for use in liquid cell studies as liquid electrolytes have been observed to be quite sensitive to the electron beam. It is important for the user to be able to discern what visible changes are being induced by the applied voltages and what changes are beam induced. Furthermore, the standard TEM beam can break down the electrolyte itself, forming gas bubbles and rupturing the delicate nitride windows of the cell.

2.1.3 Scanning Electron Microscopy

While the primary characterisation tool used in this work is the TEM, the scanning electron microscope is an equally valuable method for analysing material and structures. In this work the SEM was used to image structures when printed onto flexible substrates for planar printed energy storage devices. The SEM is particularly useful for analysing the topography of a surface. Similar to the TEM, an electron source produces a stream of electrons incident to the sample that is to be analysed. These electrons have a much lower energy than those of the TEM, usually in a range of 1 to 40 keV. This beam is focussed using a set of condenser lenses and is scanned across the specimen by a set of scanning coils. The scanning beam generates an image point by point as the beam is rastered across a set rectangular viewing area that is to be imaged.

The images are formed from a number of signals generated by the incident beam, but mainly from Secondary Electrons (SEs) and Backscattered Electrons (BSEs). These can also be found listed on Figure 2.2 previously. BSEs are typically higher energy (up to half the incident beam energy)[10] elastically scattered electrons with SEs being very low kinetic energy (≤ 20 eV)[11] electrons that have been ejected from the sample due to inelastic scattering interactions with the electrons of the beam. SE and BSE detectors absorb these signals, with each discrete signal assigned to an image pixel. This is how the microscope forms images.[12] Secondary electrons are generally generated at the surface, and so can give highly accurate topographical information.[13]

In order to create clear and representative images, much like in a TEM there are a number of variables that the SEM operator can adjust. Beam current, beam diameter, and beam convergence angle can all be manipulated to produce clear SEM images of the specimen. Much like the TEM, radiation damage must be considered when imaging a sample with the SEM, and some materials can be very sensitive to the beam interaction. In addition to, this non-conductive materials can build up charge during imaging with an SEM. As electrons are inserted into the sample with the beam, they will begin to accumulate if they are not connected to a ground.[14] This accumulation of charge will introduce a distorting electric field to the specimen, which will slow down incident electrons, and therefore change the energy of the signals being detected by the SE and BSE detectors of the SEM.

In many ways the SEM is similar to the TEM, but they have traditionally occupied different spaces in terms of their uses; the SEM being the more robust examination tool for larger samples and those requiring superior topographical and depth of field images, and the TEM being used for fine examination and high-resolution imaging of materials. They are largely two complimentary techniques, with most experiments requiring high magnification imaging using both methods at some point.

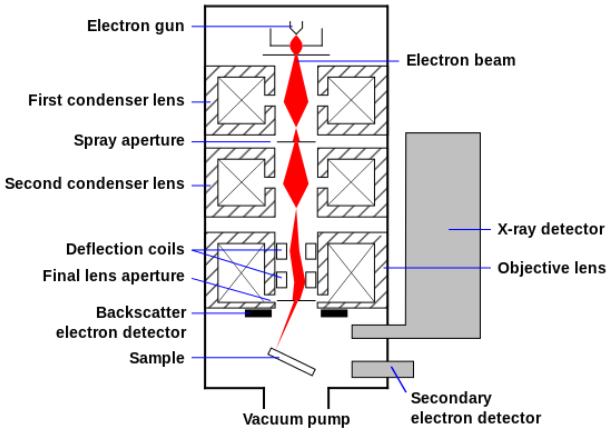

Figure 2.5: Schematic diagram of a typical SEM, showing electrons passing through the lens structures and hitting the sample. The detectors are located above the sample, absorbing backscattered and secondary electrons.

2.3 Liquid Phase Exfoliation (LPE)

As more and more research is conducted into the physical and electronic properties of two-dimensional materials, a single question persists; how to effectively separate these materials from their bulk counterparts? There are many methods of synthesising and exfoliating 2D materials, but few are suitable for both laboratory and commercial applications. Taking graphene as an example, while the original mechanical exfoliation technique (using scotch tape to shear layers from each other breaking the Van der Waals bonds) first demonstrated by Novoselov *et al*[15] is effective at producing very high quality graphene, it results in a low yield and the procedure is not necessarily scalable to industrial levels.

Liquid phase exfoliation (LPE) was a technique developed first in 2008[16] that allowed for high yield production of graphene at a low cost. Since then, the process has been further applied to a range of other layered materials including MnO_2[17,18], MoS_2[19,20], hexagonal boron nitride (h-BN)[21,22], as well as a range of layered double hydroxides (LDHs)[23]. As a process, LPE displays a distinct advantage in the sheer number of different materials that can be synthesised and exfoliated, offering a diverse range of physical, electronic and optical properties to the user depending on the material chosen to be exfoliated. These materials can be exfoliated into 2D nanosheets as they exhibit a structural similarity to graphene; they have strong in-plane atomic bonds but very weak interlayer bonds. This allows the layers to be

detached quite easily when energy is applied. For the liquid phase exfoliation methods used in this work, two separate but equally important processes contribute to the effective exfoliation and dispersion of nanomaterials in solvent; ultrasonic irradiation and solvent matching.

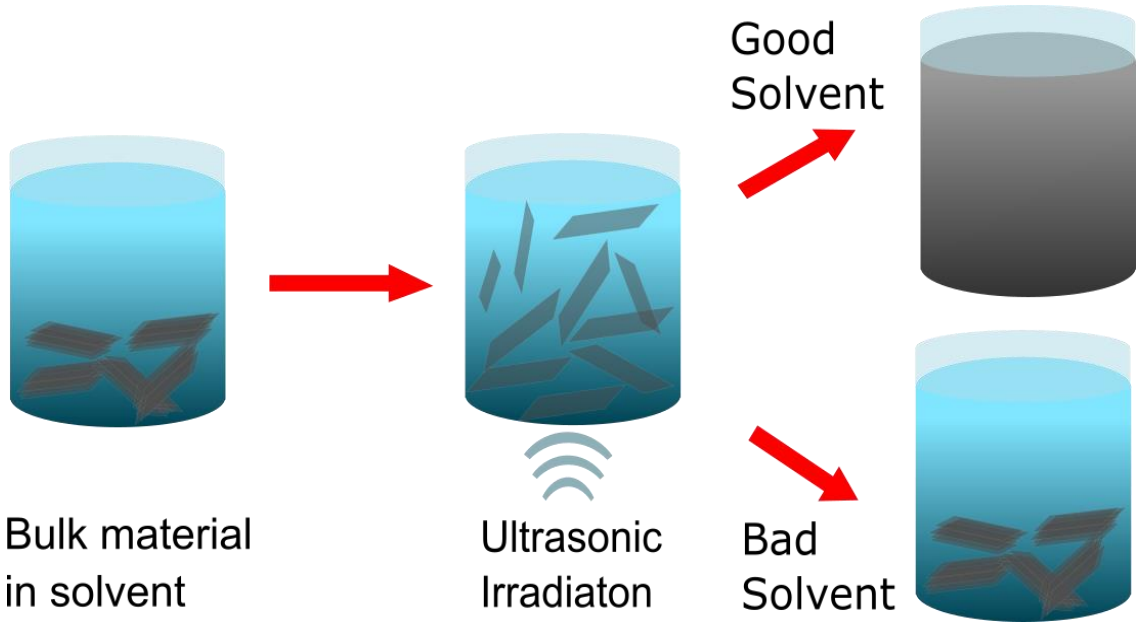

Figure 2.6: The process of Liquid Phase Exfoliation of layered materials. Bulk materials are exposed to ultrasonic irradiation to break the inter-plane bonds forming nanosheets. If the solvent and solute are well matched, the material will remain in suspension in its nanosheet form.

Ultrasonic irradiation is the process by which energy is imparted to the bulk layered material, breaking the weak inter-plane Van der Waals bonds and exfoliating the bulk material into nanosheets. This energy is not actually directly provided by the high frequency acoustic waves however, it relies on a process known as cavitation which is the formation of vapour pockets or bubbles within a liquid. As acoustic waves pass through the liquid, the molecules of the liquid oscillate. If the negative pressure is enough to separate the molecules further than the critical distance required to maintain the liquid state, the liquid will break down and cavities will appear, hence the term cavitation. These bubbles will continue to expand during the rarefaction step of the wave until a maximum negative pressure is reached. From this point, entering the compression part of the acoustic wave cycle, they will contract. This contraction and eventual collapse of the bubble releases the energy stored in bubble growth process in a very short period of time resulting in extremely high localised pressures (~100 bar) and temperatures (~6000K).[24,25] These collapsing

bubbles can impart enormous amounts of energy to the surrounding matter, and can be the cause of serious damage- in the field of naval engineering for example, this process is well known for damage caused to ship propellers.[26–28]

The interaction of these bubbles with matter is key to the concept of liquid phase exfoliation. Nucleation sites for bubbles can be created more easily from gases trapped in defects and crevasses within particulate matter.[25] These bubbles will form within the defects and eventually break away from the particle. Cavitation bubbles which collapse near a boundary deform, and rather than collapsing evenly, they collapse asymmetrically.[24,29,30] This asymmetric collapse of the bubble generates microjets within the bubble. These microjets can pierce the bubble as it collapses, directing the localised pressure effects. These microjets extend from the collapsing bubble towards the interface that is causing the asymmetric deformation of the bubble itself. In practical terms, a bubble is generated by a nucleation site on the surface of material suspended in a liquid. The collapse of that bubble causes the energy that is contained within it to be directed back towards the material that induced the bubble growth. Figure 2.6 (a) shows the schematic shape that the deformation takes as the radius of the bubble contracts when close to a surface. The internal microjet formation of the collapsing bubble can be seen through the progression of images in Figure 2.6 (b).

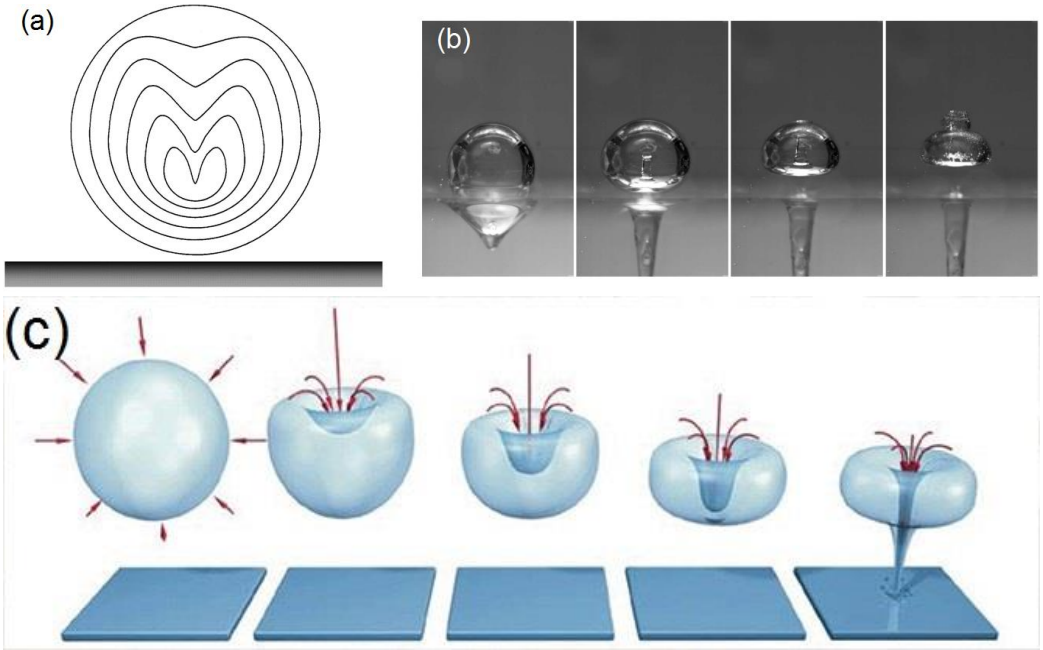

Figure 2.7: Deformation and collapse of cavitation bubbles close to boundaries where (a) shows the internal shape change of collapsing bubble close to a surface (b) shows a high speed image of a collapsing cavitation bubble producing a microjet in the direction of the interface and (c) shows the general process of the microjet being directed towards the surface as it collapses. (a) adapted from Ref (25), (b) adapted from Ref (26).

Detailed and extensive mathematical treatments of the bubble inducing phenomena have been carried out in References 24 and 25, but are outside the scope of this work.

For liquid phase exfoliation it is these microjets, and the large shear forces that they generate that break apart the interlayer bonds of the dispersed layered materials, forming suspended nanosheets.[16,25,31,32] Extensive studies have been conducted as to the effect of sonication time, frequency and intensity on the yield and quality of the final material.[33,34]

Solvent matching is the second process that is required for effective liquid phase exfoliation. Once the acoustic cavitation effects have separated the sheets from the bulk, it is important that the sheets do not re-aggregate from their exfoliated form. A process of solvent matching is required whereby the surface energy of the material that is to be exfoliated and dispersed is matched to the surface energy of the solvent. This process gives an outline of what solvents will maintain stability but can further be refined by examining what are known as the solubility parameters of the system. Under isothermal and isobaric conditions the interaction of a dispersion can be given by the Gibbs free energy[35]

$$\Delta G_{mix} = \Delta H_{mix} - T\Delta S_{mix} \tag{2.5}$$

Where ΔG_{mix} is the Gibbs free energy, ΔH_{mix} is the Enthalpy of mixing, T is the absolute temperature and ΔS_{mix} is the Entropy of mixing. To create stable dispersions the Gibbs free energy must be negative. From Equation 2.5 this can be achieved by either increasing ΔS_{mix} or decreasing ΔH_{mix}. It has been found that due to the rigidity of materials such as nanotubes and 2D nanosheets ΔS_{mix} is relatively small.[36,37] This results in ΔH_{mix} being the dominant term of the process and and therefore in order to create a stable nanomaterial dispersion the energetic cost should be minimised. The Hildebrand-Scratchard Equation allows us to quantify the energetic cost of mixing a solute and solvent[38]

$$\Delta H_{mix} \approx (\delta_A - \delta_B)^2 \phi(1-\phi) \tag{2.6}$$

Where ΔH_{mix} is the enthalpy of mixing per unit volume of the solvent, δ_A and δ_B are the Hildebrand Solubility Parameters of the solute and the solvent respectively and ϕ is the solute volume fraction. The minimisation of the enthalpy of mixing leads to a solution that is closer to an ideal solution and so it is more likely that mixing will occur.[35,39] From Equation 2.6 it can be seen that the closer the Hansen solubility parameters of the solute and solvent, the closer ΔH_{mix} will approach zero. Therefore

this equation provides us with a basic framework whereby stable dispersions can be predicted. Hildebrand solubility parameters are simply the root of the cohesive energy density of the material, i.e $\delta = \sqrt{E_C/V}$. However this approximation only takes into account the dispersive contributions to the cohesivie energy density, and for a more complete treatment, polar and hydrogen contributions must be accounted for. There will be three separate contributions towards the total cohesive Energy density E_C;[40]

$$\frac{E_C}{V} = \frac{E_D}{V} + \frac{E_P}{V} + \frac{E_H}{V} \tag{2.7}$$

Where E_D, E_P and E_H are the dispersive, polar and hydrogen bond contributions to the total cohesive energy density respictively[41]. This results in three separate Hansen solubility parameters that contribute to the Hildebrand parameter[40]

$$\delta^2 = \delta_D^2 + \delta_P^2 + \delta_H^2 \tag{2.8}$$

This allows a reconfiguration of Equation 2.6 to more accurately describe the interactions and show how the solubility parameters can separately effect ΔH_{mix}; [41]

$$\Delta H_{mix} \approx [(\delta_{DA} - \delta_{DB})^2 + (\delta_{PA} - \delta_{PB})^2 + (\delta_{HA} - \delta_{HB})]\phi(1-\phi) \tag{2.9}$$

Equations 2.6 and 2.9 show that in general, dispersions will be stable when A-B interactions (solvent-solute) are as energetically close as possible to A-A interactions and B-B interactions. [41] It is from this point of view that we approach solubility parameters for dispersions of exfoliated nanomaterials. Solvents that closely match the solubility parameters of the dispersed materials will tend to produce stable dispersions and the material will not have a large energetic and thermodynamic tendency to reaggregate into its bulk form. As mentioned previously surface energy can initially provide an estimate of what solvent-solute combinations will yield stable dispersions. Working in reverse for un-characterised materials, the solvents surface energies can also be used to infer estimates of the surface energies of the materials that disperse well within them.[42]

The final step in this process is centrifugation. The centrifugation of material serves a dual purpose; firstly, it separates exfoliated and unexfoliated material. The LPE process does not result a 100% yield of exfoliated material, and so the final

dispersions, even when optimised and appropriately solvent matched, will contain unexfoliated bulk material. These dispersions are then centrifuged as a purification process to separate out the bulk, unexfoliated material, which is then removed. Concentration measurements of dispersions are measuered after this process in order to determine exact concentrations of exfoliated material. [16,33,43]

A second use of centrifugation for LPE dispersions is that of particle size selection. Dispersions that have been produced through LPE have a tendency to be polydisperse and to produce small flake sizes (in the case of graphene mean flake size ≈ 1 µm).[44] The polydisperse nature of the dispersions however can be utilised to produce dispersions of a required flake size. With high speed centrifugation, the larger flakes will crash into the sediment. This sediment can be separated from the original dispersion and redispersed in solvent, producing two dispersions of differing flake sizes. Average lateral flake size remaining in the dispersion decreases with increasing centrifugation RPM.[44] This step is essential for full characterisation of the properties of the materials as it has been found in many cases that flake size has a noticable impact on the mechanical and electrical performance of two-dimensional materials.[45,46]

2.4 Inkjet Printing

Inkjet printing has become one of the foremost research methods for the production of flexible electronics and patterned thin films in recent years[47–49]. Inkjet printing is non-contact, direct writing, additive and maskless. Material is directly deposited in patterns that can be very easily changed or altered, allowing for seamless and rapid engineering of different devices and circuits. The primary advantage of inkjet printing is the accuracy and control it allows for the deposition of material inks, allowing for the fabrication of complex patterns and morphologies. This accuracy and control is assisted by modern material deposition systems having a high deposition resolution[50] The DMP 2800 system used in this work boasts a variable resolution of between 100 drops per inch (dpi) and 5080 dpi[51] with the usual working resolution usually used being 1060 dpi. The achievable resolution will typically depend on the spreading of the ink carrier solvent on the chosen substrate In the case of IPA based inks with porous PET substrates as used here, a minimum resolution of between 25 and 50 µm is expected. The accuracy and resolution of inkjet printers allow for the design and manufacture of complex devices such as

transistors[47,52–56], photovoltaics[50,57–61] LEDs[47,62,63] antennae[64–68] and increasingly fully integrated circuitry including some of the aforementioned devices.[69–71]

The additive nature of inkjet printing is one of the reasons this will be a major method of electronics fabrication as the consumer electronics industry pivots to a more renewable model. Material is only deposited where it is needed, saving money where materials are expensive, and reducing overall waste. It also eliminates the need for expensive masks and lithography, resulting in processes that are flexible and easy to modify depending on the desired device.

Crucial to inkjet printing's technical flexibility is the minimisation of process steps required. With sufficiently characterised material inks, very few steps are required to fabricate a device. Thin film transistors (TFTs) for example require separate material printing for the source and drain, the channel, the dielectric and the gate.[52,53,56,72] Depending on the material, no further treatments or processes are required. For simpler devices such as a supercapacitor electrode developed from a conductive material such as graphene[73] or Ti_3C_2 this process can be a single printing step before the device is then encapsulated with electrolyte. Other active materials can be deposited in another simple print pass. This limited number of process steps, and flexibility in terms of the pattern that can be fabricated and materials that can be deposited make inkjet printing an excellent candidate as a deposition method which can be upscaled for rapid mass production.

Inkjet printing developed rapidly from the 1970's onward as a method of processing digital images and documents. Continuous jet printers, whereby a material stream constantly flows from the ink nozzle but is diverted when not needed, were the first to be developed, followed by Drop on Demand (DOD) printers where individual droplets are induced from the printhead at will to form the final pattern.[74] As inkjet printers began to have smaller nozzles and therefore smaller droplet sizes, the achievable resolution was increased making the technology attractive as a fabrication method for thin films and circuitry.[75]

For the manufacture of printed electronics, the operating principles of the printers involved remain largely the same as printers designed to print documents or photographs. The primary difference is the resolution and the materials which the printer is capable of depositing. The continuous jet printer has largely been superseded by its DOD counterpart. It operates by a continuous stream of ink

flowing from the printer ink reservoir to a print head. A piezoelectric element within the print head induces pressure waves within the ink stream creating a finely controlled Rayleigh instability resulting in a steady stream of droplets exiting the nozzle.[74,75] The droplets pass through an electrostatic field and are charged by a charging mechanism or plate. These charged droplets can then be selectively deflected by a deflection plate further down the stream, either into a recycling gutter for recirculation back into the ink reservoir or onto the substrate forming the desired pattern.[74,75]

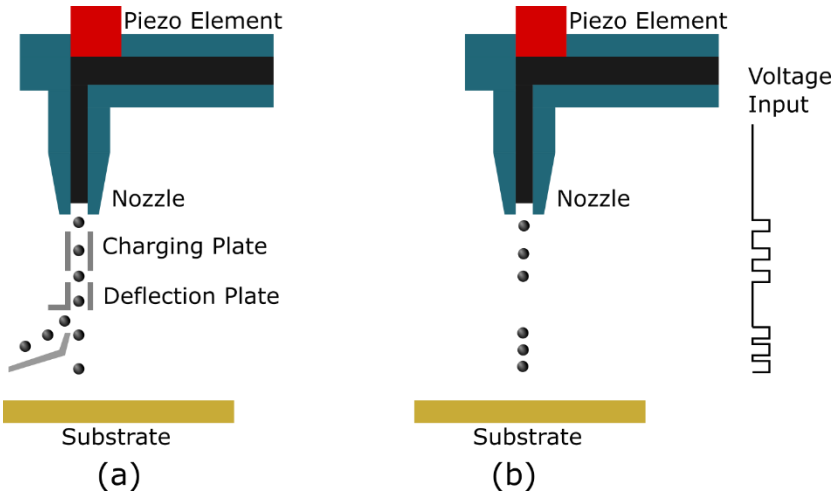

Figure 2.8: Comparison of (a) Continuous Inkjet Printing and (b) Drop on Demand Printing. The deflection plates for continuous jet allow for a control of the pattern formation. For DOD, the voltage driving the Piezo (seen on the right hand side) drives the droplet formation.

Drop on Demand is a more selective approach to droplet deposition. The primary difference between DOD and continuous jet printing is that there is far higher control of droplet generation. DOD printers achieve this in one of two ways; either thermal or piezoelectric. In thermal DOD printing, each ink chamber contains a small heating element. A voltage pulse is sent through this heating element, evaporating a small amount of ink within the ink chamber, leading to a rapid pressure increase. This pressure increase forces the formation of a droplet from the nozzle.[74,76] The collapse of this bubble draws ink back into the print head from the reservoir, readying the head to fire another droplet. The primary limiting factor to this method is the requirement that there must be a volatile component of the ink which can be evaporated to generate the printed droplet. This requirement can act as a limiting factor for what kind of inks and materials can be used.

Piezoelectric DOD printing utilises a similar construction to thermal DOD. A voltage pulse is passed through a piezoelectric element or diaphragm. When a voltage is applied to the piezo element, it deforms creating a pressure pulse through the ink in the print head. This pressure pulse then generates a droplet, which is ejected from the nozzle.[74,75,77] The piezoelectric method is more widely used in commercial and industrial printing than the thermal method and this prevalence has carried over to research systems. The piezoelectric means of deposition displays a number of advantages. As mentioned before, the thermal system requires the ink to have a volatile component in order to generate the bubbles that induce droplet formation. This is not a requirement for piezoelectric based systems. In addition due to an absence of heating, there are no issues with internal ink deposition associated with the evaporation of ink internally in thermal systems. Varying amplitude, shape and duration of the voltage pulses passing through the piezo diaphragm allow the user very fine control over droplet formation and accordingly allows for a range of different inks to be used.

The system used in this work is a Dimatix DMP 2800, manufactured by Fujifilm Dimatix and utilising a set of 16 piezoelectric driven print nozzles. As such, the operating principles applying to a piezoelectric DOD printer apply this work and will be the primary printing method discussed.

Successfully jetting a liquid ink is not simply a matter of passing a voltage pulse through the piezo. Most DOD printers require low viscosity inks in order to form stable droplets, usually in the range 4 to 30 cP,[50] and most printers require a high surface tension to print, usually > 35 mN m^{-1}.[50] Whether an ink can jet, and how it behaves when it does jet is largely governed by the ink surface tension γ, the ink viscosity η, density ρ, the diameter of the nozzle which is ejecting the droplet a and the velocity of the droplet when ejected v.[78,79] The fluid dynamics of the jetting process can be modelled with the Reynolds number[79]

$$Re = \frac{va\rho}{\eta} \tag{2.10}$$

And the Weber number[79]

$$We = \frac{v^2 a\rho}{\gamma} \tag{2.11}$$

The Ohnesorge number is given by relating the Reynolds number and the Weber number in the following manner[79]

$$Oh = \frac{\sqrt{We}}{Re} = \frac{\eta}{\sqrt{\rho\gamma a}} \tag{2.12}$$

For the purposes of describing the fluid dynamics of Inkjet printing systems the final figure of merit that is usually used is Z, the inverse Ohnesorge number, finally giving[79]

$$Z = \frac{\sqrt{\rho\gamma a}}{\eta} \tag{2.13}$$

The value of Z serves as a useful indication of the dominant forces acting within an ink. If Z is small, viscous forces dominate and a large voltage pulse would be required to successfully eject a droplet.[79] In addition it would be expected that there would be a short tail or trail from the ejected droplet. If Z is large, then inertial or surface tension effects dominate and longer tails and potential satellite droplets are to be expected.[49,77] A general rule of thumb to be followed in ink synthesis is that an ink can be jetted effectively for a range of Z values between $1 < Z < 14$. This is a guideline however, and there have been many studies in recent years of jettable inks with Z values as high as 68.5[49,80] and as low as $Z \approx 1$[81] for a UV curable ink. What is clear in these more recent studies, particularly demonstrated by Torrisi *et al*[49], is that effective inks can be developed in choice solvents by carefully tuning the η , ρ and γ in order to jet. This allows for a large range of flexibility when a material or ink that is traditionally outside the accepted Z range is required to be printed. When combined with liquid phase exfoliation, the ability to tune the properties of inks allow for all inkjet-printed structures, requiring no reliance on other deposition methods.

One major concern that cannot be avoided when a material ink is used for inkjet printing is clogging and nozzle blockage. Printing processes have been seen to be quite sensitive to particle dimension and concentration. The a value in the inverse Ohnesorge number (Equation 2.12) is the printer nozzle diameter which largely acts as a limiting factor on maximum particle size. It has been suggested that an optimal particle size is no larger than $\frac{1}{20}$ the size of the nozzle diameter[49,82] in order to prevent

an agglomeration of material at the orifice. While high concentration will result in faster clogging, particle size appears to be the dominant effect on stability with respect to clogging nozzles. For example, Finn *et al* found for graphene exfoliated in NMP, optimal lateral flake size was ~170 nm and optimal concentration was 1.6 mg ml^{-1} for a nozzle of diameter ~ 21 µm.[83] While particle sizes larger than optimal can be printed, clogging increasingly becomes an issue past the $\frac{1}{20}$ ratio depending on the concentration of the ink and the volatility of the solvent used.

Once the droplet has been successfully ejected from the nozzle, its travel, impact and eventual drying is governed by a complicated range of fluid dynamics. The exit velocity of the droplet is largely governed by the voltage that has been used to induce the droplet itself, although the velocity of a droplet for a given voltage will vary depending on the viscosity of the liquid ink. Low viscosity inks require a higher voltage in order to generate a droplet and this resulting droplet will be slower than one from a lower viscosity ink.[84] Ideally the droplets will follow a straight trajectory through the air between the print head and the substrate. Most droplets will be ejected at a velocity that is higher than the terminal velocity for a spherical droplet, and so it would be expected that droplets will slow as they fall between the print head and substrate. When droplets are ejected, they can be followed by a satellite or tail. While waveform and viscosity can be manipulated to mitigate the formation of satellites, sometimes it is unavoidable. Satellites can merge with the leading droplet if given a sufficient travel distance[77] which may result in users wishing to define a higher print height. In addition, while ideally a small print height is desirable for accurate deposition, in some cases where droplets are very large or have a high velocity, splashing of the droplet rather than wetting and spreading can occur[85]. All of these effects must be taken into consideration in order to achieve maximum accuracy, resolution and homogeneity of the final printed structure.

When the liquid droplet is deposited on the surface, it will either wet the surface completely, or it will form a droplet with some non-zero contact angle. These scenarios are termed either a wetting situation or a partial wetting situation. The partial wetting situation can largely be described by Young's relation[86]

$$\gamma_{SG} = \gamma_{SL} + \gamma_{LG} Cos\theta \tag{2.14}$$

Where γ_{SG} is the solid-gas surface energy, γ_{SL} is the solid-liquid surface energy, γ_{LG} is the liquid-gas surface energy and θ is the contact angle the deposited droplet

makes with the surface.[87] This equation essentially shows the equilibrium forces that result when a droplet is deposited onto a surface that it does not completely wet.

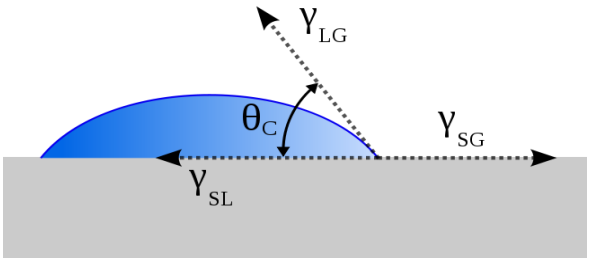

Figure 2.9: The equilibrium forces maintaining a particular contact angle as described by Young's relation.

This relation is only perfectly accurate for a very smooth surface, but the principle stands that the surface energy of the chosen substrate will influence the morphology of the final deposited structure. As the droplet dries it may deposit in a manner known as "coffee staining", first mathematically described by Deegan *et al* in 1997. This phenomenon is important when dealing with high surface energy substrates and/or low concentration dispersions and will be fully described in Chapter 3. Other specific details that relate to the printing of particular materials, or effects caused by particular printing conditions or patterns will be fully described in subsequent chapters.

2.5 Electrochemical Testing

The primary method of electrochemical testing utilised in this work is cyclic voltammetry (CV). CV testing is one of the most widely used methods of characterising the behaviour of materials that are deemed to be electroactive. It is vital in the field of research on energy storing materials, as it allows for accurate descriptions of power and energy densities and allows for an exact quantification of the operating voltage of a battery or supercapacitor system. As such it is a highly robust method to examine all functional aspects of an energy storage system.[88] Kissinger *et al*[88] described cyclic voltammetry as being analogous to a conventional spectrum, conveying chemical information as a function of an energy scan.

The process involves bringing an electrode from one set potential to another, and back to the original potential. The current response of the electrode is measured and the V and I values are usually plotted against one another. This V is controlled versus a reference electrode, which can vary from experiment to experiment, but saturated calomel electrodes or silver/silver chloride electrodes are common.[88] Cyclic voltammetry is important in the field of energy storage as it allows the user to visualise the process of electron transfer kinetics, and thus visualise how energy is stored within a system. A whole range of information can be seen within a CV curve. If redox peaks are present, the potential that is required to induce oxidation can be seen from where the peak begins, and the presence (or lack thereof) of a second redox peak will tell if the process is reversible or not. Intense redox peaks can signify battery behaviour if they are observable on both the forward and reverse sweep.[89] The area under or within the displayed curve represents the charge stored in Coulombs. Two examples of typical CV curves found in energy storage work are displayed in Figure 2.8.

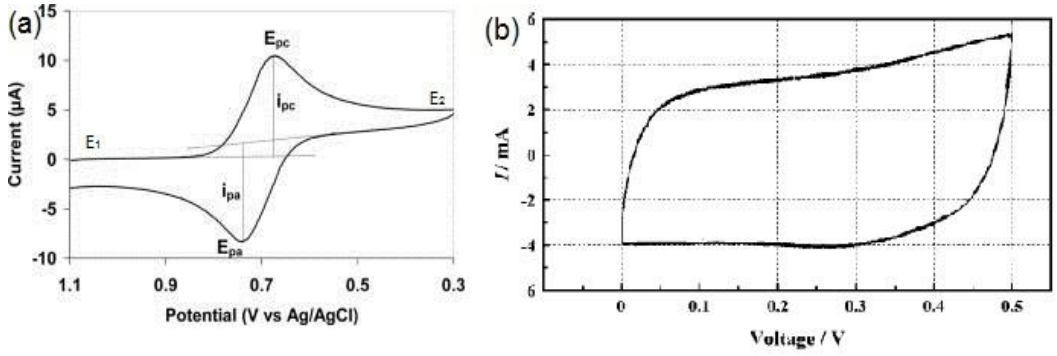

Figure 2.10: Sample CV curves for devices storing charge (a) through redox reactions and (b) through double layer capacitance. (a) adapted from Wikipedia under creative commons, (b) adapted from https://electronics.stackexchange.com.

Figure 2.10 (a) shows the typical CV curved from a material or device that is storing energy through redox reactions. The cycle begins at potential E_1 and the potential is changed at a steady rate, known as the scan rate (in V or mV s^{-1}), to potential E_2, and then reversed at the same rate back to E_1. This can either be in a positive or negative direction, depending on the cell configuration and the charge state of the material. E_1, the initial potential, is usually selected to give the cell a negligible initial current. From the graph, we can see that when the voltage is sufficiently low enough, reduction in the electrode begins, and the cathodic current increases. This increase continues until the amount of un-reduced material in the electrode is at a

low enough concentration to cause the current to peak, marked on the curve as E_{pc}. This current is the peak cathodic current. This peak current then decays until the electrode material has been reduced. The scan direction then reverses at potential E_2, and the potential steadily increases. When the voltage becomes sufficiently high enough, the electrode material will begin to oxidise, and the anodic current will increase, once again increasing to a peak value E_{pa} in a similar manner to the cathodic current. After this peak is passed, the current will begin to decay until the initial cell potential E_1 is reached once more, completing the cycle.[88,90,91] The Nernst Equation governs the equilibrium conditions that are to be found at the electrode during the entirety of the scan length[90]

$$E = E_0^f + \frac{RT}{zF} ln \frac{c_o}{c_r} \tag{2.5}$$

Where E is the cell potential, E_0^f is the standard cell potential, R is the gas constant, T is the temperature, F is Faraday's constant, z is the number of electrons transferred in the reaction c_o is the concentration of oxidised species and c_r is the concentration of reduced species.

The second graph, (b), is that displayed of a supercapacitive material when subjected to cyclic voltammetry. As discussed in the previous chapter, the current response of a cell displaying double layer capacitance should be linear to the rate of change of potential. Utilising constant scan rates should therefore produce a rectangular CV response. In addition, the charge stored should be constant across the entirety of the voltage window. These conditions give rise to the shape of the graph seen in Figure 2.10 (b). There should be no observable redox peaks within the CV curve unless pseudocapacitive materials are utilised.

Electrochemical testing and specifically cyclic voltammetry forms a significant part of chapter 4 of this work, detailing the electrochemical testing of printed in-situ TEM electrodes. Information and technical details specific to those experiments will be fully detailed in the relevant chapter.

Conclusions

This chapter is intended to present the experimental methods used through this work. The two most important techniques presented are TEM and inkjet printing

and more specific information regarding their function in this work will be given in Chapters 3 and 4.

Bibliography

1. Williams, D. B. & Carter, C. B. in *Transmission Electron Microscopy* 3–22 (Springer US, 2009). doi:10.1007/978-0-387-76501-3_1

2. De Broglie, L. Recherches sur la théorie des Quanta. *Ann. Phys. (Paris).* **10,** 22–128 (1925).

3. Williams, D. B. & Carter, C. B. in *Transmission Electron Microscopy* 91–114 (Springer US, 2009). doi:10.1007/978-0-387-76501-3_6

4. Ruska, E. & Knoll, M. Die magnetische Sammelspule für schnelle Elektronenstrahlen. *Z. Tech. Phys.* **12,** 389 (1931).

5. Williams, D. B. & Carter, C. B. in *Transmission Electron Microscopy* 73–89 (Springer US, 2009). doi:10.1007/978-0-387-76501-3_5

6. Williams, D. B. & Carter, C. B. in *Transmission Electron Microscopy* 197–209 (Springer US, 2009). doi:10.1007/978-0-387-76501-3_11

7. Holtz, M. E. *et al.* Nanoscale imaging of lithium ion distribution during in situ operation of battery electrode and electrolyte. *Nano Lett.* **14,** 1453–1459 (2014).

8. Williams, D. B. & Carter, C. B. in *Transmission Electron Microscopy* 141–171 (Springer US, 2009). doi:10.1007/978-0-387-76501-3_9

9. Williams, D. B. & Carter, C. B. in *Transmission Electron Microscopy* 371–388 (Springer US, 2009). doi:10.1007/978-0-387-76501-3_22

10. Goldstein, J. I. *et al.* in *Scanning Electron Microscopy and X-Ray Microanalysis* 15–28 (Springer New York, 2018). doi:10.1007/978-1-4939-6676-9_2

11. Goldstein, J. I. *et al.* in *Scanning Electron Microscopy and X-Ray Microanalysis* 29–37 (Springer New York, 2018). doi:10.1007/978-1-4939-6676-9_3

12. Goldstein, J. I. *et al.* in *Scanning Electron Microscopy and X-Ray Microanalysis* 65–91 (Springer New York, 2018). doi:10.1007/978-1-4939-6676-9_5

13. Goldstein, J. I. *et al.* in *Scanning Electron Microscopy and X-Ray Microanalysis* 111–121 (Springer New York, 2018). doi:10.1007/978-1-4939-6676-9_7

14. Goldstein, J. I. *et al.* in *Scanning Electron Microscopy and X-Ray Microanalysis* 133–146 (Springer New York, 2018). doi:10.1007/978-1-4939-6676-9_9

15. Novoselov, K. S. *et al.* Electric field in atomically thin carbon films. *Science (80-.).* **306,** 666–669 (2004).

16. Hernandez, Y. *et al.* High-yield production of graphene by liquid-phase exfoliation of graphite. *Nat. Nanotechnol.* **3,** 563–568 (2008).

17. Mendoza-Sánchez, B., Coelho, J., Pokle, A. & Nicolosi, V. A 2D graphene-

manganese oxide nanosheet hybrid synthesized by a single step liquid-phase co-exfoliation method for supercapacitor applications. *Electrochim. Acta* **174,** 696–705 (2015).

18. Coelho, J. *et al.* Manganese oxide nanosheets and a 2D hybrid of graphene-manganese oxide nanosheets synthesized by liquid-phase exfoliation. *2D Mater.* **2,** 025005 (2015).

19. Bang, G. S. *et al.* Effective Liquid-Phase Exfoliation and Sodium Ion Battery Application of MoS 2 Nanosheets. *ACS Appl. Mater. Interfaces* **6,** 7084–7089 (2014).

20. Wang, Q. H., Kalantar-Zadeh, K., Kis, A., Coleman, J. N. & Strano, M. S. Electronics and optoelectronics of two-dimensional transition metal dichalcogenides. *Nat. Nanotechnol.* **7,** 699–712 (2012).

21. Ye, H. *et al.* Liquid-Phase Exfoliation of Hexagonal Boron Nitride into Boron Nitride Nanosheets in Common Organic Solvents with Hyperbranched Polyethylene as Stabilizer. *Macromol. Chem. Phys.* **219,** 1700482 (2018).

22. Golberg, D. *et al.* Boron nitride nanotubes and nanosheets. *ACS Nano* **4,** 2979–2993 (2010).

23. Ma, R. & Sasaki, T. Nanosheets of oxides and hydroxides: Ultimate 2D charge-bearing functional crystallites. *Adv. Mater.* **22,** 5082–5104 (2010).

24. Brennen, C. E. *Cavitation and Bubble Dynamics*. *Annual Review of Fluid Mechanics* **9,** (2013).

25. Mason, T. J. & Lorimer, J. P. *Applied Sonochemistry*. **0,** (2002).

26. Blake, J. R. & Gibson, D. C. Cavitation Bubbles Near Boundaries. *Annu. Rev. Fluid Mech.* **19,** 99–123 (1987).

27. Tang, C. ., Cheng, F. . & Man, H. . Improvement in cavitation erosion resistance of a copper-based propeller alloy by laser surface melting. *Surf. Coatings Technol.* **182,** 300–307 (2004).

28. Dular, M., Bachert, B., Stoffel, B. & Širok, B. Relationship between cavitation structures and cavitation damage. *Wear* **257,** 1176–1184 (2004).

29. Devine, J. Applications of ultrasound. *Tech. Text. Int.* **29,** 14–17 (1993).

30. Supponen, O., Obreschkow, D., Kobel, P. & Farhat, M. Detailed Jet Dynamics in a Collapsing Bubble. *J. Phys. Conf. Ser.* **656,** 012038 (2015).

31. Xu, H., Zeiger, B. W. & Suslick, K. S. Sonochemical synthesis of nanomaterials. *Chem. Soc. Rev.* **42,** 2555–2567 (2013).

32. Amiri, A., Naraghi, M., Ahmadi, G., Soleymaniha, M. & Shanbedi, M. A review on liquid-phase exfoliation for scalable production of pure graphene, wrinkled, crumpled and functionalized graphene and challenges. *FlatChem* **8,** 40–71 (2018).

33. Ciesielski, A. & Samorì, P. Graphene via sonication assisted liquid-phase exfoliation. *Chem. Soc. Rev.* **43,** 381–398 (2014).

34. Khan, U., O'Neill, A., Lotya, M., De, S. & Coleman, J. N. High-Concentration Solvent Exfoliation of Graphene. *Small* **6,** 864–871 (2010).

35. Barton, A. F. M. Solubility parameters. *Chem. Rev.* **75,** 731–753 (1975).

36. Bergin, S. D. *et al.* Multicomponent solubility parameters for single-walled carbon nanotube-solvent mixtures. *ACS Nano* **3,** 2340–2350 (2009).

37. Coleman, J. N. Liquid-phase exfoliation of nanotubes and graphene. *Adv. Funct. Mater.* **19,** 3680–3695 (2009).

38. Rubinstein, M. C. R. *Polymer physics*. (Oxford University Press, 2003). at <http://www.oupcanada.com/catalog/9780198520597.html>

39. Hildebrand, J. H. Solubility. XII. Regular solutions. *J. Am. Chem. Soc.* **51,** 66–80 (1929).

40. HANSEN, C. M. THE U N IVE RS A L i TY OF THE SOLUBILITY PARAMETER. *l&EC Prod. Res. Dev.* **8,** 589–604 (1969).

41. Hansen, C. *Hansen Solubility Parameters*. (CRC Press, 2007). doi:10.1201/9781420006834

42. Coleman, J. N. *et al.* Two-dimensional nanosheets produced by liquid exfoliation of layered materials. *Science (80-.).* **331,** 568–571 (2011).

43. Coleman, J. N. Liquid exfoliation of defect-free graphene. *Acc. Chem. Res.* **46,** 14–22 (2013).

44. Khan, U. *et al.* Size selection of dispersed, exfoliated graphene flakes by controlled centrifugation. *Carbon N. Y.* **50,** 470–475 (2012).

45. Nirmalraj, P. N., Lutz, T., Kumar, S., Duesberg, G. S. & Boland, J. J. Nanoscale Mapping of Electrical Resistivity and Connectivity in Graphene Strips and Networks. *Nano Lett.* **11,** 16–22 (2011).

46. Gong, L. *et al.* Interfacial Stress Transfer in a Graphene Monolayer Nanocomposite. *Adv. Mater.* **22,** 2694–2697 (2010).

47. Singh, M., Haverinen, H. M., Dhagat, P. & Jabbour, G. E. Inkjet printing-process and its applications. *Adv. Mater.* **22,** 673–685 (2010).

48. Mannerbro, R., Ranlöf, M., Robinson, N. & Forchheimer, R. Inkjet printed electrochemical organic electronics. *Synth. Met.* **158,** 556–560 (2008).

49. Torrisi, F. *et al.* Inkjet-printed graphene electronics. *ACS Nano* **6,** 2992–3006 (2012).

50. Krebs, F. C. Fabrication and processing of polymer solar cells: A review of printing and coating techniques. *Sol. Energy Mater. Sol. Cells* **93,** 394–412 (2009).

51. Dimatix-Fujifilm Inc. Dimatix Materials Printer DMP-2831 | Deposition Products | Industrial Inkjet Printheads | Fujifilm USA. at <http://www.fujifilmusa.com/products/industrial_inkjet_printheads/deposition-products/dmp-2800/#overview>

52. Kelly, A. G. *et al.* All-printed thin-film transistors from networks of liquid-exfoliated nanosheets. *Science (80-.).* **356,** 69–73 (2017).

53. Beecher, P. *et al.* Ink-jet printing of carbon nanotube thin film transistors. *J. Appl. Phys.* **102,** 1–7 (2007).

54. Yan, H. *et al.* A high-mobility electron-transporting polymer for printed transistors. *Nature* **457,** 679–686 (2009).

55. Ko, S. H. *et al.* All-inkjet-printed flexible electronics fabrication on a polymer substrate by low-temperature high-resolution selective laser sintering of metal nanoparticles. *Nanotechnology* **18,** 345202 (2007).

56. Carey, T. *et al.* Fully inkjet-printed two-dimensional material field-effect heterojunctions for wearable and textile electronics. *Nat. Commun.* **8,** 1202 (2017).

57. Eom, S. H. *et al.* Polymer solar cells based on inkjet-printed PEDOT:PSS layer. *Org. Electron. physics, Mater. Appl.* **10,** 536–542 (2009).

58. Hoth, C. N., Choulis, S. A., Schilinsky, P. & Brabec, C. J. High photovoltaic performance of inkjet printed polymer:Fullerene blends. *Adv. Mater.* **19,** 3973–3978 (2007).

59. Lu, H. *et al.* Inkjet printed silver nanowire network as top electrode for semi-transparent organic photovoltaic devices. *Appl. Phys. Lett.* **106,** 093302 (2015).

60. Jung, J., Kim, D., Lim, J., Lee, C. & Yoon, S. C. Highly efficient inkjet-printed organic photovoltaic cells. *Jpn. J. Appl. Phys.* **49,** 05EB03 (2010).

61. Steirer, K. X. *et al.* Ultrasonically sprayed and inkjet printed thin film electrodes for organic solar cells. *Thin Solid Films* **517,** 2781–2786 (2009).

62. Villani, F. *et al.* Inkjet printed polymer layer on flexible substrate for OLED applications. *J. Phys. Chem. C* **113,** 13398–13402 (2009).

63. Haverinen, H. M., Myllylä, R. A., Jabbour, G. E. & Jabbour, G. E. Inkjet Printed RGB Quantum Dot-Hybrid LED. *IEEE/OSA J. Disp. Technol.* **6,** 87–89 (2010).

64. McManus, D. *et al.* Water-based and biocompatible 2D crystal inks for all-inkjet-printed heterostructures. *Nat. Nanotechnol.* **12,** 343–350 (2017).

65. Rida, A., Yang, L., Vyas, R. & Tentzeris, M. M. Conductive inkjet-printed antennas on flexible low-cost paper-based substrates for RFID and WSN applications. *IEEE Antennas Propag. Mag.* **51,** 13–23 (2009).

66. Subramanian, V. *et al.* Progress toward development of all-printed RFID tags: Materials, processes, and devices. *Proc. IEEE* **93,** 1330–1338 (2005).

67. Kamyshny, A. & Magdassi, S. Conductive nanomaterials for printed electronics. *Small* **10,** 3515–3535 (2014).

68. Eom, S. H., Seo, Y. & Lim, S. Pattern switchable antenna system using inkjet-printed directional bow-tie for bi-direction sensing applications. *Sensors (Switzerland)* **15,** 31171–31179 (2015).

69. Kraft, T. M., Berger, P. R. & Lupo, D. Printed and organic diodes: Devices, circuits and applications. *Flex. Print. Electron.* **2,** 033001 (2017).

70. Chen, P. *et al.* Fully printed separated carbon nanotube thin film transistor circuits and its application in organic light emitting diode control. *Nano Lett.* **11,** 5301–5308 (2011).

71. Siegel, A. C. *et al.* Foldable printed circuit boards on paper substrates. *Adv. Funct. Mater.* **20,** 28–35 (2010).

72. Lee, D.-H., Han, S.-Y., Herman, G. S. & Chang, C. Inkjet printed high-mobility indium zinc tin oxide thin film transistors. *J. Mater. Chem.* **19,** 3135 (2009).

73. Xu, Y. *et al.* Inkjet-printed energy storage device using graphene/polyaniline inks. *J. Power Sources* **248,** 483–488 (2014).

74. Le, H. P. Progress and trends in ink-jet printing technology. *J. Imaging Sci. Technol.* **42,** 49–62 (1998).

75. Calvert, P. Inkjet printing for materials and devices. *Chem. Mater.* **13,** 3299–3305 (2001).

76. Slade, C. E. & Evans, J. R. G. Freeforming ceramics using a thermal jet printer. *J. Mater. Sci. Lett.* **17,** 1669–1671 (1998).

77. Derby, B. Additive Manufacture of Ceramics Components by Inkjet Printing. *Engineering* **1,** 113–123 (2015).

78. Fromm, J. E. Numerical Calculation of the Fluid Dynamics of Drop-on-Demand Jets. *IBM J. Res. Dev.* **28,** 322–333 (1984).

79. Derby, B. & Reis, N. Inkjet Printing of Highly Loaded Particulate Suspensions. *MRS Bull.* **28,** 815–818 (2003).

80. Dong, H., Carr, W. W. & Morris, J. F. An experimental study of drop-on-demand drop formation. *Phys. Fluids* **18,** 072102 (2006).

81. Hsiao, W.-K., Hoath, S. D., Martin, G. D. & Hutchings, I. M. Ink Jet Printing for Direct Mask Deposition in Printed Circuit Board Fabrication. *J. Imaging Sci. Technol.* **53,** 050304 (2009).

82. Technotes. at <http://www.microfab.com/technotes>

83. Finn, D. J. *et al.* Inkjet deposition of liquid-exfoliated graphene and MoS<inf>2</inf> nanosheets for printed device applications. *J. Mater. Chem. C* **2,** 925–932 (2014).

84. De Gans, B. J., Kazancioglu, E., Meyer, W. & Schubert, U. S. Ink-jet Printing Polymers and Polymer Libraries Using Micropipettes. *Macromol. Rapid Commun.* **25,** 292–296 (2004).

85. Kuang, M., Wang, L. & Song, Y. Controllable Printing Droplets for High-Resolution Patterns. *Adv. Mater.* **26,** 6950–6958 (2014).

86. Torkkeli, A. Droplet microfluidics on a planar surface. *VTT Publ.* **7,** 3–194 (2003).

87. de Gennes, P.-G., Brochard-Wyart, F. & Quéré, D. in *Capillarity and Wetting Phenomena* 1–31 (Springer New York, 2004). doi:10.1007/978-0-387-21656-0_1

88. Kissinger, P. T. & Heineman, W. R. Cyclic voltammetry. *J. Chem. Educ.* **60,** 702 (1983).

89. Bruce, P. G., Armstrong, A. R. & Gitzendanner, R. L. New intercalation

compounds for lithium batteries: Layered LiMnO2. *J. Mater. Chem.* **9,** 193–198 (1999).

90. Compton, R. G., Laborda, E. & Ward, K. R. *Understanding Voltammetry*. (IMPERIAL COLLEGE PRESS, 2014). doi:10.1142/p910

91. Hamann, C. H., Hamnett, A. & Vielstich, W. *Electrochemistry*. (Wiley-VCH, 2007). at <https://www.wiley.com/en-ie/Electrochemistry,+2nd,+Completely+Revised+and+Updated+Edition-p-9783527310692>

Chapter 3: Inkjet Printing of In-Situ TEM Electrodes

3.1 The Need for In-Situ Analysis

To improve the capacity and efficiency of energy storage devices, we must fully understand how the materials that make up these devices change during the charge and discharge process. Of particular importance is understanding how these materials degrade and fail. As batteries and supercapacitors are designed to hold more and more energy, and to charge and discharge at increasingly high rates, safety and reliability is vital. While the morphological and chemical changes that the materials undergo during this process can be inferred from post-mortem studies of used devices, this is not always the case. Li ion secondary batteries exist in a closed environment. These battery materials are highly reactive and unstable, and the atmospheric exposure required to examine them renders much of the information obtained useless. It is for this reason that in-situ and operando studies of these materials is required. The ability to analyse energy storing materials in conditions similar to those that would be present within a full device is important, and thus has been the focus of significant amounts of research. For energy storage materials, this generally means examining the materials while they are immersed in, or at the very least in contact with, a liquid electrolyte.

In-situ TEM studies represents the best opportunity for collecting meaningful chemical and morphological data on energy storage materials. There are currently numerous specialised TEM holders on the market, designed for examining liquids and materials in liquids. When coupled with the capability to introduce electric currents to the liquid environment, these holders can be very powerful tools in the analysis of nanomaterials as used in energy storage electrodes. Despite the field itself being nascent, with most original studies focussing on biological samples in liquids[1,2], there has been considerable findings over the last number of years, particularly with respect to dendrite and solid electrolyte interphase (SEI) formation[3–5].

The experimental methods of this process are not trivial. The microelectrode structures must be fabricated within a very small space, with the working counter and reference electrodes of the cells used in this thesis separated by a distance of 20 µm. When coupled with the fragile nature of the chips, and the electron transparent window of the cell being 20 nm thick, a very considered approach must be adopted in the preparation of these devices. In most published material, the focussed ion beam (FIB) is the primary method of fabricating the in-situ electrodes.

In addition to these fabrication problems, a number of technical hurdles exist in imaging liquid cell samples. The presence of liquid layers inhibits high resolution image acquisition and precludes many of the chemical spectroscopic techniques such as electron energy low loss spectroscopy (EELS) and energy dispersive x-ray spectroscopy (EDX spectroscopy).

A further experimental hazard that must be considered is the effect of the electron beam. This effect can be twofold in micro-electrochemical systems like those shown. Firstly, the electrolytes are susceptible to damage and degradation from the beam. Appropriate electrolytes that are not beam sensitive must be chosen for these systems. Secondly, it is possible for the energy imparted by the beam itself to induce electrochemical changes within the cell. These beam induced changes must be differentiated from morphological and chemical changes that occur due to the electrochemical cycling. In an ideal situation, these beam induced changes would be completely eliminated from consideration.

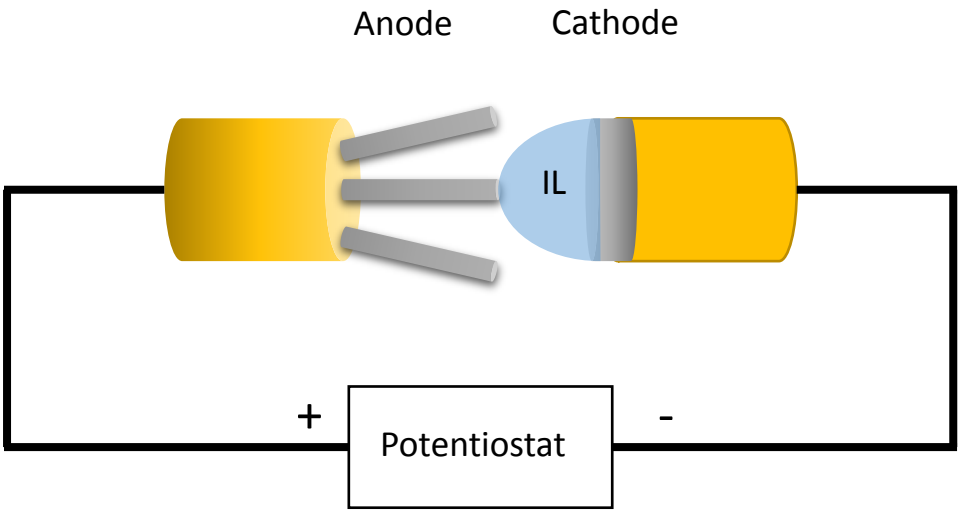

Figure 3.1: A schematic diagram of a typical Open Liquid Cell. An anode, typically formed from a nanowire welded or epoxied to a gold electrode is immersed in an Ionic Liquid Electrolyte (ILE) which is in turn in contact with a cathode material (typically $LiFePO_4$ or $LiCoO_2$). Both sides are connected to an external potentiostat.

Many publications have removed some of the issues of aqueous and organic electrolytes in the TEM column by utilising an open cell configuration. This usually consists of the anode and cathode materials connected to each other with a droplet of ionic liquid electrolyte.[6,7] The open cell exposes the workings of the device to the column pressure. Due to the exceedingly low vapour pressure of the ionic liquid electrolyte, there is no evaporation and the device is safe to be operated within the TEM column pressure. Some issues do present themselves with this method. For the most part, ionic liquid electrolytes are electron opaque.[8] It is not possible to observe what is happening to the material through the electrolyte itself.

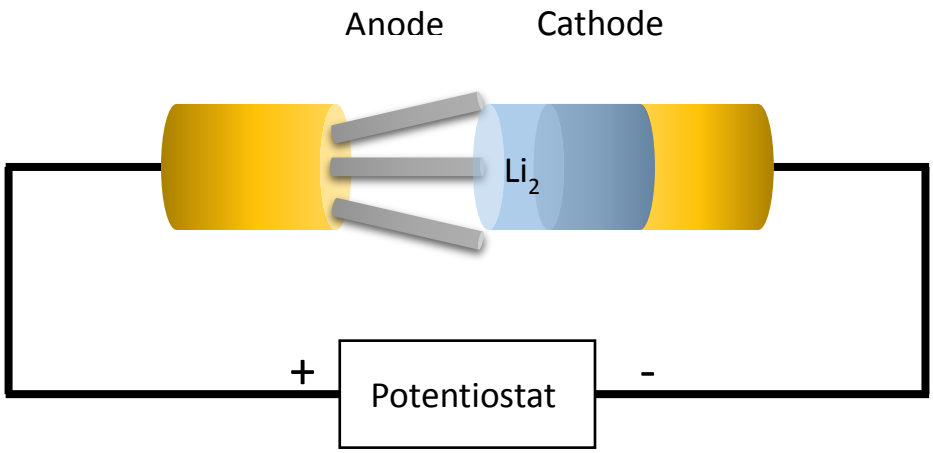

Figure 3.2: Schematic diagram of a Solid State Open Cell. In this configuration, a coating of Li2O forms over lithium metal during the process of inserting the TEM holder into the column. This layer is used as a solid-state electrolyte when it comes into contact with the anode material.

Figure 3.1 gives a basic schematic outline of the typical open liquid cell that utilises an ILE. It has been observed that for micro/nanobatteries, such as those composed of single nano-wires, beads of ionic liquid electrolyte will coat the length of the structure. While this does allow the device to function, it impedes resolution and the thin film of electrolyte is very prone to degradation and polymerization under the electron beam.[9]

Some tests have utilised a solid-state cell, mostly using the Li_2O coating that forms on lithium metal to act as the electrolyte.[10,11] As the holder is inserted into the TEM column, the surface of the pure Li electrode oxidises providing a solid-state electrolyte that completes the device.

The absence of the liquid electrolyte allows for a high degree of spatial resolution and eliminates the risk of stray droplets of liquid entering the TEM column proper

and compromising the column, vacuum, or in the worst-case scenario, the electron gun. The absence of liquid also ensures much clearer spectroscopic signals and scattered electrons to be observed, allowing techniques such as EELS and EDX to be utilised to investigate the chemical composition and changes that occur. This configuration however is not a wholly accurate representation of the function of a Lithium ion secondary battery. The Li_2O layer has a very low ionic conductivity at room temperature. In order to overcome this, a large over potential must be applied to drive the lithium ions into the electrode.[9,11,12]

While these two methods (open liquid cell and open solid-state cell) have previously been extensively been used, it is well known that there are limitations to how much information can be obtained through these methods. The primary problem is that in these open cell configurations, the electrolyte is only in point contact with the anode material rather than fully immersed in the electrolyte at all points. This point contact could inadvertently alter the Li ion diffusion process. Secondly, the open cell configuration precludes some of the phenomena that we know occur in full sized devices such as SEI formation at the electrode-electrolyte interfaces and interactions between the electrolyte and the bulk electrode. Because of these limitations, in this work a third method of cell construction is used; a closed electrochemical liquid cell.

3.2 Liquid Cell Electrochemistry

Liquid cell electrochemistry is the primary method of addressing the shortcomings of the two traditionally used open cell methods. Liquid cell techniques present an opportunity to conduct not just *in-situ* but also operando (full analysis during external stimulation such as cyclic voltammetry) testing of energy storage materials. Using liquid cells allows for a close representation of the inner workings of a battery or supercapacitor to be reproduced. Relevant electrodes and electrolytes can be used in a closed environment, ignoring some of the fundamental limitations of the open cell structure. The entirety of the electrode and material maintains contact in a full closed liquid cell, allowing for reasonable replication of diffusion pathways that appear in full devices. The interface between the electrode material and electrolyte can be closely probed, unlike in the open liquid cell configuration. Electrolyte selection must be carefully considered as some electrolytes degrade and behave unusually under high intensity electron beams. Aqueous and organic

electrolytes are electron transparent, and allow for direct morphological analysis unlike experiments performed using electron opaque ionic liquid electrolytes.

The closed liquid cell consists of electrodes and electrolyte closed within a cell that can be held within a TEM holder, some of which allow for electrical signals to be induced onto the electrodes. The original liquid cells were fabricated within research groups and varied in appearance and experimental operation,[13,14] however in recent years more sophisticated commercial liquid cell assemblies from Hummingbird Scientific and Protochips have enabled standardised liquid cell testing. These commercial cells differ in fine architecture, but are fundamentally similar. They consist of pairs of Si chips with a thin layer of SiN_X. The Si is etched away at overlapping points to form electron transparent windows, measuring 200 µm X 50 µm, through which the electron beam can pass. The basic schematic of the cell itself is given in Figure 3.3.

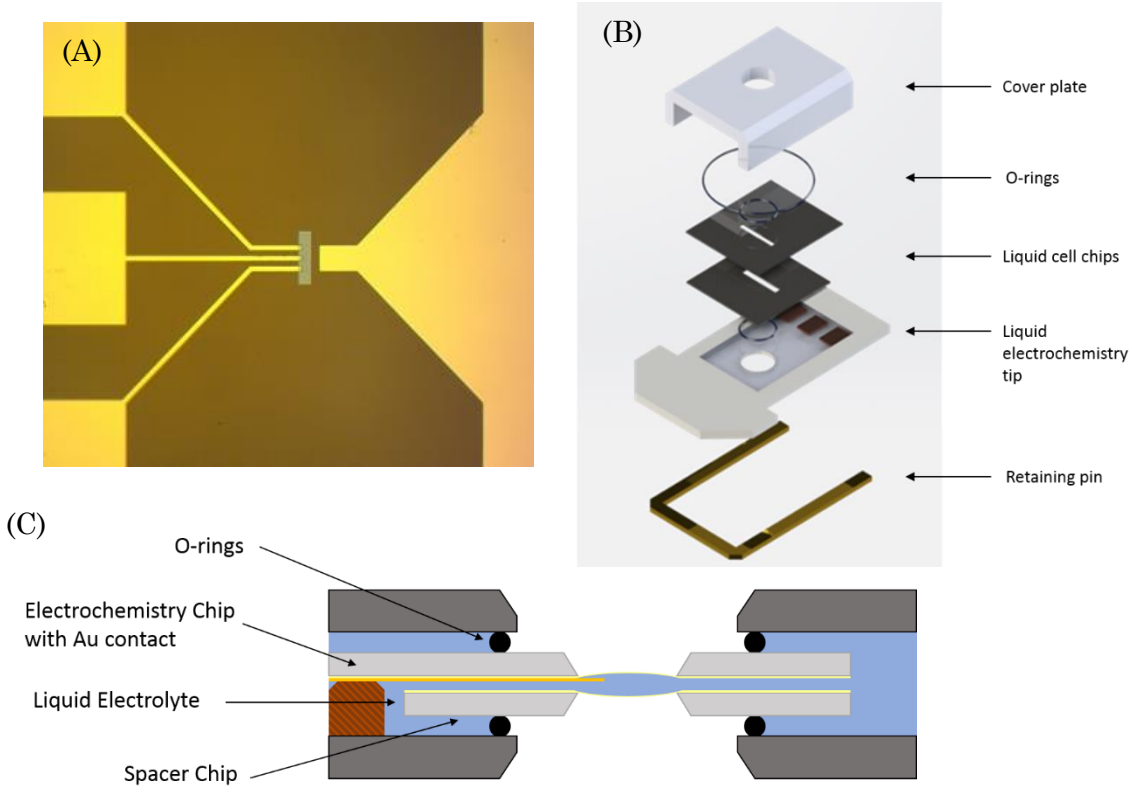

Figure 3.3: The Liquid Cell Holder and Chips. (A), a blank liquid cell chip with visible window and three Au electrodes leading into the viewing area. The Au electrodes are 20µm wide, (B) an exploded view of the liquid cell TEM assembly. This tip is inserted into the liquid cell holder which in turn is inserted into the TEM column for imaging. Note the top cover plate narrows the field of view limiting certain functions such as EELS, EDX and HAADF analysis. (C) shows the schematic elevation view of the assembled cell.

The larger of the two Si chips is the electrochemistry chip. On the electrochemistry chip, three metal electrodes extend into the viewing window. These electrodes are

20 μm wide, and are spaced 20 μm from each other. These electrodes extend towards the rear of the cell and expand to contact pads, which connect to electric contacts at the rear of the TEM holder. The second chip is known as the spacer chip. This chip consists of a square Si piece, with the same centrally located SiN_X window which overlaps with the window of the electrochemistry cell.

Adjoining each side of the chip is a patterned layer of SU8 (an epoxy based negative photoresist). This SU8 has a dual function within the cell. The first is to create a narrow channel within which the electrolyte can be contained (and flow, depending on the specific experimental setup). The second purpose is to isolate the large rear contacts from the liquid electrolyte. This is to ensure that the majority of the electrochemical response that is being observed is exclusively as a result of phenomena occurring within the viewing area. This layer of SU8 is provided in different thicknesses by the manufacturer which allows for different liquid film thicknesses. In practice the thinnest liquid film possible is desirable to increase resolution and decrease scattering. The sandwiched electrodes are held in place with a pair of rubber O Rings and a metallic retaining plate, which exposes only the windows to the TEM vacuum. The overall design of the tip itself is given in Fig 3.3. Full details on the theory, experimental operation and results of in-situ TEM electrochemistry and imaging for the cells presented here are contained in Chapter 4.

3.3 Fabrication of Liquid Cell Electrodes Using Nanomaterial Inks and Inkjet Printing

In this work, inkjet printing was utilised as a method of depositing material onto the metallic electrodes. This approach was chosen for a number of reasons. Firstly, this method of deposition is the same as is used for making large scale devices. This allows for a degree of consistency in terms of electrochemical data and electrode morphology. Electrodes can be patterned onto the liquid cells without any further modifications required to our inks, which have been created through liquid phase exfoliation (LPE) as described in Chapter 2. Secondly, printing allows for a larger range of materials to be deposited, hybrid dispersions in particular. FIB is the primary method of fabrication for liquid cell electrode systems, however as has been noted before, the single nanowire batteries that are common within *in-situ* electrochemistry research are less than ideal for investigating long term cycling

information and the function of full sized devices.[11,15] For these experimental set ups to provide a close analogue to full-sized devices, forests of hundreds of nanowires would have to be deposited, an expensive and time consuming task. In addition, FIB deposition has its limitations when dealing with hybrid materials.

One of the primary advantages of the inkjet printing approach is the ability to manufacture electrodes consisting of composite or hybrid materials. Many materials within the field of supercapacitors and batteries are now being functionalised with carbon nanostructures (graphene, CNTs etc) or conductive polymers.[16–22] Stable liquid dispersions of these materials can be used as inks and deposited directly onto electrochemistry chips without the need for extensive or complicated fabrication steps as would be required if the materials were to be grown directly onto the cells or transferred using FIB deposition or micromanipulation.

3.4 Optimisation of Printing Processes for IPA Nanomaterial Inks

Prior to electrochemical testing, it was necessary to conduct a full printing parameter characterisation of our ink dispersions. Certain parameters that would not normally be considered to have a large impact during the printing of large scale devices, such as droplet velocity and individual droplet repeatability were found to be important when fabricating electrode structures on micro-scale pre-fabricated architecture.

3.4.1 Ink formulation and solvent selection

For the initial printing characterisation an MnO_2 material ink was selected. The MnO_2 inks were prepared in the manner described in Ref [24]. $Mn(NO_3)H_2O$ (1.67 g) is dissolved in 100 mL of deionised water . A triblock copolymer, PEG-PPG-PEG (0.5 g) is then added. This solution is heated and maintained at 45 ^{O}C. Separately, an aqueous solution of $KMnO_4$ (100 mL, 0.1 M) is prepared. This solution is slowly dripped into the first solution, creating a precipitate which is washed sequentially with DI water and ethanol. The solution is then vacuum filtered and dried overnight, resulting in MnO_2 powder.

To create an exfoliated nanomaterial ink, bulk MnO_2 (300 mg) is added to IPA (30 mL) and sonicated in an ultrasonic bath for 3 hours at 37 kHz. Following this the

suspension is centrifuged at 5000 rpm for 3 hours to remove un-exfoliated bulk material and the top 70% of the remaining supernatant is retained, with the remainder being discarded. This supernatant is used as the MnO_2 IPA ink, without further modification

For liquid cell electrochemistry, IPA based inks were originally selected for a number reasons. The first was the availability of many stable IPA material dispersions giving a large material "toolbox" with which the experimental work could be conducted. As described in Chapter 2, many of these stable, or meta-stable, dispersions can be used for hybrid material suspensions due to the similar surface energies and solubility parameters of the solvents and materials to be dispersed.

Secondly, the low volatility of the dispersion solvent was important. Due to the eventual exposure of the Si electrochemistry cells to liquid electrolytes and given the low current ranges expected from micro-electrochemical cells, it was imperative that as little original solvent as possible remained on the surface of the cell. While extensive studies have shown that many of the 2D materials used within this work can be exfoliated and dispersed more effectively or at higher concentrations in NMP and DMF[23–29], for the purposes of this work, a lower volatility solvent in which material could be reasonably well dispersed was deemed to be more desirable. Spreading of the liquid droplets and the ability to rapidly evaporate the printed lines was also a consideration. Since the target substrate (the prefabricated electrochemistry cells) was fixed, there is no real opportunity to change the surface chemistry or energy. Heating is the only feasible way to modify the surface during the printing process,[30,31] and so IPA satisfied this requirement once again.

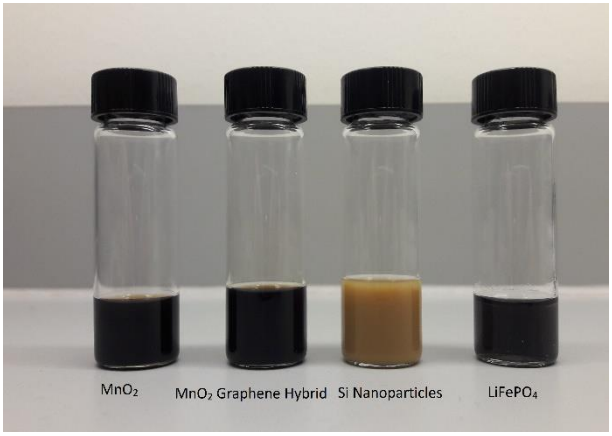

Figure 3.4: An example of a range of IPA based nanomaterial-based dispersions. Used in this work. The MnO_2-Graphene Hybrid and Si nanoparticle inks are examples of high concentration (~ 10 mg mL^{-1}) stable ink dispersions.

3.4.2 Characterisation of printed IPA Droplets and Lines

Once appropriate solvents/inks were selected, the initial printing phase was designed to characterise how these inks would wet and spread on the SiN_x layered cells. Initially, the appropriate waveform development to create a fully jettable droplet was undertaken (described in full in Chapter 2). For large scale printing projects, long term droplet stability and clogging are major factors in generating stable printed droplets. However, for the small-scale devices presented in this section, this was less of a concern. A large interdigitated supercapacitor may consist of hundreds of thousands of overlapping droplets, printed over the course of multiple passes. For these devices it is vital for the ink dispersions to maintain a stable droplet over the course of multiple minutes and hours (depending on ink concentration and desired film thickness). However, the electrodes designed to be printed onto electrochemical TEM cells are in the order of hundreds of microns long and tens of microns in width, and therefore consisted of only a few droplets. This makes long term droplet stability less of a concern, as droplets need only be completely stable over the course of the 5 or so seconds required to deposit the required amount of material.

Some short time scale stability issues do remain, however. The most important of these stability concerns is that accurate droplet placement relies on a consistent droplet trajectory, and even small deviations of the in-flight droplet can cause severe positional errors that would not be noticeable on larger devices. The largest contribution to trajectory errors is usually an accumulation of material at the nozzle edge[32], which can directly deflect the path of the droplet. The primary printing nozzle used must be kept clear of accumulated material to ensure accurate electrode placement. A secondary point to note is the agglomeration that can occur in inks where the solvent and solute have been poorly matched. The theory of liquid phase exfoliation, discussed in Chapter 2, showed how a poorly matched suspension will have a tendency to agglomerate. With agglomeration, the particle size of the material within the suspension rises, possibly coming close to the size limit of printable material usually $\frac{1}{20}th$ of the nozzle diameter (in this case a nozzle size of 21 µm, giving a limit of 1 µm). While these limits are only guidelines, they do have an effect on the stability of the generated droplets and the trajectory of ejected droplets can be affected by an accumulation of oversized particle aggregates. In

short, while a dispersion does not necessarily have to have long term stability for this kind of printing, it is largely recommended that it is stable.

Initial tests of line formation were undertaken with a 0.1 mg ml^{-1} IPA dispersion of MnO_2. These tests were primarily intended to provide a base level of understanding on how the liquid behaved in contact with the SiN_x layer. Of primary interest was how the liquid wetted the substrate and the degree to which the printed patterns were affected by coffee staining. Multiple passes were printed outside of the window area to determine the wetting and spreading properties of the inks.

These initial tests showed that the lines printed experience severe coffee staining. Even after multiple printed passes almost no material remains on the interior of the printed features. The only significant material deposits within the line structure come from droplets that have miss fired or otherwise unintentionally deposited away from their intended target. In addition, the printed structures are very large when compared with the size of the electrode architecture of the chip. The Au electrodes of the cell are 20 µm wide and are spaced 20 µm microns from each other. In comparison the lines printed are on average 112 (±5) µm.

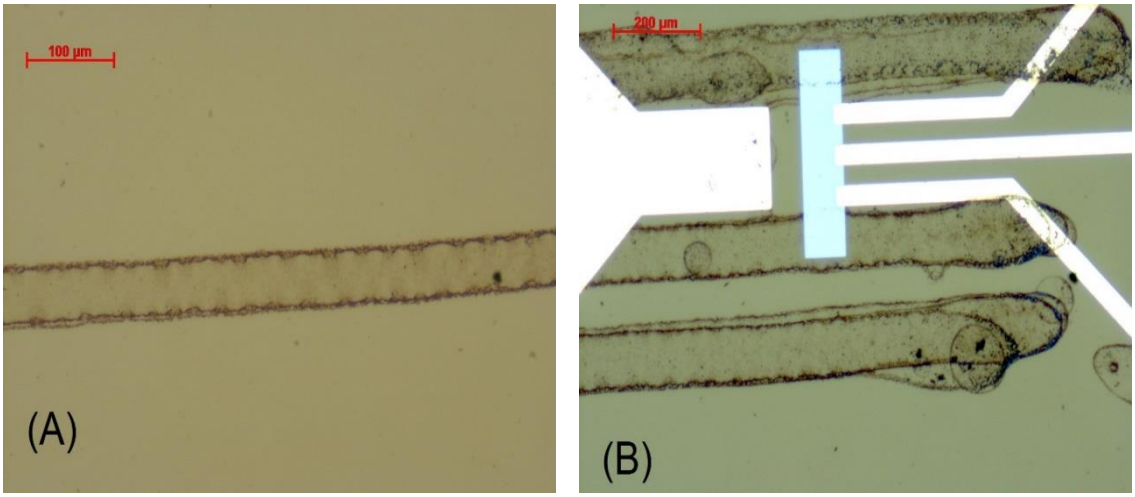

Figure 3.5: MnO2 from an IPA based ink deposited on the SiNx thin film of an electrochemistry chip. In image (A) the coffee staining effect can be prominently seen. Most of the deposited material has migrated during the drying process to the edge of the lines. In image (B) the printing errors that are introduced from stray droplets can be seen in the bottom printed line. The coffee staining is once again very prominent.

The primary print parameters that can be manipulated outside of tuning the properties of the ink itself are the driving voltage of the nozzle piezo (V), the droplet spacing (d), the print height (h) and the substrate temperature (T). Droplet spacing primarily serves to determine the distance between the droplets deposited in a particular pattern. The Dimatix DMP 2800 printer software generates the formed

patterns as a series of consecutive droplets and it is up to the user to determine the wetting characteristics of the ink, and what the appropriate spacing should be. If the spacing is too large, the droplets will not form a continuous line. If the spacing is larger than the total wetting radii of each pair of consecutive droplets, the pattern will not connect and will be a series of separated droplets. Poor drop spacing choice can also display what is known as a "scalloped"[33] pattern where the droplets connect but still retain rounded contact line shapes at the edge of the pattern (an example of this shape can be seen in the 70 µm droplet spacing image of Figure 3.6). While still creating a connected feature, these scalloped lines tend to have a larger feature width than a feature with a properly tuned droplet spacing. If the droplet spacing selected is too low, the deposited droplets will exhibit a tendency to pool and bulge rather than forming a continuous line. An appropriate droplet spacing is very important for accurate feature formation.

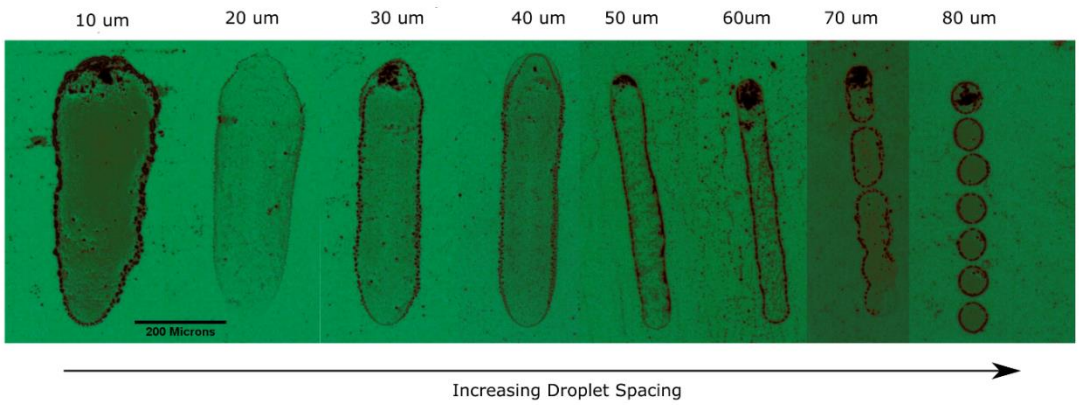

Figure 3.6: Line spreading differences depending on droplet spacing. Droplet spacing controls how close each droplet is placed to the next droplet. A lower droplet spacing for a given pattern length will give a pattern made of more droplets. The required droplet spacing depends on the wetting of the substrate. Too high droplet spacing will give non connecting droplets as seen in images for droplet spacing 70 µm and 80 µm. Too low a droplet spacing will result in high amounts of spreading in the deposited droplets as seen in the images for 10 and 20 µm spacing.

When droplets were deposited with increasing droplet spacing the narrowest line was found to occur at a spacing of 60 µm for the IPA ink. The line breaks down at higher droplet spacings than this, forming individual droplets instead of a connected line. This is shown in Figure 3.6. Determining the droplet spacing is the first objective when using a new liquid system. When using different ink solvents and droplet spacings it is important to remember that changing the droplet spacing will yield a different deposited mass per unit area.

The driving voltage of the piezoelectric diaphragm is the primary factor determining the velocity of the droplet. From experimental observations, the droplet exit velocity (the velocity of the droplet as it exits the nozzle), is directly proportional to the piezo driving voltage *V*. For a given optimised waveform, steady droplet formation was found to occur from 15V and higher. Below this value, jetting was either inconsistent, providing a highly inaccurate, irregular flow of droplets or did not occur at all. The following tests were conducted at a standard spacing of 50 µm, voltage of 24 V and print height of 500 µm at an ambient platen temperature.

It is important to note at this point that these values are of the droplet's *exit velocity* from the nozzle. The terminal velocity of a droplet of 10pL of IPA falling through air is roughly ≈ 1 m s^{-1} (assuming a spherical droplet of IPA, and ignoring buoyancy effects) and so the droplets will slow due to drag effects between the nozzles and the substrate. Accordingly, the larger the distance between the print head and the substrate, the slower the final impact will be.

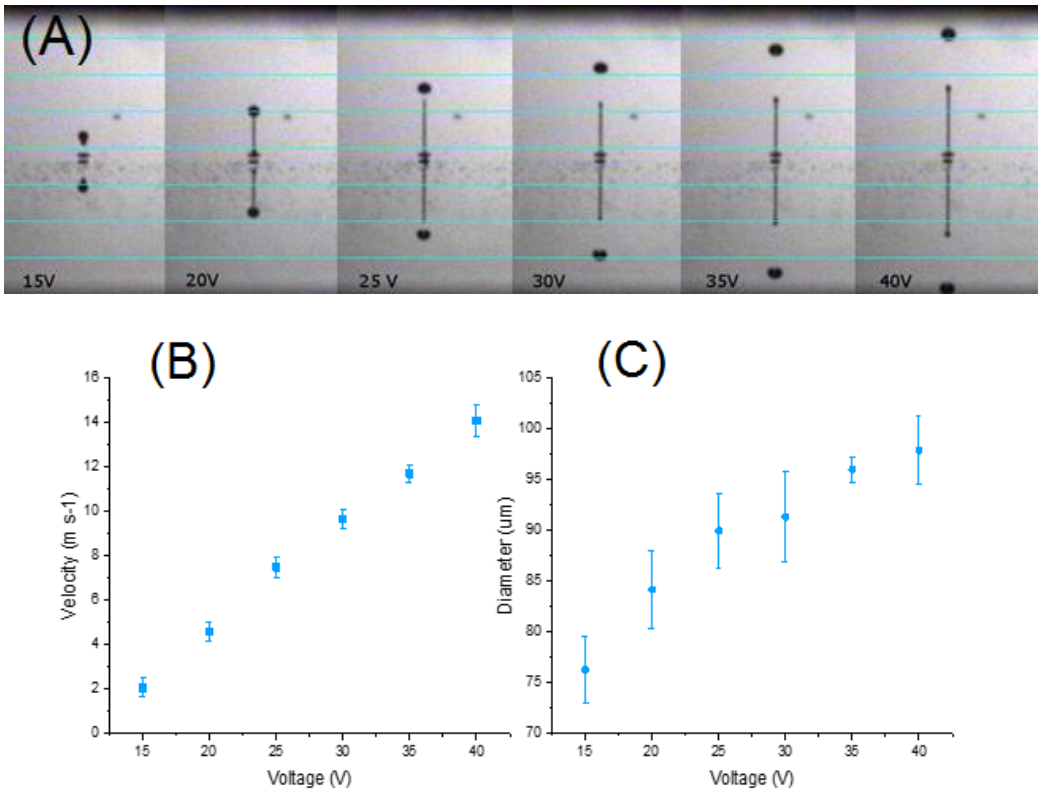

Figure 3.7: The effect of piezo driving voltage on droplet velocity and final pattern diameter. Image (A) shows the increasing velocity of a given droplet for increasing driving voltage. The strobostropic camera is set to a 37 µs delay. The exit velocity of the droplets appears to scale linearly with the driving voltage, as seen in graph (B) This in turn appears to have an effect on the final droplet diameter when deposited on the Si Chip, shown in graph (C)

Droplet velocity was seen to influence the spreading of deposited droplets at a given height and ambient temperature, as is shown in the graphs in Figure 3.7. There is a clear increase in droplet diameter as the driving voltage is increased. This effect could be in part due to a phenomenon observed for droplets impacting surfaces at a high velocity. Droplets hitting substrates at a high velocity are observed to spread or "pancake" to a far larger diameter than what would normally become their final contact line if pure viscosity and surface tension effects were considered. Depending on the velocity and the liquid used, the kinetic energy imparted is dissipated by viscous forces or converted to the surface energy associated with a much larger free surface area of the droplet, causing the droplet to recede from its maximum spreading.[34–36] However, due to differences in the advancing and receding contact angles that are associated with contact angle hysteresis, this pancaking and receding effect can cause differences in final droplet diameter and coffee staining pattern. As explained by Rooiboo *et al*[34], surface effects such as roughness and debris can have a massive effect on how a droplet spreads and recedes when impacting a surface. This can lead to deposition of perimeter droplets and material as the droplets recede, or a complete bouncing of the droplet from the surface. These factors can cause a much different deposition than what could be expected just from examining surface tension effects and Young's equation.

Higher voltages can also produce higher radius droplets, causing the final pattern to be larger. While there are a number of mechanisms at work within the system, the final consideration is that a higher driving voltage will produce a larger droplet. This is important for controlling pattern size because, as mentioned before, these tests are substrate limited; there is little or no opportunity to modify or change the substrate, and so other methods of changing our final pattern morphology must be considered.

Varying the height of the print head from the substrate affects the deposited pattern in two distinct ways. As the droplets are ejected from the print head at a velocity higher than their terminal velocity, the droplet slows as it falls due to drag. The larger the distance between print head and substrate, the longer the droplet has to decelerate and therefore the slower it will be on impact. This deceleration was observed to have a small impact on the final width of the printed structures, as shown in the graph in Figure 3.7, with the difference in width between droplets deposited at the highest position (1.5 mm) and the lowest position (200 µm) being

roughly 10 µm. The final line widths plateau as the height increases, suggesting that droplets reach their terminal velocity along the flight path at a certain height. This is useful if inks require a high voltage to jet, but a narrower final line is required. The second way that height effects the printed pattern is in terms of positional accuracy. With a higher distance between the nozzle and the substrate, droplets with an imperfect or deviating trajectory land further from the expected position, meaning patterns deposited at high height settings exhibit a large variation in their final positioning. Deviating or misplaced droplets are more common, making width tests and accurate deposition difficult at the highest height values. A combination of high voltage and a large height between substrate and the print head could mitigate these errors caused by non-straight flight paths, and could serve to be an effective means of printing lower concentration inks where a higher voltage is required to jet uniformly.

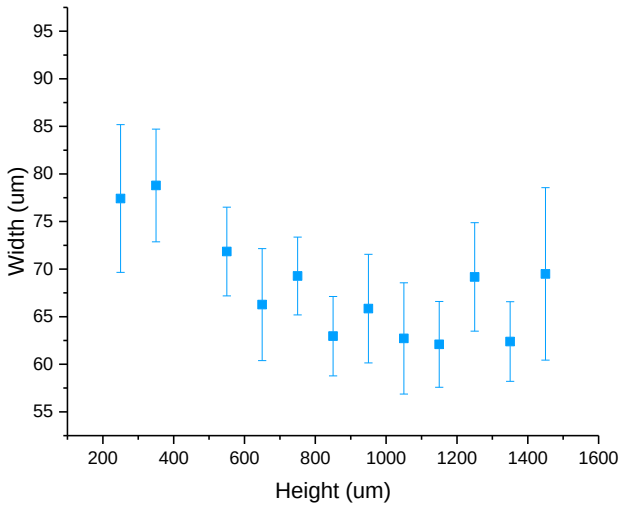

Figure 3.8: The relationship of print height to final printed feature width. The feature width decreases as height increases due to the additional drag effects experienced by the droplet. The tests were conducted at ambient temperature, with a driving voltage of 25 V, droplet spacing of 50 µm

Temperature variance is seen to have a minor effect on the spreading of deposited material. It has previously been established that for a given solid-liquid system where the deposited droplet exhibits a non-zero contact angle, increasing the temperature T will decrease the contact angle θ.[37–39] Therefore it is expected that as temperature increases for our system, the width of the deposited line should also

increase. As can be seen in Figure 3.7, the drop diameter increases until it reaches maximum wetting at 45 °C. After this point the line diameter appears to decrease.

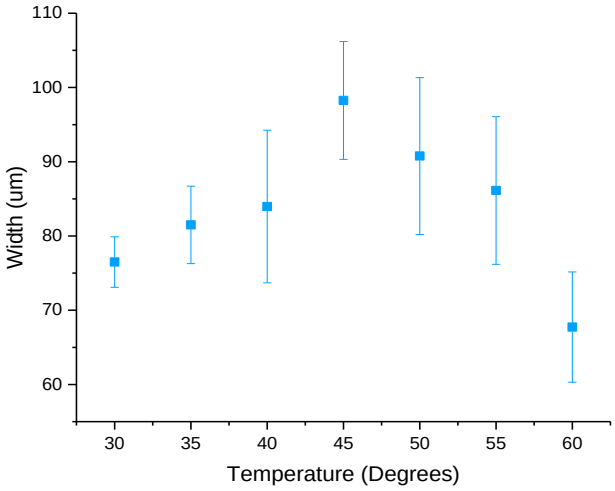

Figure 3.9: The variation of deposited line width with increasing substrate temperature. The tests were conducted with a droplet spacing of 50 µm, print height of 500 µm and driving voltage of 25 V.

The decrease in line width as the temperature increases is unexpected but can be explained by the system bypassing a critical temperature beyond which the droplet begins to evaporate before the droplet ceases movement and forms it's final pinned contact line. The same printing system was used by van Osch *et al* who reported that heating the print platen to it's maximum temperature (60 °C) reduced line spreading.[40] The boiling point of IPA is 82.6 °C so it would appear that the IPA dries rapidly at these elevated temperatures, however a thorough study with different solvents would be required to confirm this theory.

3.4.3 The Coffee Staining Effect

In the previous section one of the most visible characteristics of the deposited lines and droplets was the very visible coffee staining effect. While the characterisation conducted provided parameters for the narrowest printed pattern possible, the coffee staining effect remains pronounced for all variations. While much research has been conducted into supressing the coffee staining effect for the purposes of obtaining homogenous material depositions, many of these solutions involve either

a chemical alteration of the substrate, which was not seen to be practical in this case, or a modification of the material ink. These ink modifications usually come in two forms; the addition of a polymers or surfactants to suppress the internal capillary flow that creates the coffee stain pattern or the mixing of solvents to create a binary solvent system.[41] In the former situation, Marangoni flows are typically induced in the droplets by the presence of the surfactants. This creates a surface tension gradient which in turn re-circulates the material towards the centre of the drying droplet. This inhibits or completely reverses the capillary effects that create the coffee staining. This can also be induced by highly localised temperature gradients[42], as surface tension is affected by the temperature.

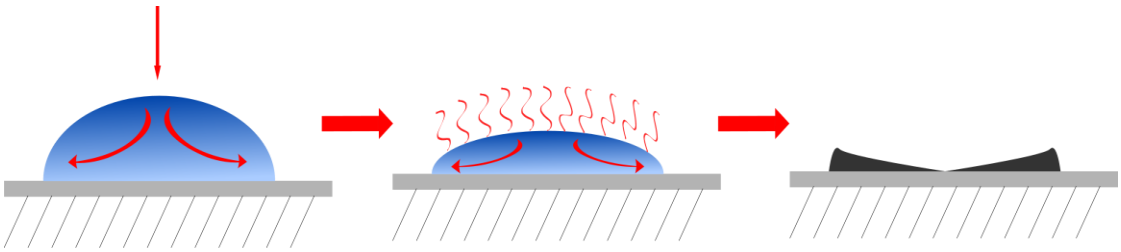

Figure 3.10: An example of typical progression of the coffee staining effect. The contact line pins when the droplet is deposited, and the droplet begins to evaporate. As the contact line is stationary, the edge must be replenished with solvent from the centre of the droplet, migrating solute towards the contact line. Finally, when the liquid is all evaporated, there is much larger amount of material deposited at the edges of where the droplet was than in the centre.

While these procedures were considered, both were deemed to present more issues than they solved. The addition of any kind of polymer or surfactant was undesirable for similar reasons stated in section 3.4.1. Due to the very low current nature of the tests involved, it was not considered practical to include additives to the inks that could drastically affect the conductivity of the small amount of material deposited. A conductive network between the material, the electrolyte and the metallic electrode is vital for inducing the physical and chemical changes required for energy storage, and a signal large enough to be visible on potentiostat software was required. Similarly the addition of different solvents after the initial characterisation phase was undesired due to the possibility of unevaporated solvents and drastically changing the stability of our liquid inks.

Another option considered was to print an excess of material, leaving significant delays between layers in order to fill in the lines, with each successive layer acting

as boundary for the next. This solution presented further complications. Firstly, there is still a requirement for the samples to be electron opaque (as discussed in the fundamentals of TEM operation in Chapter 2) in order for characterisation to be conducted. Secondly there is a practical upper limit of how much material can be deposited onto the window. Prefabricated spacers allow for a gap between the SiN_x windows ranging from 50 nm to 1 µm. When the mass of material approaches this limit, there is a high chance of the window rupturing, rendering the experiment unusable. In addition, while a larger spacer could be used, this will increase the thickness of the liquid layer that the e^- beam must pass through and dramatically increases the likelihood of secondary scattering events (as discussed in the TEM section of Chapter 2). While this would allow for an excess of deposited material and introduces the possibility of forming a homogenous film of material on the cell, the likelihood of actually being able to obtain a usable signal and resolution of the images would be low. Ideally as thin a liquid layer as possible should be used in order to fully detect morphological and chemical changes.

While some low impact surface treatments such as argon/oxygen plasma cleaning are available, this technique in particular is usually used to improve the wetting of hydrophobic surfaces, and to remove dirt. This would still not solve the issue of extensive coffee staining on the cell and would serve to increase as opposed to decreasing the total line width of the deposited pattern. When the cells are later assembled, plasma cleaning is used to enhance the spreading of the liquid electrolyte over the entirety of the cell surface.

Considering the spreading dynamics of our printed lines however, it was seen that for printing TEM electrochemistry cells that the coffee staining could in fact be beneficial rather than an inherent problem to be overcome. As can be seen from the previous Figure 3.5, the coffee staining effect on a highly wettable substrate, like the SiN_x layer used here, is extremely pronounced and results in the vast majority of the deposited material accumulating along the dried contact line of the printed feature. However, this contact line of material is much closer in width to the pre-existing electrode architecture than even the narrowest printed line (56 ± 3.54 µm narrowest printed line achievable vs 20 µm wide Au electrodes with 20 µm distance to the next electrode). Accordingly, it was decided to utilise rather than suppress the coffee stain pattern and deposit a narrow line with a large mass of usable material.

The advantages of this approach are readily apparent. Firstly, and perhaps most importantly, when the total objectives of the experimentation are considered, no modification to our ink or material are required. This means that there is a consistency between the materials that are being used in the in-situ testing and would be used for the fabrication of full scale devices. One of the primary objectives of this work is to identify the chemical and morphological changes that occur during the energy storage process. Considering this, it is not desirable to introduce any other materials or factors that would largely change the composition of our electrodes. Secondly, from a technical point of view, utilising just the contact line as opposed to the full width of the line is important when two electrode systems are considered.

For supercapacitive materials that are relying on purely electrostatic effects or redox effects between the electrode and the electrolyte, the gold electrode can function adequately as a counter electrode. However for a battery device, a two electrode system consisting of a Li based material and a Li host anode is required. It is important that there is no overlap of material either on or off the window, made much more difficult by the close packed architecture of the electrochemistry cells. At their closest approach the working and counter electrodes etched onto the cell are only 60 µm apart. In certain configurations offered by Hummingbird (depending on electrode materials), and those used in this work, the spacing is far less than this.

This characterisation step provides a framework of requirements for electrode deposition. The narrowest line possible is required, in order to maximise the density of material at the contact line and to minimise the chance of shorting between the electrodes. Ideally as few satellite droplets, or inaccurately deposited droplets as possible are needed. A single poorly placed droplet has the required diameter (>60 µm) to short all three electrodes, and once material is deposited, it is impossible to effectively remove without shattering the window. There are guidelines provided by Hummingbird Scientific for the cleaning of the electrochemistry chips. This involves successive baths in IPA, Acetone, Methanol and DI water, however it was found to not effectively remove the printed material. Any attempts at mechanical cleaning shattered the SiN_x windows instantly. While a low voltage provides narrow lines, low velocity droplets are more affected by clogging and deviating trajectories. As droplet accuracy was imperative, it was decided that an intermediate velocity (≈ 25

V) would be used to minimise both line width and the potential for greatly deviated droplets.

While the effects of the varying temperature have been mentioned before, a second effect of varying the temperature was also observed. As temperature increased, the density of material at the contact line visibly increased. At 55 ^{O}C and 60 ^{O}C the internal structure of the line fully broke down and the material no longer created a clear thing film. It has been reported previously that coffee staining increases at elevated temperatures[33] due to the increased rate of evaporation at the edges of the deposited droplets. Qualitatively it is worth noting that an elevated substrate temperature caused more frequent blockages in the print head. A non-jetting waveform maintains a meniscus of liquid at the nozzle edge at all time. This is in order to keep the printing channel wet with solvent. However, due to the low boiling point of IPA it was believed that the heated platen was evaporating the IPA interface as the print head passed over the printing area, causing a rapid accumulation of material at the nozzle edges. This is compounded by the desire to maintain the print head at as low a height as possible to minimise trajectory errors. It is therefore a matter of balancing advantages and disadvantages for each of the measured parameters. At the length scales involved in this work, and with the fine accuracy requirements, each parameter appears to have considerable impact on the others. Therefore, it was found to not be a simple matter of merely selecting the individual parameters that provided the narrowest lines in the isolated characterisation tests.

3.5 Printing of Electrodes utilising Contact Line deposition

Once the initial characterisation of how the droplets behaved on contact with the electrochemistry chips was completed, inks were prepared for printing of usable cells for in-situ electrochemistry. Electrochemistry chips were fabricated for one of two systems; a single electrode configuration for supercapacitor materials and a two-electrode system for a battery type material system.

3.5.1 Printing of Single Electrode Systems

Following on from the primary characterisation steps, a low concentration (≈ 0.1 mg ml^{-1}) dispersion of MnO_2 in IPA was selected for examining electrodes formed from the contact line depositions of the dried droplets. The low concentration dispersion was selected to give a better optical contrast between the material accumulations at the line edge to the interior of the line. Generally, a test line is printed first, off the area of the window to provide an accurate deposition position. While the repeatability of the line depositions for the Dimatix 2800 is generally excellent (within ± 25µm according to the manufacturer, but in actual fact better than this value when clogging is avoided), depending on the droplet spacing and nozzle used, the actual deposition location can vary by up to 200 µm in both x and y directions from the actual target specified. The distance between the deposition origin point in the Dimatix software and the actual deposition point of the first droplet is measured, and used as an offset for the remainder of the test. Usually this distance is calculated to the bottom edge of the printed line, so the contact line can be accurately lined up to the metallic electrode, so as to get as much material as possible in good electrical contact while still extending across the SiN_x window.

The droplet spacing used for a printed pattern is controlled by rotating the entirety of the print head, changing the x distance between the nozzles. However, this can introduce minor errors due to the nozzle being off the specified x axis during the print. This is a very minor error normally not noticeable in large scale print patterns but can be significant when printing single droplet lines onto electrochemical cells. A central nozzle is usually selected as the printing nozzle for this process for this reason (ideally nozzle 8, the central nozzle and the centre of the axis about which the print head rotates).

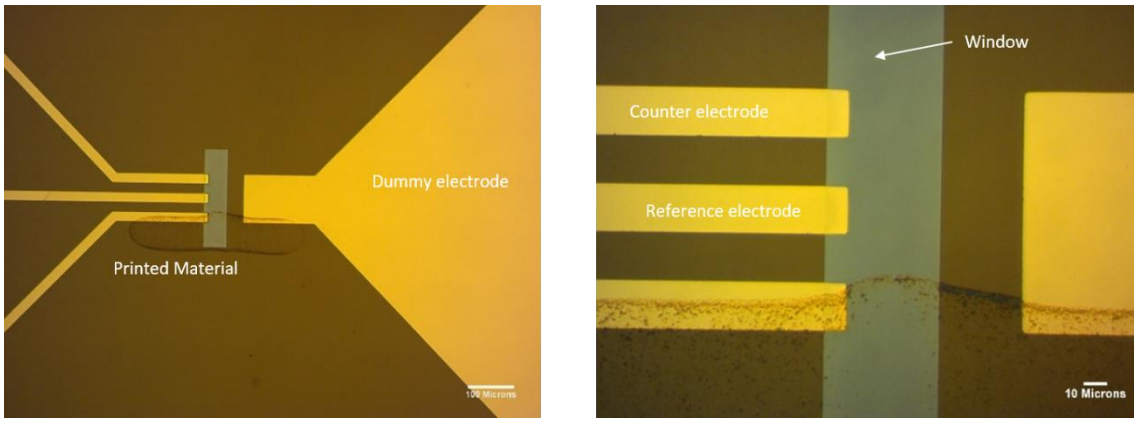

Figure 3.11: Optical Microscope Images of a dilute suspension of MnO2 in IPA printed onto the SiNx chip. The contact line has been deposited in line with the electrode.

Figure 3.11 displays the initial tests for creating a contact line based electrode. A single printed pass of dilute material was deposited across the Au electrode. From the images in Figure 3.11 we can see that the Dimatix printer can print lines with a high enough accuracy for the pinned contact line to be utilised as the electrode. The dilute nature of this particular dispersion precluded it from actually being tested electrochemically. It is clear from the higher magnification image that there has not been enough material deposited in order to form what could be a conductive network. The right-hand side electrode is a dummy electrode, so it is not necessary for the conductive network to extend fully across the window, only enough material as is required to generate a clear electrochemical response.

From this initial test shown in Figure 3.11 it is clear that either more material or at the very least a higher concentration ink would be required. For the next step a Hybrid MnO_2-Graphene ink was to be used, in order to provide a high enough conductivity for the cell to be usable. The synthesis and characterisation of this hybrid material is fully detailed in Ref [24] and involved a single co-exfoliation step. 300 mg of bulk MnO_2 powder (as synthesised in section 3.4.1) and 300 mg of as purchased graphite flakes were dispersed in 30 mL of IPA. This suspensions was then sonicated for 18 hours, and centrifuged at 5000 rpm for 3 hours. The top 70% of the supernatant was taken as the ink. This was then further filtered and re-dispersed to increase concentration.

A 10mg ml^{-1} hybrid suspension was printed using the same parameters as before, yielding a higher amount of deposited material onto the cell. A higher number of print passes, 25 passes in this case, were deposited to test both the electron transparency and spreading of additional layers deposited. The optical images and TEM images of the deposited line are given in Figure 3.12. From these images the pronounced coffee staining can be seen, however more of the interior of the line has been filled in than with printing conducted with 1 mg ml^{-1} or lower inks, or with single passes.

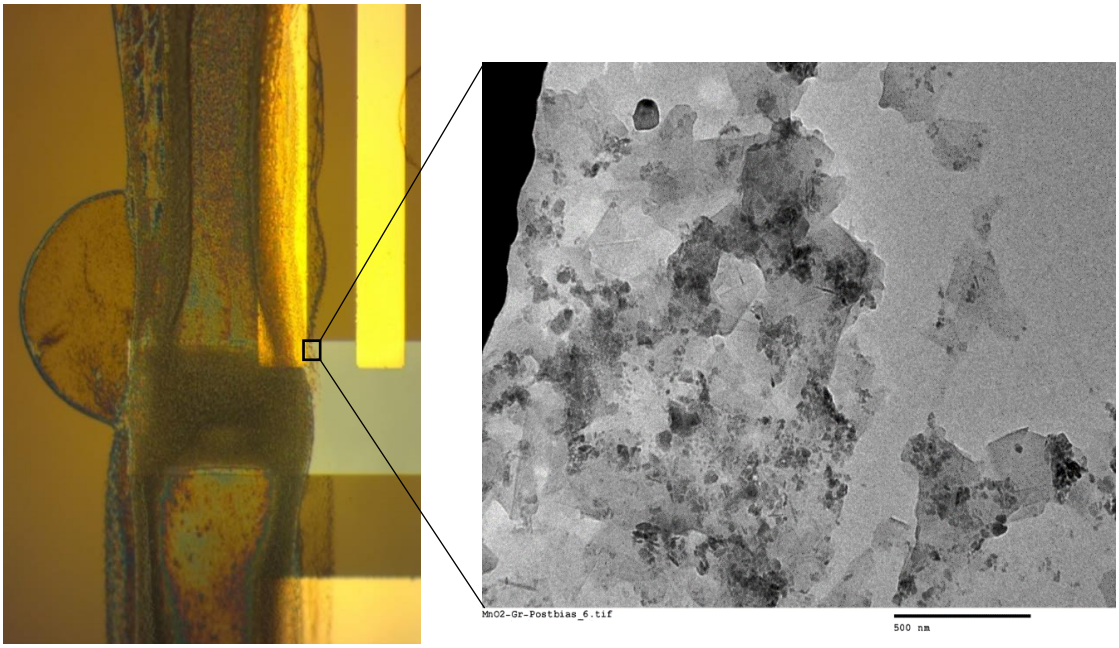

Figure 3.12: Optical Microscopy and TEM images of MnO2-Graphene (10 mg ml-1 dispersed in IPA) hybrid deposited onto the electrochemistry chip.

It is interesting to note that there appears to be a difference in how material wets between the body of the Si chip and the exposed window area, despite the whole cell being the same material and what should be a relatively flat surface. It is believed this may be due to bowing of the window under the weight of the liquid during the deposition process. It is known that the windows bow under TEM pressure, with reports from Ring *et al* reporting total window bowing bulging in the vacuum increasing the liquid layer thickness by 100%.[43,44] The windows are designed to withstand this level of bowing without shattering under most circumstances, so it is not unreasonable to believe that the weight of the deposited droplet could warp the 20 nm thick membrane. As is expected, the raised Au electrode controls the spreading of the liquid in that side of the line. While some material has deposited onto the surface of the gold itself, most of the material has migrated only as far as the SiN_x-Au interface.

Although these preliminary tests do not allow for a perfect indication of the viability of this liquid cell test, it provides some key information on cell fabrication. The previous approach yielded a large amount of material forming a contact line extending from the electrode. Under TEM examination this line was seen be electron transparent, and yet a reasonable mass of material was seen close to the electrode. In Figure 3.12 it is clearly seen that flakes of the material are in physical contact with the electrode. This is the basic condition required if morphological or chemical

changes are to be observed. A concern that is raised from the TEM imaging of the material is the amount of contrast presented by the Au electrode. As can be seen from the left-hand side of the TEM image, the Au electrode is completely opaque. There is no transmission occurring. Ideally, the material that will be imaged in liquid cell tests will be close to the Au electrode, in order to ensure that the area viewed is electrochemically active. However, the weight and thickness of the Au electrode will drastically affect the material contrast available when looking at the much lighter and thinner MnO_2-Graphene deposition. This is before the secondary scattering effects of the liquid are taken into account.

This process of printing works well for depositing single electrode systems. With proper characterisation steps and a reasonable amount of care, the electrodes can be deposited in an accurate manner using the contact line of the deposited line. Ideally a high concentration ink (within the bounds that the printer can effectively print) is used in order to minimise the number of successive passes required to print the pattern. Most importantly is the ability to deposit a hybrid material electrode with reasonable ease, something that would be very costly, difficult and time consuming for other methods such as FIB.

3.5.2 Printing of Two Electrode Systems

Following on from the confirmation that it is indeed possible to print an electrode directly onto the surface of an electrochemistry cell, the same process was then expected to be as equally effective at fabricating a battery material system. The primary difference between the two device systems for the purposes liquid cell electrochemistry experimentation is that the battery electrode system requires two separate electrodes of different material to be deposited. If it is desired to observe the entirety of the system, both electrodes must be deposited onto the SiN_x window, although this is not always a requirement and some tests will suffice with the material being in contact with both the metallic electrode and the liquid electrolyte.

From an experimental and technical standpoint, very little differs in the deposition of a two-electrode system from a single electrode system. Different materials are used, and if both electrodes have to be deposited onto the window an added level of care is required to ensure no material overlap or, in the worst-case scenario, shorting

occurs. One primary difference between this process and the one described in the previous section is the amount of material deposited. For battery materials a sufficient mass of Li^+ ion material is required for the system to operate. In most cases, this material is not of interest to us (as these tests primarily will focus on the physical changes observed in anode materials), however it still must be present. This large mass of material is usually electron opaque and can present window stability problems. Another concern is the introduction of a pressure gradient across the window. With more material at one end of the flow path than the other, there is potential for a small pressure gradient to occur within the flowing liquid. While the cells are designed to handle very high pressures, due to the nature of the TEM, they are designed under the assumption that the pressure at the liquid-window-column interface is even. If there is a large mass of material inhibiting flow at one extremity of the window, unwanted stresses can be introduced. These phenomena are difficult to experimentally quantify, as there is no easily discernible way to tell how the window breaks after the fact.

The primary system printed in the two electrode configuration was a battery system consisting of a $LiFePO_4$ cathode, with either a carbon or Si nanoparticle anode. The initial tests were conducted with $LiFePO_4$ and carbon in order to determine the required amount of $LiFePO_4$ for the cell to function and to ensure cells did indeed function in battery configuration. Activated carbon was dispersed in IPA, $LiFePO_4$ was dispersed and sonicated as described in the Liquid Phase exfoliation section of Chapter 2. Both dispersions were dispersed at a concentration of 10 mg ml^{-1} and were then printed sequentially. The $LiFePO_4$ electrode was printed first, to a thickness of 50 printed layers. The carbon was deposited to a thickness of 100 printed layers. Both electrodes are seen in BF and DF optical images (x5 magnification) in Figure 3.13.

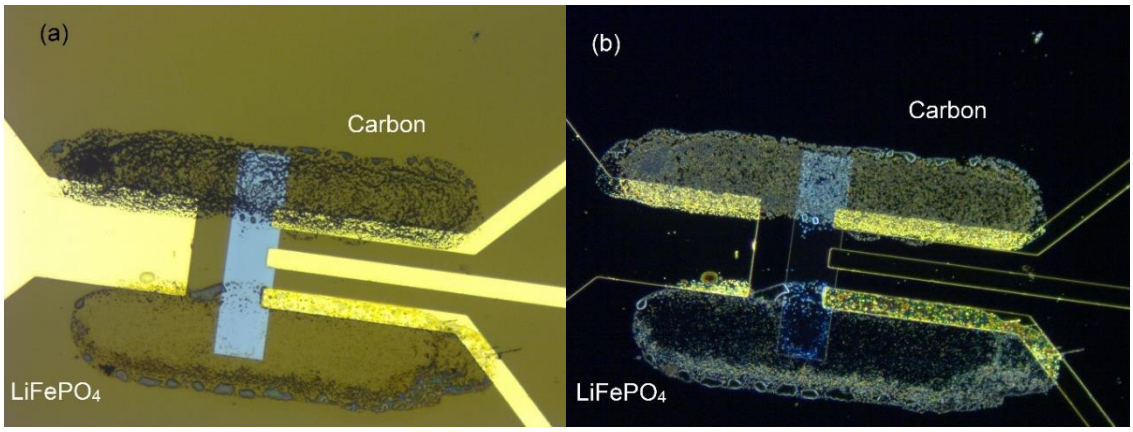

Figure 3.13: Optical microscopy images of a two-electrode battery cell formed from carbon and LiFePO4 printed patterns. (a) shows a bright field image of the deposited material. The mass of carbon is clearly visible. (b) shows a dark field image of the deposited material. Most of the contact line of the LiFePO4 has accumulated along the Au electrode. The contact line breaks up as it extends over the window however a concentration of material can be seen at the leading edge of the Au electrode jutting into the window.

The DF images provide a good insight into how each of the dispersions have deposited onto the cell. The 100 layers of carbon has deposited in a reasonably concentrated mass, forming a more uniform film than is usually seen. The carbon disperses well in the solvent and so the deposited concentration is conceivably very close to the beginning concentration of the dispersion.

The printed $LiFePO_4$ presents an unusual printed contact line. There is a clear difference in wetting and contact line pinning between the Au electrode and the SiN_x, with both the DF and BF images above showing that the deposited contact line breaks down when subjected to large surface energy changes. In addition, there is a height difference of 100 nm (provided by Hummingbird Scientific[45]) between the Au electrode and the surrounding SiN_x surface. This also serves to disrupt the continuity of the contact line. Despite this irregular deposition, from the DF image in Figure 3.13 there is a clear accumulation of material at the electrode edge for imaging, and along the length of the surface of the Au electrode, which will contribute to the overall signal obtained when cycled. The actual morphological and chemical mechanisms by which $LiFePO_4$ and carbon store energy are reasonably well known. This material combination was used in order to obtain *ex-situ* electrochemical responses which could be compared to the literature values of $LiFePO_4$ charge-discharge behaviour.

For most of the recent history of the Li ion battery simple graphite has been the anode of choice. However graphite anodes have a tendency to be fragile and while their energy density is high, other materials have displayed faster rates and better performance at elevated or lowered temperatures, and so new anode materials are needed if Li ion battery systems are to continue to improve. Commonly researched anode materials include TiO_2,[46], $Li_4Ti_5O_{12}$,[47,48] CNTs and CNT based composites,[49,50] Si nanoparticles[51–53] and Si nanowires[54,55], among others.

Silicon exhibits a very large volume increase as it alloys during lithiation.[56,57] This volume expansion can eventually lead to fracture of the particles or wires, which severely limits the practical number of cycles the cells can sustain. Understanding the mechanisms of this lithiation-induced strain and eventual fracturing is key to effectively utilising Si as an anode material, and it is for these reasons that it is perfect for analysis in an *in-situ* TEM electrochemistry experiment. The materials undergo both physical and chemical changes that can be observed within an in-situ TEM environment. The aim of this section of the experiment was to examine the swelling of Si nanoparticles and investigate how the addition of other materials such as CNTs, carbon black and graphene would inhibit the swelling and fracture.

Initially the electrodes were formed from Si nanoparticles dispersed in IPA. The dispersion was not subjected to any extra treatment such as sonication and no binders or stabilisers were added. The Si-IPA dispersion remained stable over the course of a week, beginning to fully collapse past this point. Original dispersions were at a concentration of 1 mg ml^{-1}. The counter electrode was to be formed by $LiFePO_4$, which was printed in the same manner as shown in Figure 3.13, which additional passes required. Chemical and morphological tests were not initially required for the $LiFePO_4$ so it was satisfactory to print this material off window, but still within the liquid flow channel and connected to the electrode. While this approach removes the material from the viewing area, it offers two distinct improvements from a technical standpoint. Firstly, it removes the need to print a large mass of material directly under the SiN_x window. As stated previously, large amounts of material within the viewing area greatly deteriorate window stability. Secondly, it allows for a greater amount of material to come into contact with the electrode itself. The architecture of the electrode close to the window gives a very small area on which material can be deposited. Off the window there is far more scope to deposit material directly onto the Au electrode, and accuracy problems

which are frequently seen in this work when printing any number of consecutive layers above 10 layers are diminished. This also eliminates the possibility of cross electrode contamination or electrical shorting of the electrode system as a whole.

Initial printing tests used 10 printed passes of Si and 200 printed passes of $LiFePO_4$. After repeated window breakages, the decision was made to stagger the positions of the deposited contact lines rather than deposit all passes directly on top of one another. A small number of passes (2 passes for Si and 10 for $LiFePO_4$) would be deposited, and then the deposition target would be moved slightly This was done in the hope that a continuous network of material would still be deposited, but not at a height that would jeopardise the integrity of the SiN_x window. Once again, the effects of changes like this are difficult to quantify, lacking any kind of proper way to analyse the broken windows as we are, however window breakages were seen to decrease once this approach was taken.

A selection of both passivated and non-passivated cells were available during the course of this part of the experimentation. Hummingbird Scientific offer passivated electrodes as a method to reduce the noise that may be introduced in electrochemical testing from the interaction of the metallic electrodes and the surrounding electrolyte. These passivated cells offer both advantages and disadvantages. In essence, the sole difference between these cells and the regular cells is that the metallic electrode materials are coated with a (non-specified) insulating coating along the length of the electrode leaving only the pads at the rear of the cell and the parts of the electrodes that extend into the window uncovered. While this is intended to produce a clearer signal, one of the disadvantages that it presents is that material must be deposited into the window area in order to for the cell to function. In this case where it is desirable to limit the overall height of material that is being placed within the window to avoid rupturing the cells, this is not a desired outcome. In addition, the passivation layer increases the total cell thickness, as the spacer chips rest on top of the passivated metallic electrodes. This will serve to increase the thickness of the total liquid layer, further limiting the achievable resolution of the cell when it is in the TEM.

3.6 Conclusion

In this chapter the process for depositing micro-electrochemical electrodes on prefabricated TEM cells is presented. The effect of voltage, print head height,

droplet spacing and substrate temperature on the final line morphology was investigated, and a set of parameters to be used for the effective deposition of materials dispersed in IPA as electrodes was decided upon. The coffee staining effect that is visible in almost all drying liquid systems was used, rather than suppressed, as a method of depositing material in a manner that was eventually more accurate than using the full width of the printed lines, exceeding to some degree the stated accuracy range of the printer manufacturer (± 25 μm). Following on from these initial characterisation experiments, a range of IPA based nanomaterial inks were prepared, and both battery and pseudocapacitive materials were deposited. This method demonstrated its versatility when compared to traditional methods of TEM electrode fabrication in its ability to consistently deposit composite inks rather than those composed of a single material. This process mitigates one of the major issues for the development of in-situ TEM analysis for energy storage systems. The vast majority of published works in the field exclusively cover Si nanowires and their lithiation dynamics and kinetics.[11,15,58,59] While this is not to say that this avenue of research is not important, it is clear that the field has been material limited by what can be effectively placed using FIB techniques. The methodology developed was accurate enough to deposit two distinct working and counter electrodes that are required for the analysis of asymmetric or battery materials. Depending on the desired analysis within the TEM system one or both electrodes can be located on the electron transparent window for future chemical and morphological analysis.

Bibliography

1. Jonge, N. d., Peckys, D. B., Kremers, G. J. & Piston, D. W. Electron microscopy of whole cells in liquid with nanometer resolution. *Proc. Natl. Acad. Sci.* **106,** 2159–2164 (2009).

2. Woehl, T. J. *et al.* Correlative electron and fluorescence microscopy of magnetotactic bacteria in liquid: Toward in vivo imaging. *Sci. Rep.* **4,** 6854 (2014).

3. Sacci, R. L. *et al.* Direct visualization of initial SEI morphology and growth kinetics during lithium deposition by in situ electrochemical transmission electron microscopy. *Chem. Commun.* **50,** 2104–2107 (2014).

4. Dollé, M., Grugeon, S., Beaudoin, B., Dupont, L. & Tarascon, J. M. In situ TEM study of the interface carbon/electrolyte. *J. Power Sources* **97–98,** 104–106 (2001).

5. Klein, K. L., Anderson, I. M. & De Jonge, N. Transmission electron microscopy with a liquid flow cell. *J. Microsc.* **242,** 117–123 (2011).

6. Huang, J. Y. *et al.* In situ observation of the electrochemical lithiation of a single SnO2nanowire electrode. *Science (80-.).* **330,** 1515–1520 (2010).

7. Yuk, J. M., Seo, H. K., Choi, J. W. & Lee, J. Y. Anisotropic lithiation onset in silicon nanoparticle anode revealed by in situ graphene liquid cell electron microscopy. *ACS Nano* **8,** 7478–7485 (2014).

8. Liu, X. H. & Huang, J. Y. In situ TEM electrochemistry of anode materials in lithium ion batteries. *Energy Environ. Sci.* **4,** 3844–3860 (2011).

9. Wang, C. M. In situ transmission electron microscopy and spectroscopy studies of rechargeable batteries under dynamic operating conditions: A retrospective and perspective view. *J. Mater. Res.* **30,** 326–339 (2015).

10. McDowell, M. T. *et al.* In situ TEM of two-phase lithiation of amorphous silicon nanospheres. *Nano Lett.* **13,** 758–764 (2013).

11. Liu, X. H. *et al.* Anisotropic swelling and fracture of silicon nanowires during lithiation. *Nano Lett.* **11,** 3312–3318 (2011).

12. Liu, X. H. *et al.* Size-dependent fracture of silicon nanoparticles during lithiation. *ACS Nano* **6,** 1522–1531 (2012).

13. Williamson, M. J., Tromp, R. M., Vereecken, P. M., Hull, R. & Ross, F. M. Dynamic microscopy of nanoscale cluster growth at the solid-liquid interface. *Nat. Mater.* **2,** 532–536 (2003).

14. Chen, X., Noh, K. W., Wen, J. G. & Dillon, S. J. In situ electrochemical wet cell transmission electron microscopy characterization of solid-liquid interactions between Ni and aqueous NiCl2. *Acta Mater.* **60,** 192–198 (2012).

15. Gu, M. *et al.* Demonstration of an electrochemical liquid cell for operando transmission electron microscopy observation of the lithiation/delithiation behavior of Si nanowire battery anodes. *Nano Lett.* **13,** 6106–6112 (2013).

16. Peng, L. *et al.* Ultrathin two-dimensional MnO2/graphene hybrid nanostructures for high-performance, flexible planar supercapacitors. *Nano Lett.* **13,** 2151–2157 (2013).

17. Xu, Z. L. *et al.* Carbon-coated mesoporous silicon microsphere anodes with greatly reduced volume expansion. *J. Mater. Chem. A* **4,** 6098–6106 (2016).

18. Wu, H. *et al.* Engineering empty space between Si nanoparticles for lithium-ion battery anodes. *Nano Lett.* **12,** 904–909 (2012).

19. Gohier, A. *et al.* High-rate capability silicon decorated vertically aligned carbon nanotubes for li-ion batteries. *Adv. Mater.* **24,** 2592–2597 (2012).

20. Higgins, T. M. *et al.* A Commercial Conducting Polymer as Both Binder and Conductive Additive for Silicon Nanoparticle-Based Lithium-Ion Battery Negative Electrodes. *ACS Nano* **10,** 3702–3713 (2016).

21. Xue, L. *et al.* Carbon-Coated Si Nanoparticles Dispersed in Carbon Nanotube Networks As Anode Material for Lithium-Ion Batteries. *ACS Appl. Mater. Interfaces* **5,** 21–25 (2013).

22. Park, S. H. *et al.* Self-assembly of Si entrapped graphene architecture for high-performance Li-ion batteries. *Electrochem. commun.* **34,** 117–120 (2013).

23. Lotya, M. *et al.* Liquid phase production of graphene by exfoliation of graphite in surfactant/water solutions. *J. Am. Chem. Soc.* **131,** 3611–3620 (2009).

24. Coelho, J. *et al.* Manganese oxide nanosheets and a 2D hybrid of graphene-manganese oxide nanosheets synthesized by liquid-phase exfoliation. *2D Mater.* **2,** 025005 (2015).

25. Mendoza-Sánchez, B., Coelho, J., Pokle, A. & Nicolosi, V. A 2D graphene-manganese oxide nanosheet hybrid synthesized by a single step liquid-phase co-exfoliation method for supercapacitor applications. *Electrochim. Acta* **174,** 696–705 (2015).

26. Coleman, J. N. Liquid-phase exfoliation of nanotubes and graphene. *Adv. Funct. Mater.* **19,** 3680–3695 (2009).

27. Ciesielski, A. & Samorì, P. Graphene via sonication assisted liquid-phase exfoliation. *Chem. Soc. Rev.* **43,** 381–398 (2014).

28. Hernandez, Y. *et al.* High-yield production of graphene by liquid-phase exfoliation of graphite. *Nat. Nanotechnol.* **3,** 563–568 (2008).

29. Coleman, J. N. *et al.* Two-dimensional nanosheets produced by liquid exfoliation of layered materials. *Science (80-.).* **331,** 568–571 (2011).

30. Diaz, M. E., Savage, M. D. & Cerro, R. L. The effect of temperature on contact angles and wetting transitions for n-alkanes on PTFE. *J. Colloid Interface Sci.* **503,** 159–167 (2017).

31. Petke, F. D. & Ray, B. R. Temperature dependence of contact angles of liquids on polymeric solids. *J. Colloid Interface Sci.* **31,** 216–227 (1969).

32. Lee, A., Sudau, K., Ahn, K. H., Lee, S. J. & Willenbacher, N. Optimization of experimental parameters to suppress nozzle clogging in inkjet printing. *Ind. Eng. Chem. Res.* **51,** 13195–13204 (2012).

33. Soltman, D. & Subramanian, V. Inkjet-printed line morphologies and temperature control of the coffee ring effect. *Langmuir* **24,** 2224–2231

(2008).

34. Rioboo, R., Tropea, C. & Marengo, M. Outcomes From a Drop Impact on Solid Surfaces. *At. Sprays* **11,** 12 (2001).

35. Yarin, A. L. DROP IMPACT DYNAMICS: Splashing, Spreading, Receding, Bouncing…. *Annu. Rev. Fluid Mech.* **38,** 159–192 (2006).

36. Clanet, C., Béguin, C., Richard, D. & Quéré, D. Maximal deformation of an impacting drop. *J. Fluid Mech.* **517,** 199–208 (2004).

37. RHEE, S. K. Wetting of TaC by Liquid Cu and Liquid Ag. *J. Am. Ceram. Soc.* **55,** 157–159 (1972).

38. RHEE, S. K. Wetting of Ceramics by Liquid Metals. *J. Am. Ceram. Soc.* **54,** 332–334 (1971).

39. Shafrin, E. G. & Zisman, W. A. Effect of temperature on wetting of high- and low-energy solid surfaces. *J. Phys. Chem.* **76,** 3259–3267 (1972).

40. Van Osch, T. H. J., Perelaer, J., De Laat, A. W. M. & Schubert, U. S. Inkjet printing of narrow conductive tracks on untreated polymeric substrates. *Adv. Mater.* **20,** 343–345 (2008).

41. Seo, C., Jang, D., Chae, J. & Shin, S. Altering the coffee-ring effect by adding a surfactant-like viscous polymer solution. *Sci. Rep.* **7,** 500 (2017).

42. Hu, H. & Larson, R. G. Evaporation of a sessile droplet on a substrate. *J. Phys. Chem. B* **106,** 1334–1344 (2002).

43. Ring, E. A. & De Jonge, N. Microfluidic system for transmission electron microscopy. *Microsc. Microanal.* **16,** 622–629 (2010).

44. Woehl, T. J. *et al.* Experimental procedures to mitigate electron beam induced artifacts during in situ fluid imaging of nanomaterials. *Ultramicroscopy* **127,** 53–63 (2013).

45. Biasing Chips | Hummingbird Scientific. at <http://hummingbirdscientific.com/biasing-chips/>

46. Tang, Y. *et al.* Mechanical force-driven growth of elongated bending Tio2-based nanotubular materials for ultrafast rechargeable lithium ion batteries. *Adv. Mater.* **26,** 6111–6118 (2014).

47. Wang, Y. Q. *et al.* Rutile-TiO2nanocoating for a high-rate Li4Ti5O12anode of a lithium-ion battery. *J. Am. Chem. Soc.* **134,** 7874–7879 (2012).

48. Zaghib, K., Simoneau, M., Armand, M. & Gauthier, M. Electrochemical study of Li4Ti5O12as negative electrode for Li-ion polymer rechargeable batteries. *J. Power Sources* **81–82,** 300–305 (1999).

49. De Las Casas, C. & Li, W. A review of application of carbon nanotubes for lithium ion battery anode material. *J. Power Sources* **208,** 74–85 (2012).

50. Wang, W. *et al.* Silicon decorated cone shaped carbon nanotube clusters for lithium ion battery anodes. *Small* **10,** 3389–3396 (2014).

51. Lin, Y. M. *et al.* High performance silicon nanoparticle anode in fluoroethylene carbonate-based electrolyte for Li-ion batteries. *Chem.*

Commun. **48,** 7268–7270 (2012).

52. Liang, B., Liu, Y. & Xu, Y. Silicon-based materials as high capacity anodes for next generation lithium ion batteries. *J. Power Sources* **267,** 469–490 (2014).

53. Wu, H. & Cui, Y. Designing nanostructured Si anodes for high energy lithium ion batteries. *Nano Today* **7,** 414–429 (2012).

54. Chan, C. K. *et al.* High-performance lithium battery anodes using silicon nanowires. *Nat. Nanotechnol.* **3,** 31–35 (2008).

55. Yin, Y. X., Wan, L. J. & Guo, Y. G. Silicon-based nanomaterials for lithium-ion batteries. *Chinese Sci. Bull.* **57,** 4104–4110 (2012).

56. Oumellal, Y. *et al.* The failure mechanism of nano-sized Si-based negative electrodes for lithium ion batteries. *J. Mater. Chem.* **21,** 6201–6208 (2011).

57. Hertzberg, B., Alexeev, A. & Yushin, G. Deformations in Si-Li anodes upon electrochemical alloying in nano-confined space. *J. Am. Chem. Soc.* **132,** 8548–8549 (2010).

58. Lu, X., Bogart, T. D., Gu, M., Wang, C. & Korgel, B. A. In Situ TEM Observations of Sn-Containing Silicon Nanowires Undergoing Reversible Pore Formation Due to Fast Lithiation/Delithiation Kinetics. *J. Phys. Chem. C* **119,** 21889–21895 (2015).

59. Wang, C.-M. *et al.* In Situ Transmission Electron Microscopy Observation of Microstructure and Phase Evolution in a SnO_2 Nanowire during Lithium Intercalation. *Nano Lett.* **11,** 1874–1880 (2011).

Chapter 4: In-situ electrochemistry and imaging of printed cells

4.1 In-situ and ex-situ electrochemical testing

Fundamentally the *in-situ* testing of materials and systems during electron microscopy is a means to provide more meaningful insight into how these materials and systems behave under certain stimuli. These stimuli can be very simple, such as simply observing how biological samples behave in a liquid environment,[1–3] or can be more complicated, like observing the lithiation dynamics of nanowires as they are electrochemically cycled.[4–7] Regardless of the complexity of the process, the aim remains the same; to provide a more complete understanding how materials at the nanoscale behave in an environment that is much closer to reality than those experienced by materials deposited onto copper TEM grids for standard imaging. The previous chapter discussed the fabrication techniques developed for this work, and how these new fabrication techniques have helped overcome some of the traditional material limitations that can be seen in the field of in-situ materials testing of energy storage materials.

As mentioned in Chapter 3, liquid cell TEM electrochemistry represents the most accurate reproduction of the internal structure of energy storage cells available to us. Electron microscopy techniques and microscopes have become sufficiently advanced that under controlled conditions, accurate morphological and chemical information about materials can be observed through thin liquid layers, up to 1 µm in thickness. In liquid S/TEM experiments, nanometre resolution has been reported even for thicker specimen samples.[1,8,9] The imaging and electrochemical analysis of these structures are not trivial however and require an amount of process development on a similar level that the fabrication steps require. The ideal testing scenario is one in which a material can be cycled within the liquid electrochemistry holder and the electrodes be examined with both imaging and spectroscopic techniques. This full analysis would allow a direct correlation of what is seen in the developing CV curves with the acquired images and chemical spectra.

Unfortunately, due to a range of limitations it is often not possible for all these conditions to be satisfied. Ex-situ testing (electrochemical testing of a printed cell, but at ambient conditions outside the microscope) is firstly required to verify if the cell is functioning as desired. A cell may not function for a variety of reasons; there may not be enough material deposited on the electrodes, the material may not be conductive enough to generate a signal, or the residual signal created by the cell itself, i.e the double layer formed by the bare Au or Pt electrodes and the electrolyte may be obscuring the signal from the material. Even if there is little or no electrochemical response observed from a cell, it is still possible for that cell to be functioning. Due to the nature of this kind of electrochemical testing, very low masses of materials are used, and noise can prove to be a significant problem. As such poor CV responses are at times unavoidable, particularly for materials with low conductivity.

Beam-induced effects must also be considered when observing materials, and particularly in relation to changes observed within the electrolyte. Before the development of commercial *in-situ* holders, beam induced changes were one of the first kinds of in-situ TEM studies conducted.[10–14] The accelerating voltage of the electron beam imparts more than enough energy to induce significant changes in materials if care is not taken to lower the electron dose. It is vital that changes being observed are in fact being created by the electrochemical cycling and not the incident electron beam. Electrolyte selection is a part of this process. Some organic electrolytes, while usually used without issue in standard coin cells, when utilised in electrochemical testing are beam sensitive and will degrade under high intensity electron beams. This degradation can result in crystallisation of the electrolyte under the beam, or a complete disassociation of the liquid electrolyte causing the formation of gas bubbles within the cell. These gas bubbles then push away surrounding electrolyte, drying the cell and inhibiting replenishment of the electrolyte from the flow channel.

Ex-situ testing is also required due to the potential impact of this kind of experimentation on the microscopes used. Ideally every cell fabricated would yield a clear electrochemical response and could immediately be observed within the TEM column. In reality, even in situations where a distinct electrochemical response is observed, potential experimentation is limited by window stability. Liquid cell experiments are technically demanding and the failure of one or both liquid cell

windows inside the TEM will introduce liquid inside the TEM column. Depending on the liquid used, considerable damage or contamination can be caused to the column and the electron gun if exposed to liquid, it is therefore imperative that only the highest quality samples are used in the final in-situ testing.

4.2 The in-situ holder

Apart from the TEM itself, the most important piece of apparatus used in this work is the in-situ holder itself. The holder used in this work is a Liquid ElectroChemistry TEM holder (Hummingbird Scientific, Lacey, WA). This holder provides for a closed liquid environment in which electrochemical tests can be conducted. A brief description of the Si chips that form the cells was given in Chapter 3 previously. These cells sandwich together forming the closed cell, with the SU8 spacing layer and the metallic electrode determining the thickness of the liquid channel. These sandwiched electrodes sit into the tip of the holder and are secured in place by a series of O-rings. The O-rings are designed to seal the liquid flow channels from the exterior of the tip and holder. The O-rings and the sandwiched electrodes are held in place by an upper retaining plate and pin, securing the cell in place. An exploded diagram of the tip assembly, and completed tip and holder are given in Figure 4.1. The 3 metallic pins of the electrochemistry chips connect to the tip itself which is connected via a co-axial cable to an external potentiostat. A pair of openings are located to the right and left side of the tip, allowing for a flow of liquids through.

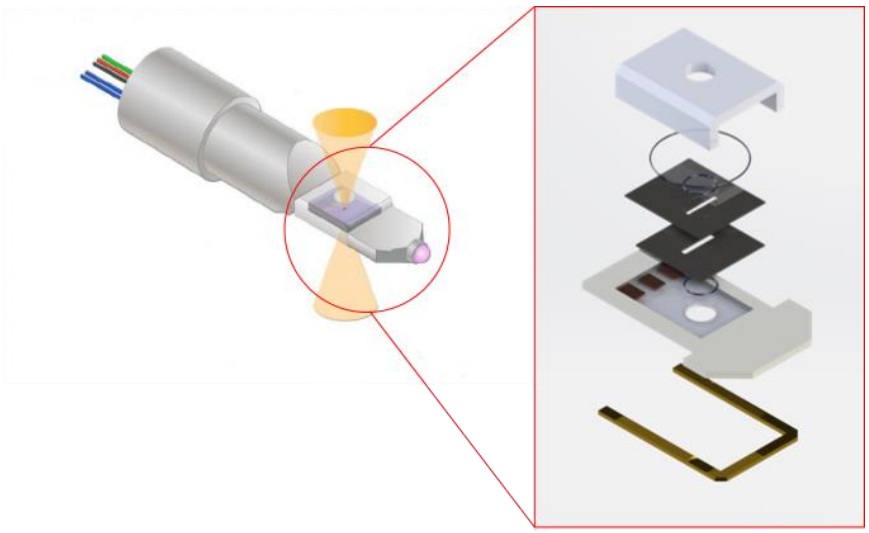

Figure 4.1: Illustration of the liquid cell tip with exploded view of internal tip assembly. Seen from top to bottom of exploded view, retaining plate, top O-rings, Electrochemistry chip, spacer chip, bottom O-rings, electrochemical tip, slide pin. Zoomed out view of tip adapted from Ref (7)

These openings connect to flow paths to the rear of the tip allowing for the connection of gas-syringes through which a steady flow of liquid can be pumped.

The tip and a detailed assembly is given in Figure 4.1. The leads at the rear of the tip are the liquid flow tubes and electrochemical connections. These connect to the back of the whole holder assembly. Using this setup, some papers report keeping the reference and/or the counter electrode outside the microscope, rather than inside the cell and tip assembly. This requires the fabrication of the reference and counter electrodes inside the liquid flow paths, or inside the gas syringe holding the electrolyte.

4.3 Cell assembly and initial liquid flow

The cell itself is assembled in such a manner as to minimise the chance of weakening or shattering the SiN_x windows. The electrochemistry chip and spacer chip are plasma cleaned using an O/Ar gas mixture to encourage wetting of the liquid electrolyte. The cell is then assembled dry; that is the electrolyte is not drop cast during the assembly of the sandwiched electrodes. Once the o-rings and the retaining plate are in place, the liquid electrolyte is then slowly flowed (1 µL per minute) through the liquid flow channel. Some publications suggest a wet assembly,[15,16] i.e depositing liquid before the sandwiching of the two electrodes. For work with non-reactive solvents, this may be acceptable, but with electrolytes used in this work ($LiPF_6$ in EC:DMC for example) limited exposure to air and water is desirable. As such the electrolyte is instead flowed directly into the fully assembled tip. Exposure to air and water is less of a concern when handling the aqueous electrolytes that are used in the sections for supercapacitor materials, however as good practice all electrolytes are handled in as careful a manner as possible.

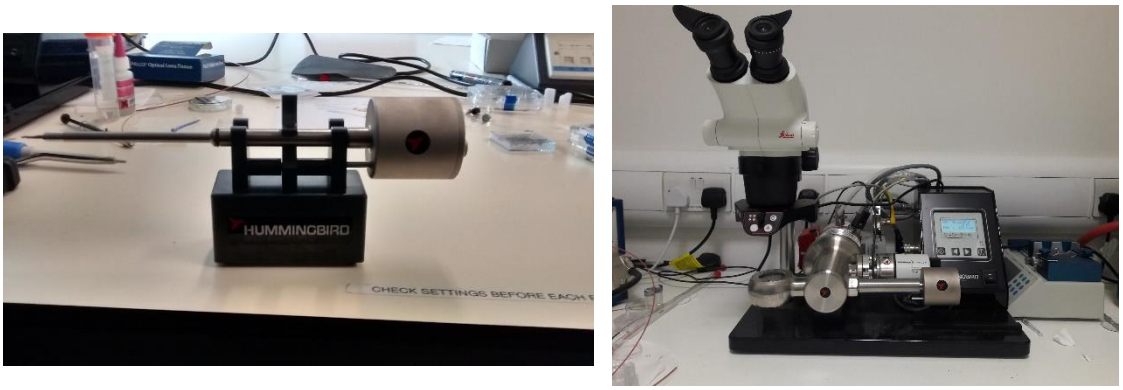

Figure 4.2: The liquid cell holder and the pumping station. Cells are assembled, and the integrity of the assembled cell is verified using the high vacuum chamber in the pumping station.

Work by Fahrenkrug *et al* (in collaboration with Hummingbird Scientific)[17] suggests that wetting of the entirety of the electrode by the electrolyte can introduce higher currents through double layer storage between the larger electrode area and the electrolyte, potentially masking the CV features that the user wishes to view. In addition, unexpected chemical reactions from contact between the electrolyte and the holder/wires/contacts can also be introduced when the entirety of the cell is wetted. Another consideration is the difficulty in correctly aligning the SiN_x windows. Before the O-rings and retaining plate are added, cells do not necessarily sit flush with one another. While for standard liquid imaging it is only necessary for there to be a small amount of overlap between the windows in order to observe the interior of the cell, the electrochemistry cell is different. If the cells are too skewed from one another, the metallic electrodes are no longer visible within the viewing window. This can occur as the top cell slides in contact with the liquid electrolyte.

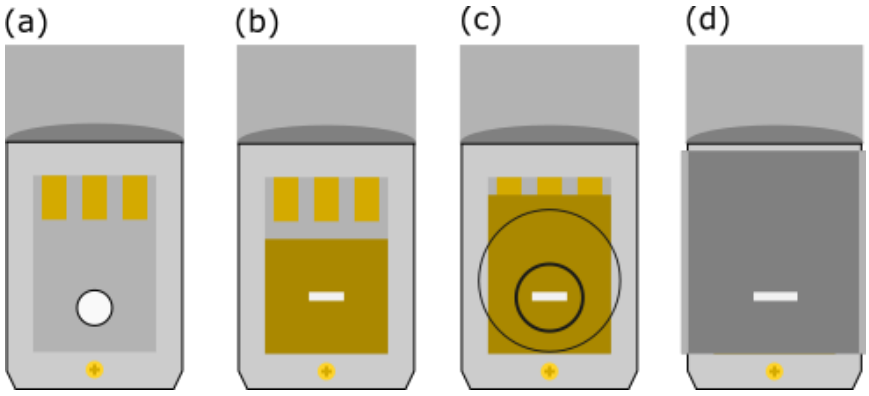

Figure 4.3:Liquid cell tip assembly showing (a) insertion of o-ring, (b) insertion of spacer chip, (c) insertion of cell with printed material, with pair of retaining o-rings and (d) the tip is secured with a retaining plate.

Once the cell is fully assembled and liquid electrolyte is flowing, the integrity of the cell is examined using a desktop pumping station. This pumping station subjects the holder to low pressures, mimicking the conditions found within the TEM column (for a well assembled, non-leaking cell the pumping station should reach 10^{-6} mbar). The pumping station is equipped with an optical microscope for analysing the windows and the tip. While the station lacks advanced imaging hardware, a reasonable amount of information as to the stability of the window itself can be obtained from observing the diffraction patterns on the window reflecting the light in the microscope. These changing patterns usually provide a good indication of the stresses the window is experiencing and the presence of unusual or non-symmetric patterns can act as a reasonable predictor of a window that is likely to rupture once the pumping station is brought to a high vacuum.

4.4 Ex-Situ electrochemical testing of MnO_2-graphene hybrid supercapacitor materials with aqueous electrolytes

The first set of materials to be tested were MnO_2-Graphene composites designed for use as supercapacitor electrodes. The graphene was added to increase the conductivity of the material. As mentioned in Chapter 1, while MnO_2 is an impressive pseudocapacitor (with a specific capacitance between 700 and1300 F g^{-1}). [18,19] it is often limited by its low conductivity when electrodes are on the micrometre scale (capacitance dropping to 250 F g^{-1}). According to the theory of how these electrodes cycle and store energy, there should not be any direct physical changes in the electrode. As explained in chapters 1 and 2, these electrodes undergo reversible redox reactions to store energy, and so it would be expected that only chemical changes should be observed. While the life cycles of pseudocapacitive materials are long (up to 15,000 cycles with a 4.6% drop from initial total capacitance)[20], if they are to be used in applications where there is expected to be a very high number of cycles, such as braking energy recovery in HEVs or PIEVs, the deviation from their theoretically unlimited number of charge and discharge cycles must be understood. There is potential for non-reversible reactions to occur that will result in physical changes or degradation to occur within the material.

These cells were all printed in the manner described in the single electrode printing section of chapter 3, initially at 5 printed passes at 5 mg ml^{-1} concentration. No counter electrode was used in these tests. Initial tests were performed ex-situ to verify the functionality of the printed cells. These tests were conducted at a scan rate of 100 mV s^{-1} utilising a pair of aqueous electrolytes, 0.1 M K_2SO_4 and LiCl. The cycling tests were kept below the upper voltage limit that aqueous electrolytes are capable of sustaining (≈1.3 V). In order to establish a baseline signal, a blank cell containing K_2SO_4 electrolyte was cycled at the same scan rate (100 mV s^{-1}) used for other tests. The blank cell was tested between a range of voltages, providing the CV curves shown in Figure 4.4. All electrochemistry tests in this chapter were performed with a Gamry Reference 300 potentiostat.

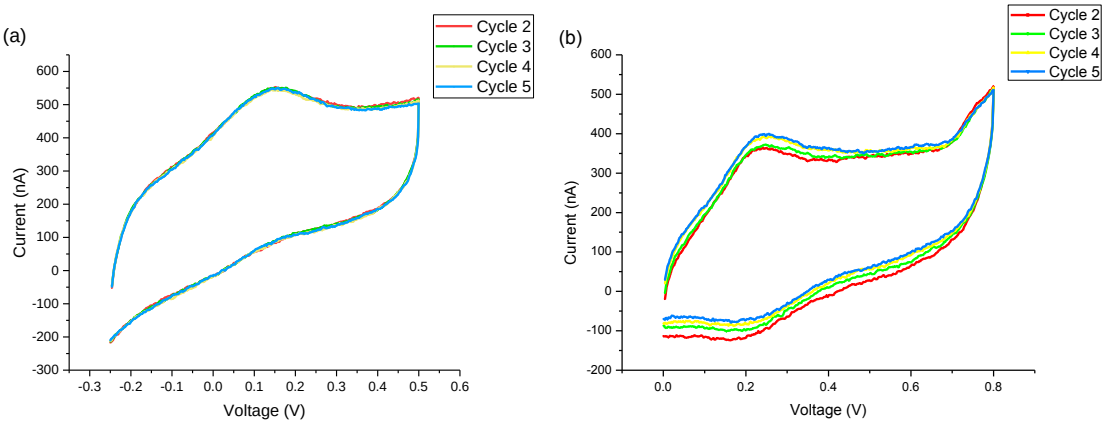

Figure 4.4: Blank cell containing K2SO4 cycled between (a) -0.25 V and 0.5V and (b) between 0 V and 0.8 V.

As seen in the CV curves for the blank cells, the cells have an inherent capacitance due to the presence of a double layer at the interface of the electrolyte and the Au electrode. The first cycle of both tests contains highly noisy signals as the cell stabilises and was excluded from both of the above graphs for this reason. The presence of small amounts of double layer capacitance is to be expected. Fahrenkrug *et al*[17] noted that the exposure of the metallic electrodes to the electrolyte will generate currents within the cell that may be large enough to obscure low signals. While these currents, and the total charge stored within the cells (3.59 µC for CV curve (a) and 2.562 µC for curve (b)) are small, the expected material response will also be small due to the tiny amount of material deposited on a 5 printed pass cell (1.75 ng for a 5 pass electrode with 5 mg ml^{-1} inks). The expected current for this cell

was calculated to be 239 nA assuming the theoretical capacitance of the material (1370 F g^{-1}) achieved, along with 100% mass utilisation. In the real situation presented here both capacitance and mass utilisation would be expected to be far lower, and accordingly the expected current would be far lower than this 239 nA figure.

In addition to this, due to the large proportion of the graph that is displayed above the 0 A point of the y axis, it is quite possible that the electrochemical response is indicative of either gas evolution or electrolyte breakdown within the cell itself in addition to latent capacitive effects resulting from a formation of a double layer between the Au contacts and the aqueous electrolyte.

Once blank cell CV curves were taken, the same parameters were used to cycle cells with the 5 printed layers of MnO_2-Graphene hybrid. These cycles, shown in Figure 4.4 yielded similar CV curves as the blank cells. These similar CV curves present two possibilities; the first is that the cell is functioning, and the material is charging and discharging, but at low enough currents for the potentiostat to be unable to identify the signal over the base current of the Au-Electrolyte double layer. The second, (and worse) possibility is that the cell is not functioning at all, and that the material is not charging and discharging and the potentiostat is successfully picking up all signals from inside the closed liquid cell. The tests were performed with differing voltage ranges, both for blank and material loaded cells with the aim of identifying regions where there was a possibility of the material signal overcoming the base signal of the cell. None of these tests provided a CV curve in which the material signal was observable above the base signal provided by the empty cell. On inspection of the cells after cycling, liquid remains within the channel, ruling out the possibility that the cells had become dry, or that there was flow problems with the liquid electrolyte. The constant flow of electrolyte from the auto gas syringe mitigates any evaporation or degradation of the electrolyte.

Extended voltages ranges, extending up to 0.9 V were also tested, but again yielded no noticeable changes. The small peak (or hump) seen in Figure 4.4 (a) and in both curves in Figure 4.5 occurs at a higher current in the cells with material than without, however the total amount of energy stored in these cells remains broadly the same. With integration showing 3.563 µC stored in the -0.25 to 0.5 V test and 4.473 µC stored in the -0.3 to 0.6 range, despite the slightly higher operating current for both curves compared to the cells without material. The tests were repeated with

a different aqueous electrolyte (0.1M LiCl) which yielded similar CV responses to those provided by the K_2SO_4 electrolyte.

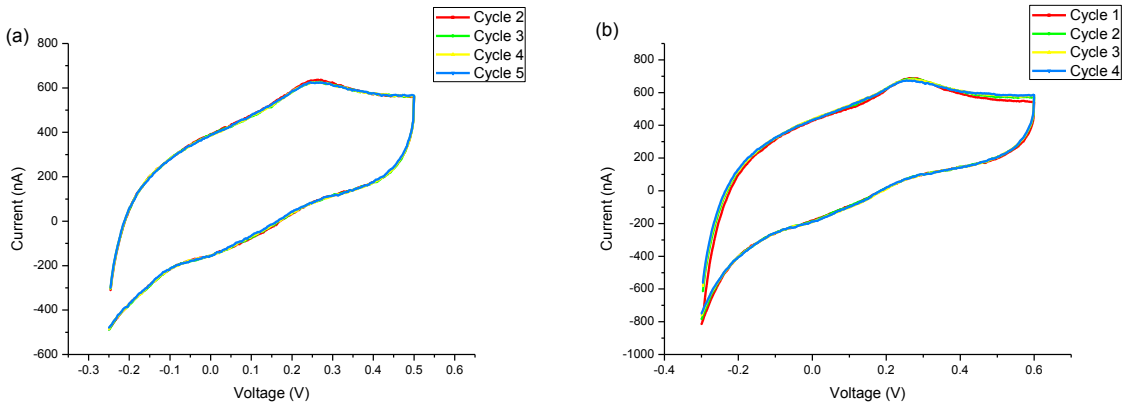

Figure 4.5: CV curves for 5 layers of MnO2-Graphene deposited onto the Au electrodes and cycled with (a) showing the same 0.25 V to 0.5 V range and (b) showing an extended -0.3 V to 0.6 V range. No discernible changes are visible

The low current electrochemical response is believed to be as a result of the low mass of active material deposited. The deposited material is set to print in a single line 300 µm long. While liquid spreading will alter the dimensions of this line, the amount of material deposited will not change. As noted before, the amount of material deposited onto the cell is 1.75 ng for a 5mg ml^{-1} ink dispersion. However, this is just the amount of material that is deposited onto the cell, not necessarily what we can consider material to be available to store energy. As not all material is contained on the contact line that has been deposited onto the electrode, and not all of that material is in electrical contact with the electrode itself, the actual amount of material that will be storing energy is much lower than that total mass of 1.75 ng. The amount of material to be deposited was therefore increased so that a larger amount of material would be deposited onto the electrode and so that there would be a much higher chance of a conductive network being formed extending out from the electrode and into the window.

The same inks were used for these tests- however the amount of material was increased to a total of 50 printed passes, providing a thick and more continuous deposited layer (as shown previously in Figure 3.12). This more continuous film will make a larger proportion of the deposited material available for charge storing. When cycled, these cells showed similar responses as before, although the 50-layer

tests perform at a higher current than those without material and display a higher amount of charge stored.

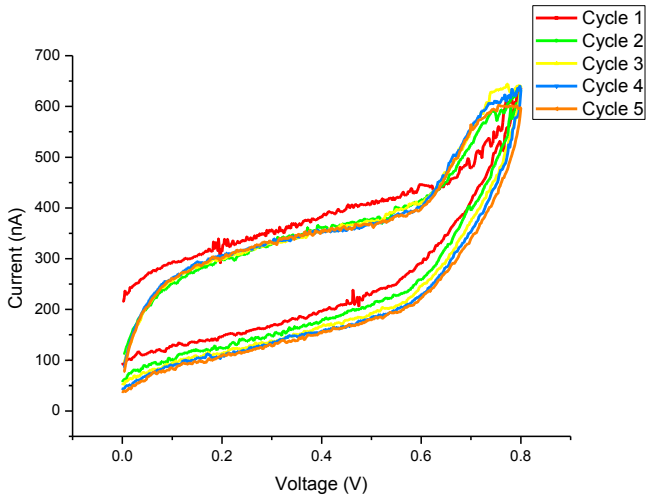

Figure 4.6: A cell consisting of 50 printed passes of MnO2-Graphene hybrid cycled between 0 V and 0.8 V at 100 mV s-1.

The CV curve of the 50-layer cell cycled between 0 and 0.8 V is shown in Figure 4.6. The total amount of charge stored in this cell is larger than the control cell without material, showing 4.684 µC stored. Despite this higher operating voltage and charge stored, the curve itself resembles the blank cell curves. Most promisingly, this test lacks the characteristic hump or peak observed in all cells in locations between 0.1 and 0.3 V. Coupled with the higher operating voltage, this suggests that at least portions of this curve are as a result of material storing energy rather than the cell itself. These ex-situ tests were repeated with a different aqueous electrolyte, LiCl but yielded very similar results. No real signal could be observed above the baseline signal of the cell apart from once again a small response seen between 0.6 and 0.8 V for a 50-layer MnO_2-Graphene hybrid deposition.

As an aside, it is a salient point to make that the bulk of published literature in the field of in-situ electrochemistry do not deal with in-depth, quantitative electrochemistry. For the most part the process has been used as a qualitative means to examine the material. In the rare cases where CV curves are given, they display similarly low current responses, in the tens to hundreds of nano-amp ranges.[6,7,21]In addition to this, Holtz *et al* demonstrated observable differences between platinum microelectrodes cycled in thin and thick liquid layers.[8] Significant Ohmic drops were observed in that experiment, slanting the observed CV curves in

a manner that appears similar to the curve seen in Figure 4.5. Further in-situ, ex-situ, and larger scale device tests would be required to confirm that this is indeed the case, although it is quite likely that similar effects are to be expected. The electrochemical responses observed from these cells are far from ideal, but it is only necessary that they work. This process is not intended to be a fully quantitative electrochemistry analysis of the material, more a qualitative investigation of the response materials show on the micron and nano scale to charging and discharging. It should be considered complimentary to standard tests used for larger scale devices. The processes are cyclical; long term storage and rate capabilities can be observed *ex-situ* and with larger scale devices, and the fundamental causes of the storage effects can be analysed through *in-situ* TEM. This then informs the composition of the next stage of device composition and testing.

4.5 Imaging of cycling MnO_2-Graphene electrodes

From the initial ex-situ testing it is unfortunately unclear from the electrochemical profiles if the cells are functioning as intended. The material mass inside the cell is low, and the material has a lower predicted energy density than materials utilised in the published literature, usually battery type materials and cycled at a much slower rate.[8,22] When the previously mentioned effects of the electrolyte-electrode double layer are taken into account, it becomes very difficult to be able to determine ex-situ which supercapacitor electrodes are suitable for viewing. As such it was decided to insert a 50-layer printed cell into the TEM in order to visualise any changes that may be occurring during the cycling process. The broader 0 to 0.8 V voltage range was selected along with a 100 mV s^{-1} scan rate and a 0.1 M LiCl liquid electrolyte was flowed through the cell.

With the total combined thickness of the cell including both windows, the liquid, the overlapping layers of material and the bowing of the windows increasing the thickness of the liquid layer (as mentioned before the bowing of the windows can increase the liquid path the beam must travel through by up to 100%)[23], resolving individual flakes of the material is not possible. However, the electrode and the deposited material can be seen at reasonable magnification levels. The liquid electrolyte is stable under the beam, although care must be taken as large changes in the focus or defocus value or the beam Z position can create bubbles within the liquid layer. Spot size is kept large and intensity is kept low, spreading the total

beam current over a larger area in order to mitigate any damaging effects of the beam radiation. This will further limit the viewing resolution, and so a compromise between liquid stability and desired resolution must be found in this case. The development of the electrode as the cycling process occurred is shown in Figure 4.7.

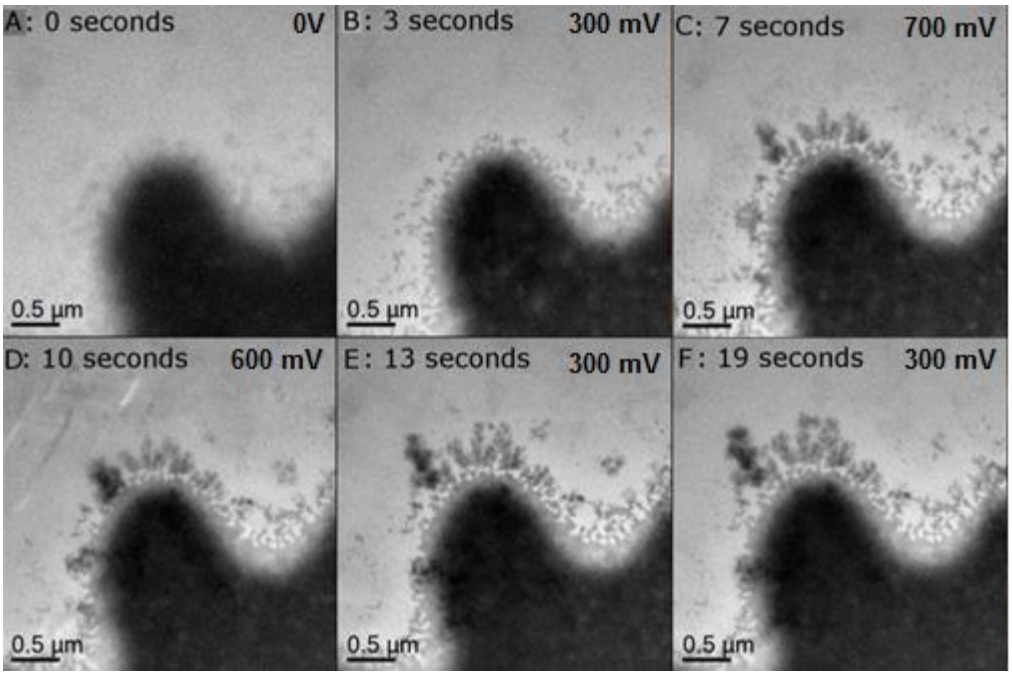

Figure 4.7: Time development of a cycling MnO2-Graphene electrode. Individual flakes are difficult to resolve but the deposited electrode can be seen. The straight edge at the lower right of the images is the Au electrode itself. The test ceased with window rupture.

Figure 4.7 (A) shows the electrode before the cycling begins. The focus of the image changes due to minute differences in the liquid as it flows. Even in non-flowing liquid, high resolution images of individual flakes are difficult to obtain. As the cell begins its charge cycle, dendrite-like formations begin to form outwards from the surface of the material. These continue to grow during the charging cycle of the electrode and is rapid at first, with significant growth occurring between the three and seven second mark (corresponding to 0.3 V to 0.7 V range at 100 mV s^{-1}). This rapid growth slows after the 10 second mark, at which point the electrode would be on the reverse cycle although notably while the dendritic growth stalls it does not stop completely. As the dendrites reach a critical size, they begin to break off from the main electrode and the material either floats out into the liquid or becomes connected to other dendrites. The clusters of material seen to the right-hand side of the main body of the electrode in 4.7 (D) and 4.7 (E) are not beam induced clusters but are material that has detached from the main electrode and drifted off into the liquid. The test finishes in the frame after Figure 4.7 (F) as the window ruptures,

ejecting electrolyte into the TEM column, and the column valves close to protect the electron gun.

A region inconsistent with the rest of the liquid can be seen in Figure 4.7 (D), in the top left-hand corner. It is unknown what causes this unusual appearance as it does not look like a standard bubble formation which are usually circular when generated by the beam. Two possibilities as to its origin are either a small solid deposition in the electrolyte moved across the flow path (although it moves with a much higher velocity than would be expected for something carried by the flow). The second possibility is that it is because of stress on the window as the dendritic growth continues. This seems the more likely explanation as the window fails a few seconds after this effect is seen. It is quite possible, due to how thin the window is (50 nm) and how narrow the liquid channel is (250 nm) that the dendritic formations seen in the images pierced the SiN_x membrane, or at the very least induced enough force to weaken them significantly. This can be mitigated in future tests by using a thicker liquid channel, although this would be at the expense of image resolution.

While no qualitative electrochemistry information was to be obtained from this in-situ test, it did nonetheless represent a significant result in terms of being able to image printed electrodes as they cycle in a liquid environment. A composite electrode can successfully be printed onto a liquid cell chip with relative ease and this cell can be cycled and imaged within an environment similar to one that materials would be exposed to in real devices. Unfortunately, due to the nature of the reactions occurring and the morphology of the holder itself, the exact composition and cause of the dendrite formation is unknown. It is unclear whether the dendrites are composed of the printed material, electrode material (or material from the adhesion layer) or are created by the breakdown of the aqueous electrolyte. EDX spectra cannot be obtained due to a shadowing effect caused by the shape of the liquid cell tip. The titanium aperture of the tip prevents X rays from being absorbed by the detector and as such the signal is dominated by the Ti signal provided by the tip itself.[24] While this shadowing does not cause a similar problem for EELs as it does for EDX, signals through thick liquid layers are very difficult to obtain due to the multiple scattering events caused by both windows and liquid. Despite this, it is hoped with further technical development of the process and the holder itself that chemical signals from EDX and EELS spectra can be routinely used. Thinner liquid layers, and thinner SiN_X membranes could bring the

background signal low enough to observe EELS spectra and physical modification of the holder itself could reduce the shadowing effect that prohibits EDX spectra from being obtained. [8,23,24]

It is also important that the area of interest that is to be viewed and analysed be as close as possible to the window edge. Minute changes in liquid thickness can have a very large effect on focus and resolution of material. This can be seen quite clearly in the differences in focus between frames in Figure 4.7. Localised changes in the electrolyte causes drastic differences in resolution and image quality.

With all these factors considered, the process still represents an incredibly promising method of examining the morphological changes that occur within energy storage devices. Due to the fact that supercapacitive materials should not undergo large physical changes (although the dendritic growth shown above may suggest otherwise), this morphological approach is far more useful in analysing battery anodes, specifically the lithiation induced alloying in Si nanomaterials.

4.6 Analysis of battery anodes and cathodes

The fundamental advantages and disadvantages of using silicon as a battery anode were detailed in the materials section of Chapter One. Despite its low conductivity and the pulverisation effects associated with the high volumetric changes the material undergoes, it is still a material of interest due to its low cost and low environmental impact. There has been considerable work towards combining Si nanoparticles with other materials to form composite-material electrodes. The purpose of these additives is to provide electrical conductivity and enhanced material strength to the Si electrodes.[25–28] Specifically, graphene encapsulation of Si nanoparticles has been presented as a very effective way of both increasing conductivity and inhibiting the swelling of the nanoparticles.[29] Investigating how different additives and synthesis methods affect the mechanical stability and conductivity of Si nanomaterial composites is the most promising application of the printed cell analysis demonstrated in this chapter and in Chapter 3, previously. Being able to accurately visualise how additives alter the morphological changes in Si nanoparticles could be very useful in determining the correct balance of Si and additives and allow for an understanding on a more fundamental level how these additives and composites behave.

Liquid cell TEM of battery materials is a more involved process however. Battery cells require both anode and cathode to function and, in most cases, require voltage sweeps outside the stability range of aqueous electrolytes. One particular issue is that of the power density of the devices themselves. Power density is one of the fundamental differentiating factors between supercapacitors and batteries. While in the previous tests, both ex-situ and in-situ, a cycle could be completed in a matter of seconds, this is not the case when testing battery materials. If in-situ experiments are to take place, the windows, material and electrolyte will have to be stable over the course of the electrochemical cycling, probably over the course of several hours rather than seconds. This presents a new, and unique set of experimental and technical challenges to be overcome.

4.6.1 Ex-situ testing of a battery cathode

The first step in the in-situ analysis of the two-electrode system was to ascertain if an electrochemical signal could be obtained from a printed cell. It was hoped that if intercalation peaks could be observed ex-situ, that this would narrow down the area of interest for in-situ TEM studies. Battery materials utilise wider voltage ranges and slower scan rates, making an observation of an entire cycle within the microscope difficult. If the intercalation peaks and thus the active voltage regions of the printed device can be located, the cell can be inserted selectively when charge storage is occurring. In addition to this, there is still a desire to be able to correlate CV responses with TEM images. Battery materials operate at a higher energy density and so it was hoped in this case, unlike for the supercapacitive material, that the sharp signal shown by alloying or intercalation would be observable above the baseline of the electrolyte in the cell.

A cell consisting of a $LiFePO_4$ working electrode with an activated carbon counter electrode was fabricated, as detailed in Chapter 3 and shown in Figure 4.8.

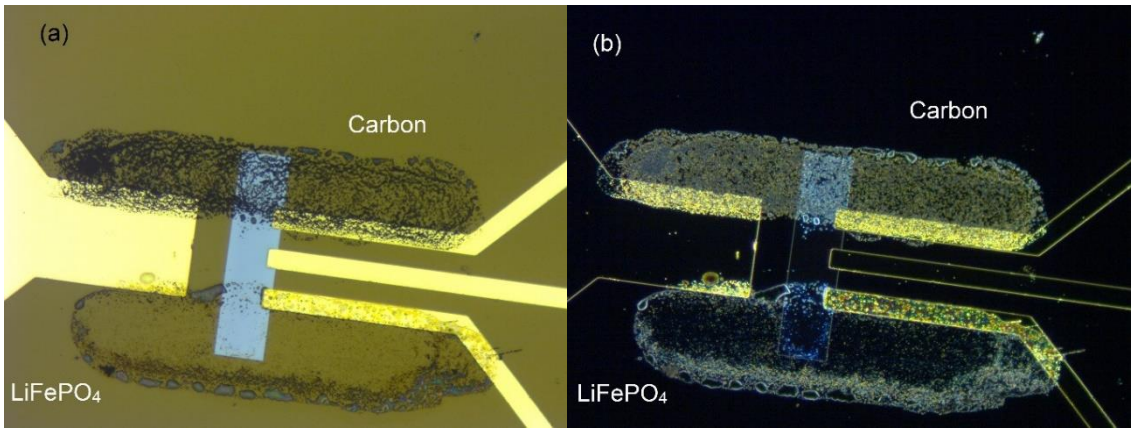

Figure 4.8: Optical microscopy images of a two electrode battery cell formed from carbon and LiFePO4 printed patterns showing (a) a bright field image of the deposited material and (b) showing a dark field image of the deposited material. Most of the contact line of the LiFePO4 has accumulated along the Au electrode.

$LiFePO_4$ is a well characterised material and has been investigated previously through in-situ experiments. A thoroughly characterised material was chosen so that any CV responses observed could be compared to published literature values of the material.[30–32] The primary difference between the standard literature values and those used in this experiment are the voltage ranges. $LiFePO_4$ is usually cycled to display the redox peaks between 3 and 4 V. For these tests an aqueous electrolyte was used, (0.1 M Li_2SO_4) and these voltage values are far higher than the electrolyte is stable at. While the voltage ranges are lower than the standard operating voltages of the material in an organic electrolyte, it is still expected that redox peaks should be observed within a 0 to 1 V range. These cells use a two-electrode setup and the potentials listed are the potentials between working and counter electrodes.

The $LiFePO_4$ cell was cycled between 0 and 1 V at a scan rate of 0.1 mV s^{-1} for 3 total cycles and the resulting CV curve from this ex-situ test is given in Figure 4.9;

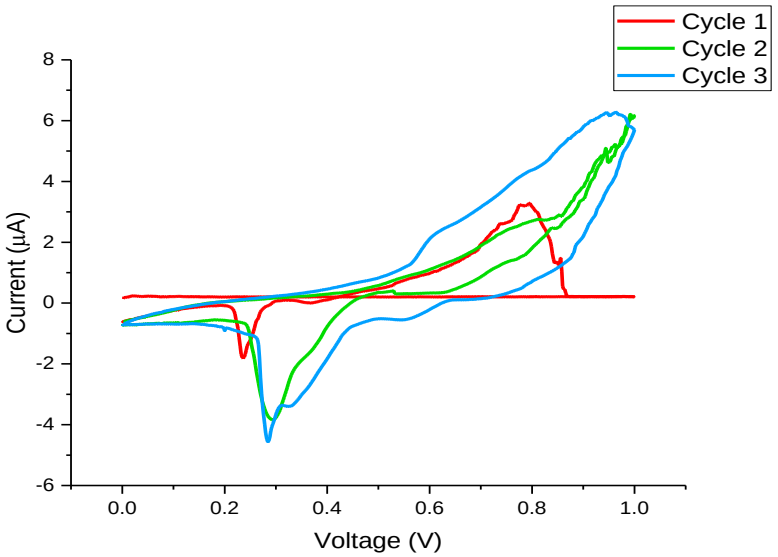

Figure 4.9: Three cycles of LiFePO4 with a carbon counter electrode. Peaks can be seen on the negative current section of the graph, but are difficult to discern for cycles 2 and 3 on the positive current portion of the graph.

The CV curve provided by the $LiFePO_4$ and carbon electrodes is distinctly different to those seen in the previous section. The first major difference that can be seen is the current that the cell is operating at. The cell reaches the µA range compared to the hundreds of nA seen for supercapacitive cells. In addition to this, some clear redox peaks can be seen within the cycles and the peak in cycle 3 of the test shows the double peak characteristic of the $LiFePO_4$-carbon storage. Unfortunately, the positive current section of the graph is largely obscured, with the slanting caused by ohmic shift visible in that region. The lack of peaks in this section of the graph suggests non-reversible reactions are occurring, although it is unclear if this is actually the case or if the peaks in this region are just obscured by noise or electrolyte effects. While this once again does not provide quantitative information on the material, it serves as a very important validation of the ex-situ and in-situ cycling process. As our peaks in shape and position are roughly in line with previously reported values for $LiFePO_4$ in Li_2SO_4 (~0.1 – 0.3 V)[33,34]

As was hoped, redox peaks from battery materials provide a far higher signal than the lower energy density supercapacitive materials and can provide a useful reference point for the expected areas of interest when the cells are located within

the TEM. Unfortunately this does come at the expense of cycle speed. The scans in Figure 4.9 had a total cycle time of over 16 hours, given the scan rate of 0.1 mV s^{-1}. It is not experimentally practical to cycle cells within the TEM for this length of time, however the redox peaks allow us to utilise a combination of both in-situ and ex-situ testing. The cell can be cycled outside the microscope in areas away from the redox peaks, and then viewed inside the microscope during the lithiation and de-lithiation of the material. This does not preclude the cell being cycled at all times within the microscope, although this can be limited by both vacuum stability and the reactivity of the electrolyte under the beam. Electrolyte stability is particularly important as the aqueous electrolyte used in this test is not appropriate for use in systems used later in this work which require organic electrolytes. This will necessitate a study of what organic electrolyte remains stable under the beam.

The successful cycling of the $LiFePO_4$ cathodes open up the opportunity to examine anode materials in-situ. Due to the limitations on chemical analysis caused by the liquid environment, most in-situ analysis of battery materials have focussed on morphological changes in the anode, and a similar approach will be adopted here to observe the volumetric expansion of Si nanoparticles and composites containing these particles.

4.6.2 Si nanoparticles for in-situ analysis of battery anodes

As has been described in detail in Chapter 1, Si is a material of interest for battery cathodes due to its high theoretical capacity. This capacity however has experimentally found to be limited by the pulverisation of the electrode by the volumetric expansion the Si undergoes during lithium ion storage[35–39]. This makes Si a perfect material for in-situ analysis because this volumetric expansion can be observed, as can the changes to that expansion caused by the addition of other materials to the Si anode. As with the $LiFePO_4$, cycle times are expected to be far longer than for the supercapacitive materials, usually in the range of 0.1 to 0.3 mV s^{-1}. Added to this, the ramp up time required to get the cell to the voltage window that is to be examined must also be taken into account. With the higher voltages that are required for Si nanoparticles in organic electrolytes, the cell requires much more time to reach the initial potential of the cell, E_1.

The Si nanoparticles we dispersed in IPA from a powder as supplied (Si nanopowder 98+%. 50-70nm Us Research Nanomaterials Inc) at a concentration of 5 mg ml^{-1}.

The listed particle size of the nanoparticles is in a range between 50 and 70 nm. The cells were fabricated as described in Chapter 3. Initially the organic electrolyte that was chosen for these tests was $LiPF_6$ in EC:DMC, a standard organic electrolyte used for Li ion battery work.

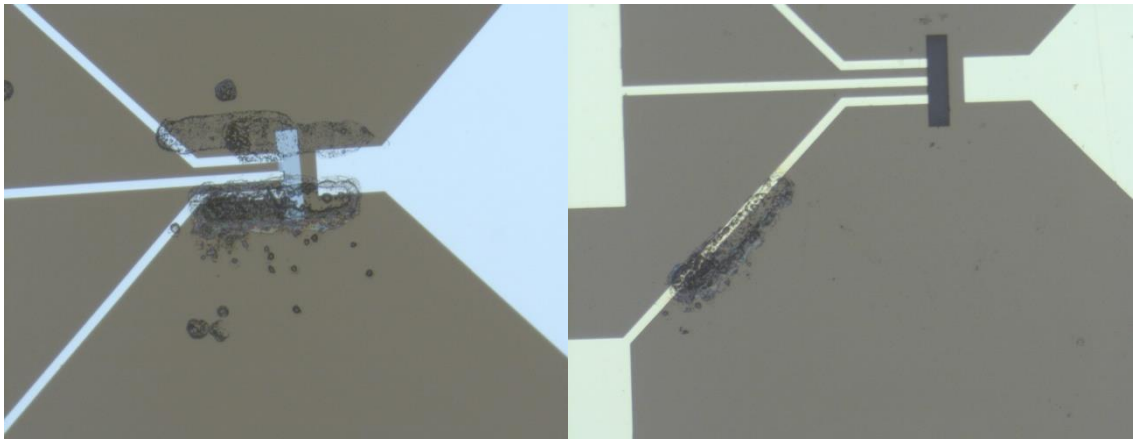

Figure 4.10: Si and $LiFePO_4$ printed onto the electrochemistry cells. The image on the left shows both Si and $LiFePO_4$ deposited onto the window. The image on the right shows the $LiFePO_4$ printed off the window, where a greater mass can be deposited.

4.6.3 Imaging of Si nanoparticles in a liquid electrolyte environment

One of the primary difficulties in imaging the nanoparticles through liquids is that of focus. As was seen for imaging of the supercapacitor electrodes consisting of layered materials, focus is difficult to achieve and can drift, due to small changes in the liquid layer. These issues are just as problematic for Si nanoparticles as they were for layered materials. Drastically adjusting the focus or Z position of the focussed beam can drastically alter the surrounding liquid, and so eliminating the characteristic white and black Fresnel fringes associated with over and under focus can prove very difficult.

Contrast also added a further complication to the imaging of Si NPs in the electrochemistry tip. As discussed previously, higher resolutions and the potential for usable chemical signals exist at the fringes of the SiN_x windows, due to the drastic increase of liquid path thickness in the centre of the windows. Owing to the low conductivity of the material being in used (both $LiFePO_4$ and Si have low conductivities) the area of interest is further restricted to the region on top of or adjacent to the metallic working and counter electrodes. The presence of the large mass of Au next to much smaller amounts of Si makes acquiring acceptable levels

of contrast difficult. Contrast improves as the imaging is moved further and further from the electrode itself, although this difficulty can be mitigated using STEM mode at the expense of focussing the beam into a much narrower spot size. STEM images could even resolve individual particles that were situated on the Au electrode itself. Smaller amounts of Si material are deposited when compared to the supercapacitive materials as the purpose of the experiments here are to observe the volumetric changes in individual particles.

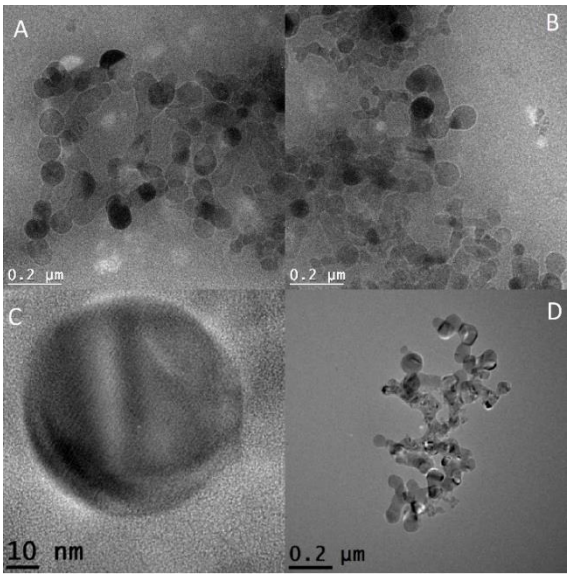

Figure 4.11: TEM images of Si NPs in both wet (A and B) and dry (C and D) environments. While resolution and focus are diminished in A and as compared to D, particles can still be resolved.

Figure 4.11 shows a typical TEM image of Si NPs in $LiClO_2$ in EC:DMC, taken away from the metallic electrode. Resolving individual nanoparticles is possible, although the white Fresnel fringes around some particles indicate how out of focus they are. As mentioned this is a very difficult artefact to correct given the liquid environment. For comparison, standard TEM images of Si NPs in a dry environment are also given.

This set of images provide a very useful indicator as to the effects that liquid has on imaging as images C and D from Figure 4.11 were taken in a dry electrochemistry cell, with no liquid between the spacer layers. From this we can see while the windows do take away some ability to resolve, the primary contributor to this is in fact the liquid. From A and B we can also see that the material connects to form reasonably good networks. Due to the low conductivity of Si nanoparticles it is

desirable to have as connected a network of particles as possible to provide a higher chance of usable conduction pathways occurring. There is a reasonably high variance in diameter of the particles observed in the images in A and B. A full statistical particle distribution of the images is difficult due to the overlapping particles, the poor focus and poor resolution but some information can be obtained. The mean particle size for A is 73 nm, with the largest particle being observed at 105 nm and the smallest at 42 nm. For B the mean was found to be 72 nm, with the largest particle at 107 nm and the smallest at 36 nm. The mean particle size is at the upper end of the suppliers range (50 to 70 nm) but this is in fact an advantage for imaging purposes. The larger images are easier to observe and resolve, but are not so large as to threaten the integrity of the window. The spacer layers used in these tests are only just an order of magnitude higher than the particle sizes, and large particles stacking can have detrimental effects on the windows.

With a non-degrading electrolyte selected and particles successfully resolved within the liquid cell, the next step was the attempt to cycle the material in-situ. The scans of the material were set with an initial voltage $E_0 = 0\,V$, $E_1 = 4\,V$ and $E_2 = 2.5\,V$. The scan rate was set at a slightly faster 0.2 mV s^{-1} than the previous $LiFePO_4$ tests. This change was primarily for practical reasons. The cell in question required cycling from 0 V to its initial voltage of 4 V. At 0.1 mV s^{-1}, this process would take 11 hours. By doubling the scan rate, we reduce this time, without completely compromising the expected swelling effects of the Si particles. Lithium insertion in Si has been found to be very sensitive to rate dependence and high scan rates will result in very little Li alloying and hence a low volumetric change. [40,41]

To achieve better contrast and be able to observe particles close to the Au electrode, the following images were taken in STEM mode. As there was a concern with electrolyte degradation over very long time scales, the STEM beam was blocked from the sample in between imaging in order to preserve the electrolyte. In ideal circumstances a full video sequence of the material would be taken, but for scans as long as those required for this test (15 Hours for a full 3 cycle test), a sequence of time resolved images will suffice. Images were taken at 5 minute or 60 mV intervals.

A comparison between the beginning of the cycle and the end of the first charge cycle is given in Figure 4.12. In STEM imaging mode, particles can be resolved even with the large mass of the Au electrode. In addition to this, very promisingly, individual particles can be resolved not just adjacent to the electrode, but directly on top it.

This is very important for imaging particles that are in good electrical contact with the system. Both the microscope images and the CV response show very little electrochemical changes occurring during the cell cycle.

The material of interest (directly adjacent to, or on top of the electrode) shows no discernible volume change. While there is no immediately discernible Li-insertion peaks visible, the CV curve does show minute changes in between 2.5 and 3 V, corresponding to the active region of the $LiFePO_4$ with this electrolyte and anode material. As itself, this can be seen as a promising result. The test was concluded after 6 hours due to window stability and time concerns, meaning only the charging sweep of the cell was measured.

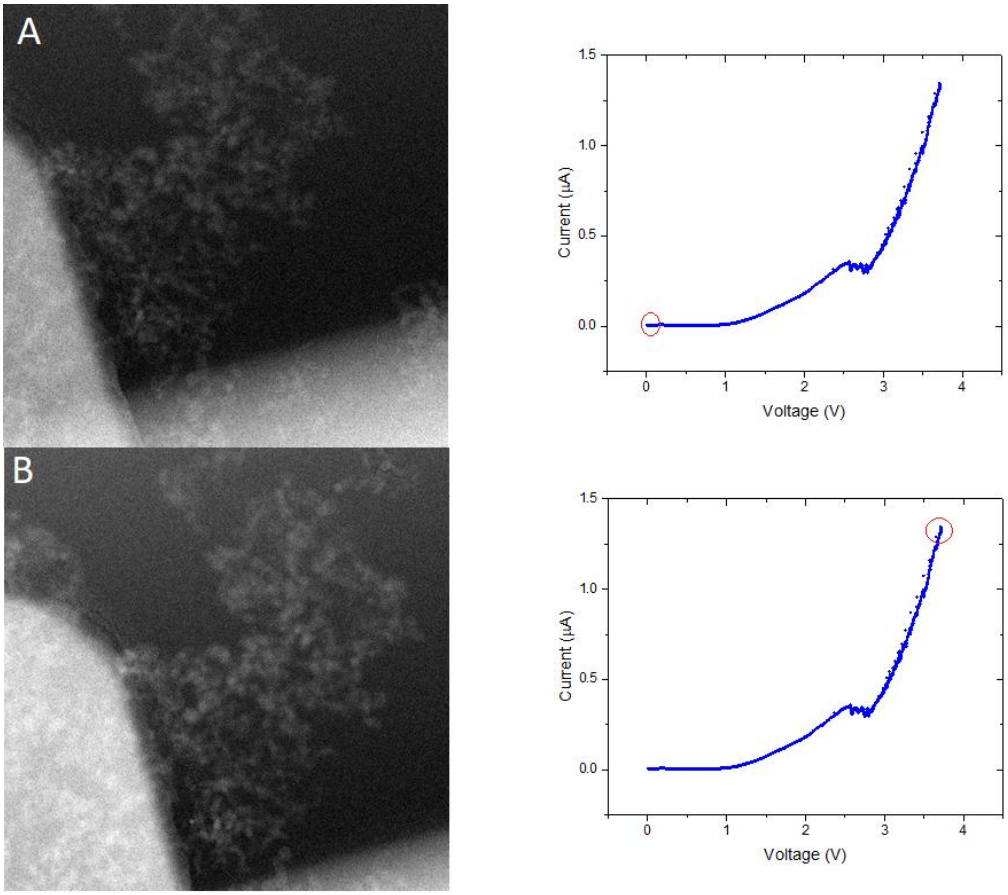

Figure 4.12: Image and CV comparisons of Si NPs deposited onto the Au electrode at (A) the beginning of the initial ramp up cycle at E0 and (B) the same electrode 6 hours later at 3.5 V when the test was concluded.

While the test provides no quantitative information, it is nonetheless useful from a technical and experimental point of view. While the cell does reach the microamp range, conductivity of the material itself is still clearly a problem. There is no change

observed even in the particles directly connected to the electrode. There are a number of potential solutions to this. Firstly, the mass deposited in these cells is quite low, with a total of 3.5 ng deposited over 5 staggered printing passes. In the printing of the Si NPs the print passes were not deposited on top of one another. Instead a layer was printed, and the successive layers were offset by ≈ 10 µm in order to preserve the window integrity. Nonetheless, this seems to be too low a mass of material to generate a response. The test conducted by Holtz *et al* where the in-situ response from $LiFePO_4$ and activated carbon reported a deposition of 30 ng of material. Increasing the mass of material deposited is certainly one avenue that should be investigated to acquire a better response from the material. It will also assist in forming a better-connected network of material.

The second solution is to increase the conductivity of the system. As has been mentioned previously, the low conductivity of Si NPs have been a major barrier in their commercial use.[28,42,43] The addition of carbon, CNTs or graphene to our inks could drastically improve their performance. Higher concentration composite inks can be created and printed successfully as was shown in previous sections of this work. Indeed, one of the primary motivating factors in conducting in-situ electrochemistry and TEM analysis of Si nanostructures in the first places was to investigate how the addition of carbon-based materials or conductive binds would affect the volumetric expansion of these materials.

From a microscopy perspective, higher resolution, better contrast and higher magnification are always desirable when examining the crystal structure of nanomaterials. To preserve the electrolyte over the long period of the test, the STEM beam was blocked between image acquisitions. A certain amount of drift in the focus of the microscope occurred between image acquisitions. Due to the small changes that occur in the electrolyte as it flows, longer exposure times do not necessarily assist in producing clearer images. Focussing the beam in the small window of time that was allowed for each voltage step is difficult. This can be aided by thinner liquid layers, although this approach can make the windows less stable and the electrochemical responses less representative to what a full-sized device may produce. Improving image contrast could be very easily done by changing the material used as the electrode on the cells. The cells used in this chapter were all either Pt or Au cells, high atomic number elements that can obscure imaging when placed next to much lighter elements. A solution to this contrast problem would to

utilise cells with a carbon working electrode, a feature commonly seen in liquid cell holders manufactured by Protochips (Morrisville NC, USA)[8,21,23,44,45] The much lower scattering of carbon would limit the contrast and spatial resolution loss to just that caused by the liquid electrolyte.

4.6.4 Degradation of liquid electrolytes under exposure to the electron beam.

Organic electrolytes tend to degrade in both air and water. For this reason, the organic electrolytes used in these tests were transported and stored in a gas syringe which was capped with Ar from an Ar glove box. Some publications suggest assembling the entirety of the cell and tip within an Ar environment in order to avoid the electrolyte degrading. This assembly process is not possible in this case for logistical reasons, but every effort is taken to avoid electrolyte exposure. The cell itself is fully assembled dry, and the Ar capping layer within the syringe is then pumped through the assembled cell. Electrolyte that has flowed through the fluid lines and the tip is then deposited into a beaker of IPA to avoid outside contamination.

On insertion of the tip into the electron beam path, the degradation of the organic electrolyte was immediately apparent. Irradiated areas of the electrolyte become electron opaque, and particle resolution becomes impossible. Lower intensity beam currents were found to only slow this process, not stop it, with standard beam currents and intensities used in the previous imaging experiments degrading areas of the electrolyte completely in a matter of seconds.

The origin of this degradation is difficult to determine. Several factors could contribute to the onset of electron opacity that was seen. The first question is if this degradation is inherent to the electrolyte chosen or is it as a result of small amounts of air or water exposure that change the chemical composition, causing instabilities within the solvent and salt that are then exacerbated by the incident electron beam. Solvent quality is also a consideration. As it has been seen to have been used without any similar reported degradation in other publications, [45,46] we can only determine that degradation of the electrolyte has occurred outside of the TEM column. This presents a concern since $LiPF_6$ hydrolyses, producing HF.[47] For obvious reasons the production of HF within the liquid cell holder and within the TEM column is not desired. The degradation of the electrolyte and introduction of gas pockets or salt

deposits within the cell also causes undue stress on the already very fragile windows. As such, an electrolyte study was required to determine an electrolyte that would be effective in reproducing a Si battery cell, but also be stable under the beam conditions.

Abellan *et al* conducted an electrolyte study for the most commonly used electrolytes used in Li ion batteries and how they degrade under continued beam exposure.[48] In this study, they found the EC:DMC solvent commonly used as a salt carrier does not react under the electron beam in TEM and STEM modes. Therefore, degradation of the electrolyte is dependent on the salt added. The first electrolyte used in our own tests was a LiTf (Lithium trifluoromethanesulfonate) in Propylene Carbonate (PC). The electrolyte was kept under argon in the same manner as the $LiFP_6$ in EC:DMC. It was then flowed into an empty cell and analysed under the beam.

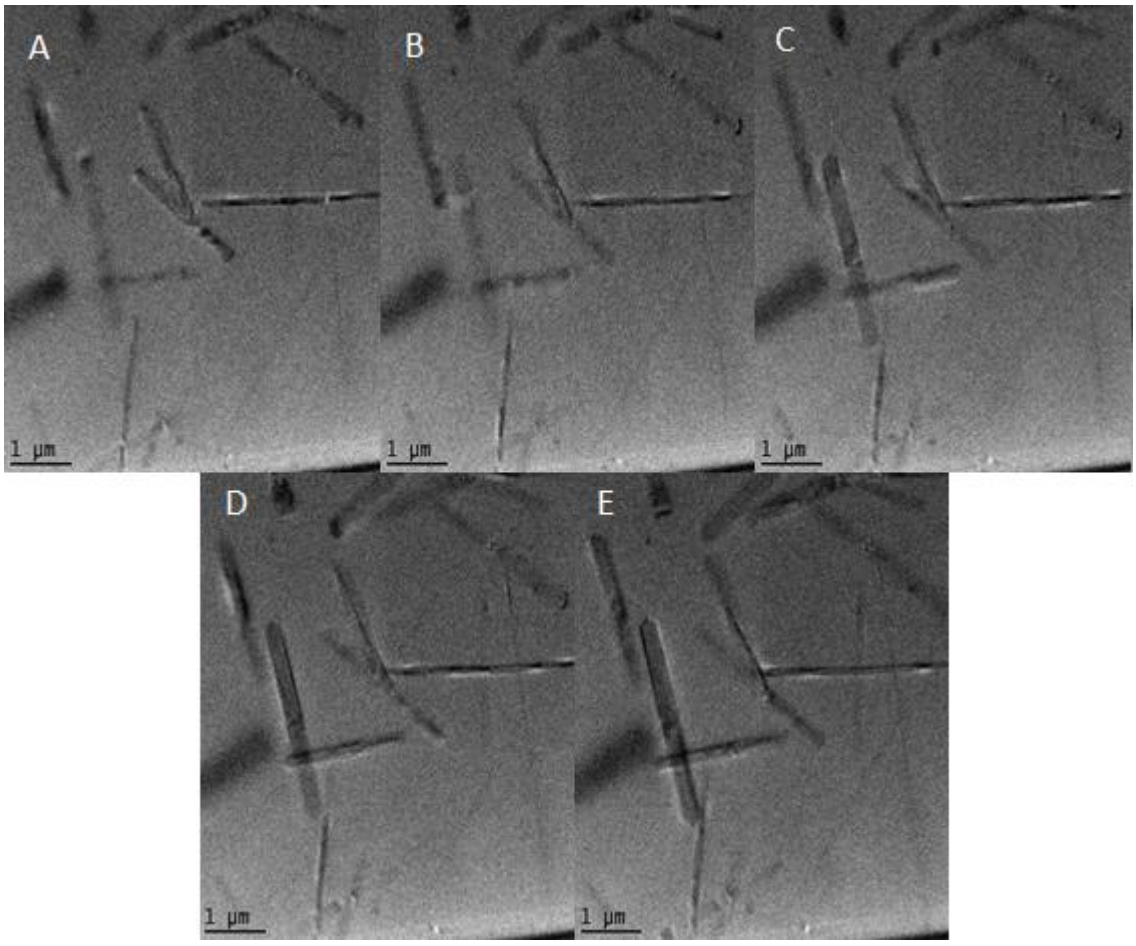

Figure 4.13: Time evolution of LiTf in PC. Rod like structures can be seen forming under the beam. The initial viewing area was clear of material at the beginning of beam exposure.

The degradation of the LiTf in PC can be seen in Figure 4.13. The electrolyte degrades into visible nanorods under exposure to the beam. The rods begin as

smaller, less resolved structures but continue to grow and evolve as long as they are exposed to the beam. The time scale shown in the sequence of images in Figure 4.10 is 180 seconds from image A to image E. Removing the beam from these areas was found to stop their growth, which immediately resumed when the previously irradiated region was brought back under the beam. Similar nanorod structures were reported by Abellan *et al* but for $LiAsF_6$ in 1,3-dioxolane (DOL).[48] They attributed this growth pattern to an incomplete degradation of the organic within the electrolyte, causing preferential growth directions to occur under the beam. Under EELS analysis they determined that the nanorods in their case were composed of arsenic related degradation products (AsF_3 or As^0). For this work, these nanorods form far too rapidly for the electrolyte to be considered for use, although further analysis may be warranted if these rods exhibit the same chemical compositions as is found in the SEI of devices using this electrolyte (as was found to be the case in Ref 36)

A second commonly used electrolyte that was investigated was $LiClO_4$ in DC:EMC. This electrolyte was analysed in the same manner as before but showed a different degradation pattern. As shown in Figure 4.14, the electrolyte formed distinct nanoparticles that increased in size under the beam. The particles themselves are distinct, showing quite sharp contrast under the beam, and exhibited none of the preferential growth directions that were seen in for the LiTf in PC electrolyte.

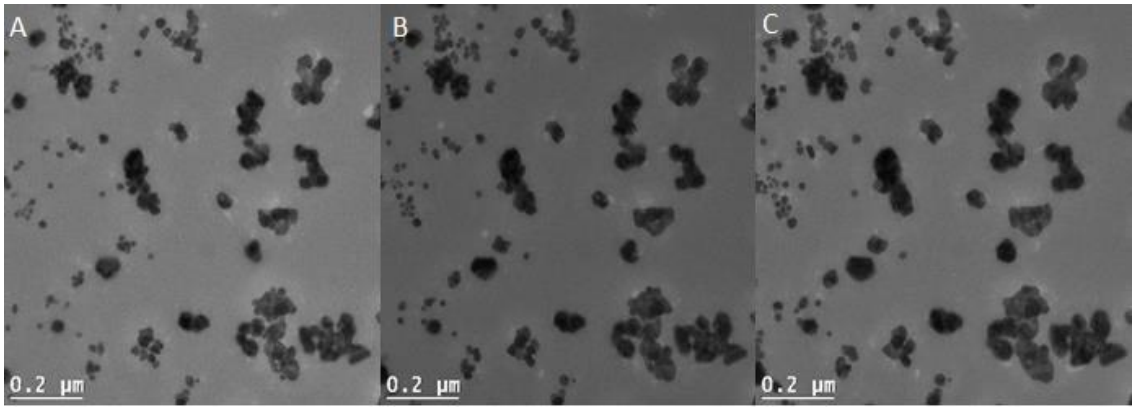

Figure 4.14: Generation of solid material under the beam from LiClO4 in EC:DMC. Window is clear of all material prior to experiment. Crystals appear under the beam and continue to get larger for as long as they are exposed to the incident beam.

Particles that are closer together grow and form larger clusters, as can be seen in the large grouping of initially very small crystals in the bottom right hand side of Figure 4.14 (A). This cluster visibly increases in size until many of the particles

combine into a larger matrix, as seen in the same position of Figure 4.14 (C). On closer inspection in certain regions, the growth of the particles under the beam is significant. It is not known what the particles are formed from, but it is reasonable to believe that they are composed of the lithium salt, which has the potential to short the cell, or at the very least effect the performance significantly

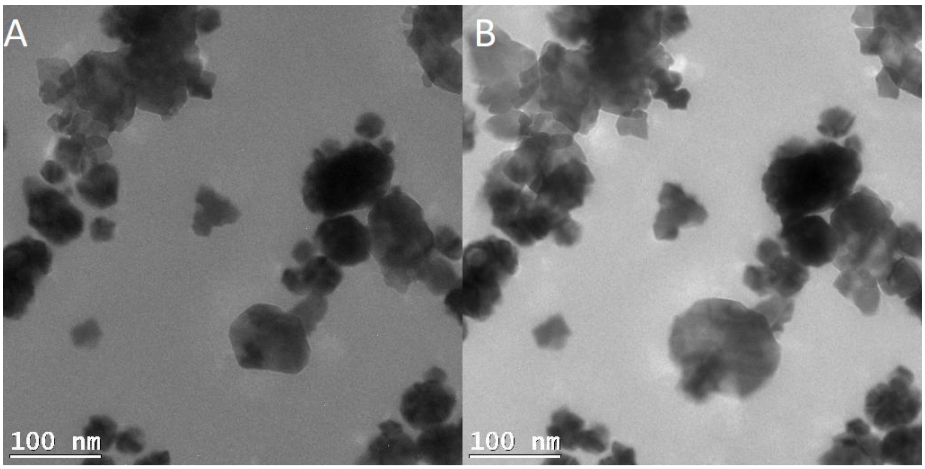

Figure 4.15: Expansion of beam induced particles under higher magnification. Higher magnifications put smaller areas of the cell under higher intensities, accelerating the degradation process Between A and B, dendritic formations can begin to be seen in the upper left region of the images.

After a few minutes of beam exposure at higher magnifications, the crystallisation and dendritic formation within the electrolyte becomes almost complete, obscuring the whole field of view of the image, and rendering the area unusable, as shown in Figure 4.16. Interesting to note is what appears to be a two-step process in this degradation. The first step consists of a nucleation of degradation products forming small crystals under the electron beam. These crystals continue to grow under the

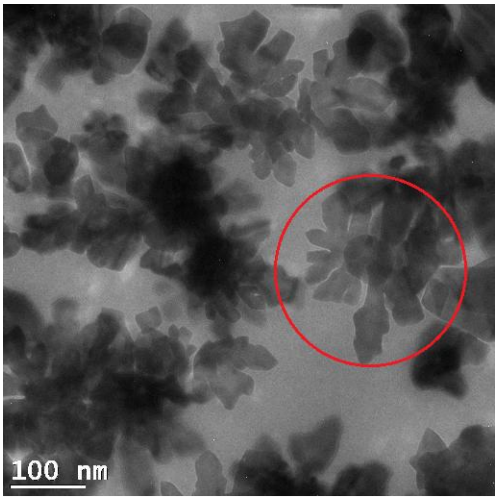

Figure 4.16: Dendritic formation from a core crystal under the beam. Nucleation of the central crystal slows and is replaced with dendritic growth outward.

beam. At a certain point, this expansion slows and shifts into a more dendritic expansion occurring outwards from the core of the crystal.

Lowering the beam intensity and increasing the spot size of the electron beam with the $LiClO_4$ in EC:DMC electrolyte did appear however to mitigate the particle formation/dendrite formation. In addition, a lower salt concentration (0.1 M compared to initial tests at 1 M) was found to further reduce the effects of the beam on the electrolyte. While this does limit resolution, it is a necessary tradeoff in order to actually be able to image the material and be able to confirm that any physical changes that are seen during cycling are in fact caused by electrochemical cycling and not the incident beam. Caution must still be taken in focusing the beam and changing the Z position of the focus as organic electrolytes are still susceptible to the bubble formation that was observed in the aqueous electrolyte tests.

Finding a stable electrolyte is vital to being able to conduct the long time-scale tests that were seen in the previous section. It is impossible to accurately examine physical changes in the cell if there is a possibility that these physical changes are either induced by electrolyte degradation or are electrolyte degradation. While these tests found an electrolyte that worked for this system, further work on electrolyte degradation and appropriate salt and solvent combinations are required.

4.7 Conclusions

In this chapter, the electrochemical cycling and imaging of several different energy storage systems was presented. Low mass printed electrodes of a MnO_2-Graphene composite were cycled at a number of voltage ranges, but it was found that no observable signal could be viewed at this mass above the base electrochemical response of the electrodes immersed in the K_2SO_4 electrolyte. Similar behaviour was observed when the amount of material deposited was increased tenfold from 5 layers to 50 layers, although it is possible that some response is observed in the 600 mV to 700 mV range. A 50-layer device was assembled into the liquid cell holder and cycled within the TEM column. During the short duration of the test dendritic growth was observed as the electrode charged and discharged suggesting the presence of electrochemical processes occurring below the current threshold of the cell itself. The origin of these dendritic formations is unknown, although the most likely cause

is a possible electrolyte decomposition. The SiN_x windows of the cell failed before meaningful chemical data could be extracted.

The effects of the incident electron beam on common organic electrolytes were studied. Depending on the salt type and concentration electrolytes can rapidly degrade under the incident electron beam. Lower concentrations can mitigate this, as can lowering the overall beam dosage by enlarging the spot size and lowering the beam intensity. This characterisation allowed for the use of an electrolyte, $LiClO_4$ in EC:DMC, that initially was found to degrade rapidly under the beam. Other electrolytes were not used for the safety of both the operators and so as not to damage the liquid cell holder tip.

Battery type materials were then tested, firstly to verify the function of the cell setup and secondly to observe the volumetric changes that are known to occur in Si nanoparticles as they charge and discharge. Firstly, a cell was conducted consisting of a $LiFePO_4$ working electrode and a carbon counter electrode. This cell was filled with 0.1 M aqueous Li_2SO_4 electrolyte and cycled between 0 and 1 V. The cell yielded what are believed to be redox peaks for the intercalation of the Li ions into the carbon structure, although some peaks are obscured by noise from the cell and/or ohmic shift due to the thin electrolyte layer. Si nanoparticle electrodes were then tested in situ but due to low total mass of active material, poor conductivity of the active material or a combination of both, no clear electrochemical signals were observed. Some signal was seen between 2.5 and 3V, the expected region of activity for the Si NP- $LifePO_4$ system, but further tests will be required to verify this. Reasonable resolution of the particles can be achieved when the particles are observed through STEM mode, but great care must be taken not to damage the electrolyte through beam irradiation. The particles were similarly viewed in standard TEM mode where individual nanoparticles down to 30 nm could be successfully resolved although focussing the beam through the liquid is difficult.

While imperfect, the process presented in this chapter can act as a foundation for further electrochemical testing. Higher concentration inks can be prepared, as can inks with additives that can increase the conductivity of the materials. For a highly responsive material, such as the $LiFePO_4$, reasonably good responses were observed. With changes to the synthesis and printing processes of the material, similar electrochemical responses can be attained from Si based electrodes and the morphological changes mapped in-situ. In addition to this, with refinement of the

holder itself and the way that electrodes are deposited, it is believed that the EELS signals could be used to fully identify the electrochemical processes involved in the charge and discharge processes of supercapacitor electrodes that incorporate pseudocapacitive materials like MnO_2

Bibliography

1. Jonge, N. d., Peckys, D. B., Kremers, G. J. & Piston, D. W. Electron microscopy of whole cells in liquid with nanometer resolution. *Proc. Natl. Acad. Sci.* **106,** 2159–2164 (2009).

2. Liu, K. L. *et al.* Novel microchip for in situ TEM imaging of living organisms and bio-reactions in aqueous conditions. *Lab Chip* **8,** 1915–1921 (2008).

3. De Jonge, N. & Ross, F. M. Electron microscopy of specimens in liquid. *Nat. Nanotechnol.* **6,** 695–704 (2011).

4. Lu, X., Bogart, T. D., Gu, M., Wang, C. & Korgel, B. A. In Situ TEM Observations of Sn-Containing Silicon Nanowires Undergoing Reversible Pore Formation Due to Fast Lithiation/Delithiation Kinetics. *J. Phys. Chem. C* **119,** 21889–21895 (2015).

5. Liu, X. H. & Huang, J. Y. In situ TEM electrochemistry of anode materials in lithium ion batteries. *Energy Environ. Sci.* **4,** 3844–3860 (2011).

6. Gu, M. *et al.* Demonstration of an electrochemical liquid cell for operando transmission electron microscopy observation of the lithiation/delithiation behavior of Si nanowire battery anodes. *Nano Lett.* **13,** 6106–6112 (2013).

7. Unocic, R. R. *et al.* Direct visualization of solid electrolyte interphase formation in lithium-ion batteries with in situ electrochemical transmission electron microscopy. *Microsc. Microanal.* **20,** 1029–1037 (2014).

8. Holtz, M. E. *et al.* Nanoscale imaging of lithium ion distribution during in situ operation of battery electrode and electrolyte. *Nano Lett.* **14,** 1453–1459 (2014).

9. Zheng, H. *et al.* Observation of transient structural-transformation dynamics in a Cu2S nanorod. *Science (80-.).* **333,** 206–209 (2011).

10. Golberg, D., Bando, Y., Stéphan, O. & Kurashima, K. Octahedral boron nitride fullerenes formed by electron beam irradiation. *Appl. Phys. Lett.* **73,** 2441–2443 (1998).

11. Yokota, T., Murayama, M. & Howe, J. M. In situ transmission-electron-microscopy investigation of melting in submicron al-si alloy particles under electron-beam irradiation. *Phys. Rev. Lett.* **91,** 265504 (2003).

12. Sepulveda-Guzman, S. *et al.* In situ formation of bismuth nanoparticles through electron-beam irradiation in a transmission electron microscope. *Nanotechnology* **18,** 335604 (2007).

13. Matsui, S. & Ichihashi, T. In situ observation on electron-beam-induced chemical vapor deposition by transmission electron microscopy. *Appl. Phys. Lett.* **53,** 842–844 (1988).

14. Mildner, S. *et al.* Environmental TEM Study of Electron Beam Induced Electrochemistry of $Pr_{0.64}Ca_{0.36}MnO_3$ Catalysts for Oxygen Evolution. *J. Phys. Chem. C* **119,** 5301–5310 (2015).

15. Evans, J. E. *et al.* Visualizing macromolecular complexes with in situ liquid scanning transmission electron microscopy. *Micron* **43,** 1085–1090 (2012).

16. Jungjohann, K. L., Evans, J. E., Aguiar, J. A., Arslan, I. & Browning, N. D. Atomic-scale imaging and spectroscopy for in situ liquid scanning transmission electron microscopy. *Microsc. Microanal.* **18,** 621–627 (2012).

17. Fahrenkrug, E., Alsem, D. H., Salmon, N. & Maldonado, S. Electrochemical Measurements in In Situ TEM Experiments. *J. Electrochem. Soc.* **164,** H358–H364 (2017).

18. Pang, S. C. & Anderson, M. A. Novel electrode materials for electrochemical capacitors: Part II. Material characterization of sol-gel-derived and electrodeposited manganese dioxide thin films. *J. Mater. Res.* **15,** 2096–2106 (2000).

19. Nagarajan, N., Cheong, M. & Zhitomirsky, I. Electrochemical capacitance of MnOx films. *Mater. Chem. Phys.* **103,** 47–53 (2007).

20. Yan, J. *et al.* Fast and reversible surface redox reaction of graphene-MnO2composites as supercapacitor electrodes. *Carbon N. Y.* **48,** 3825–3833 (2010).

21. Unocic, R. R. *et al.* Quantitative electrochemical measurements using in situ ec-S/TEM devices. *Microsc. Microanal.* **20,** 452–461 (2014).

22. Yang, C. *et al.* Direct Observations of the Formation and Redox-Mediator-Assisted Decomposition of Li $_2$ O $_2$ in a Liquid-Cell Li-O $_2$ Microbattery by Scanning Transmission Electron Microscopy. *Adv. Mater.* **29,** 1702752 (2017).

23. Holtz, M. E., Yu, Y., Gao, J., Abruña, H. D. & Muller, D. A. In situ electron energy-loss spectroscopy in liquids. *Microsc. Microanal.* **19,** 1027–1035 (2013).

24. Zaluzec, N. J., Burke, M. G., Haigh, S. J. & Kulzick, M. A. X-ray Energy-Dispersive Spectrometry During In Situ Liquid Cell Studies Using an Analytical Electron Microscope. *Microsc. Microanal.* **20,** 323–329 (2014).

25. Park, S. H. *et al.* Spray-assisted deep-frying process for the in situ spherical assembly of graphene for energy-storage devices. *Chem. Mater.* **27,** 457–465 (2015).

26. Higgins, T. M. *et al.* A Commercial Conducting Polymer as Both Binder and Conductive Additive for Silicon Nanoparticle-Based Lithium-Ion Battery Negative Electrodes. *ACS Nano* **10,** 3702–3713 (2016).

27. Luo, J. *et al.* Crumpled Graphene-Encapsulated Si Nanoparticles for Lithium Ion Battery Anodes. *J. Phys. Chem. Lett.* **3,** 1824–1829 (2012).

28. Lee, J. K., Smith, K. B., Hayner, C. M. & Kung, H. H. Silicon nanoparticles–graphene paper composites for Li ion battery anodes. *Chem. Commun.* **46,** 2025 (2010).

29. Park, S.-H. *et al.* Self-assembly of Si entrapped graphene architecture for high-performance Li-ion batteries. *Electrochem. commun.* **34,** 117–120 (2013).

30. Huang, H., Yin, S.-C. & Nazar, L. F. Approaching Theoretical Capacity of LiFePO[sub 4] at Room Temperature at High Rates. *Electrochem. Solid-State Lett.* **4,** A170 (2001).

31. Li, J., Armstrong, B. L., Kiggans, J., Daniel, C. & Wood, D. L. Lithium Ion Cell Performance Enhancement Using Aqueous LiFePO 4 Cathode Dispersions and Polyethyleneimine Dispersant. *J. Electrochem. Soc.* **160,** A201–A206 (2013).

32. Tang, W. *et al.* Aqueous rechargeable lithium batteries as an energy storage system of superfast charging. *Energy Environ. Sci.* **6,** 2093 (2013).

33. Gordon, D. *et al.* Enhancing Cycle Stability of Lithium Iron Phosphate in Aqueous Electrolytes by Increasing Electrolyte Molarity. *Adv. Energy Mater.* **6,** 1501805 (2016).

34. Sauvage, F., Laffont, L., Tarascon, J.-M. & Baudrin, E. Factors affecting the electrochemical reactivity vs. lithium of carbon-free LiFePO4 thin films. *J. Power Sources* **175,** 495–501 (2008).

35. Nitta, N., Wu, F., Lee, J. T. & Yushin, G. Li-ion battery materials: Present and future. *Mater. Today* **18,** 252–264 (2015).

36. Liu, X. H. *et al.* Anisotropic swelling and fracture of silicon nanowires during lithiation. *Nano Lett.* **11,** 3312–3318 (2011).

37. Liu, X. H. *et al.* Size-Dependent Fracture of Silicon Nanoparticles During Lithiation. *ACS Nano* **6,** 1522–1531 (2012).

38. Xu, Z. L. *et al.* Carbon-coated mesoporous silicon microsphere anodes with greatly reduced volume expansion. *J. Mater. Chem. A* **4,** 6098–6106 (2016).

39. Zuo, X., Zhu, J., Müller-Buschbaum, P. & Cheng, Y.-J. Silicon based lithium-ion battery anodes: A chronicle perspective review. *Nano Energy* **31,** 113–143 (2017).

40. Chandrasekaran, R., Magasinski, A., Yushin, G. & Fuller, T. F. Analysis of Lithium Insertion/Deinsertion in a Silicon Electrode Particle at Room Temperature. *J. Electrochem. Soc.* **157,** A1139 (2010).

41. Wu, J. J. & Bennett, W. R. Fundamental investigation of Si anode in Li-Ion cells. in *2012 IEEE Energytech* 1–5 (IEEE, 2012). doi:10.1109/EnergyTech.2012.6304667

42. Yin, Y. X., Wan, L. J. & Guo, Y. G. Silicon-based nanomaterials for lithium-ion batteries. *Chinese Sci. Bull.* **57,** 4104–4110 (2012).

43. Ge, M. *et al.* Scalable preparation of porous silicon nanoparticles and their application for lithium-ion battery anodes. *Nano Res.* **6,** 174–181 (2013).

44. Chen, X., Li, C. & Cao, H. Recent developments of the in situ wet cell technology for transmission electron microscopies. *Nanoscale* **7,** 4811–4819 (2015).

45. Wu, F. & Yao, N. Advances in sealed liquid cells for in-situ TEM electrochemial investigation of lithium-ion battery. *Nano Energy* **11,** 196–210 (2015).

46. Dollé, M., Grugeon, S., Beaudoin, B., Dupont, L. & Tarascon, J.-M. In situ TEM study of the interface carbon/electrolyte. *J. Power Sources* **97–98,** 104–106 (2001).

47. Xu, K. Nonaqueous Liquid Electrolytes for Lithium-Based Rechargeable

Batteries. (2004). doi:10.1021/CR030203G

48. Abellan, P. *et al.* Probing the Degradation Mechanisms in Electrolyte Solutions for Li-Ion Batteries by in Situ Transmission Electron Microscopy. *Nano Lett.* **14,** 1293–1299 (2014).

Chapter 5: Inkjet printing of flexible, planar supercapacitors

5.1 Flexible, printed electronics

As has been seen in the previous sections, inkjet printing can be used to rapidly and accurately deposit material inks. Until this point of the work, printing has been used for very small scale depositions, on the hundreds of microns in scale and with patterns no more complicated than single printed lines. However this case can be considered as an outlier, most inkjet printing of electronics is conducted for much larger scaled devices. The importance of the work that has proceeded and what is to follow is that the same materials and methods are used for both. The LPE exfoliation and synthesis routes that were used to provide inks previously, are the same used for larger, macro scale devices. This continuity of synthesis and deposition is vital to maintaining a link between the analysis steps performed in the previous sections, and the final production of large scale, potentially commercial devices that is to be shown in this chapter.

Inkjet printing is a method of deposition that holds vast potential for the fabrication of lightweight and flexible electronics. It has shown immense promise in the fabrication of Thin Film Transistors (TFTs)[1–5], photovoltaics[6–11] and of course in energy storage devices[12,13,22,14–21]. There are number of reasons why this process has garnered so much interest in the field of electronics manufacturing. The first advantage is cost and ease of use. Compared to photolithography, inkjet printing does not require large amounts of cleanroom space, expensive chemicals and labour-intensive processing steps[22]. The process is additive, using only the materials that are needed to form the printed patterns, and having very little waste. It can take advantage of liquid, solution processed material inks.[5,23–25] Nanomaterial inks produced by ultrasonication or shear mixing can be used almost directly in most printed processes. In addition, the process is largely not substrate limited. A wide range of materials are available to act as a substrate for printed patterns. Flexible polymers that would not be appropriate in other deposition systems due to temperatures exceeding the T_g (glass transition temperature) or due to the presence

of harsh chemicals, can be easily used in inkjet printing systems. A benefit to the inkjet printing process is that it can be upscaled to an industrial level. There are no inherent limitations on lab based systems being adapted for industrial and commercial design.

Considering this, energy storage devices consisting of nanomaterial electrodes which have been inkjet printed onto flexible substrates represent a very real step forward in the manufacture of next-generation electronics, particularly for systems where low weight and flexibility are requirements rather than added benefits. In this chapter the process of ink selection and printing for planar, flexible inkjet printed supercapacitors will be demonstrated. Two approaches in device fabrication will be taken; devices fabricated entirely from a single material functioning as both current collector and active material, and a second process where two materials are printed, acting separately as current collector and active energy storage material. Ease and simplicity in the fabrication process is the desired outcome in this case and the primary aim is to achieve an all-inkjet printed system, requiring no supplementary fabrication steps before, during or after the printing of the device. This simplicity of manufacture is essential to the upscaling potential of the process.

5.2 Planar vs multi-planar

The devices presented in this section are all interdigitated planar devices. They are not based on a multi-planar, sandwich structure sometimes seen in supercapacitor architecture, most commonly represented by pouch or rolled cells.[26,27] (The nomenclature for these devices varies wildly in the literature. For ease, planar in this text will refer to a device whose positive and negative electrodes lie along the same horizontal plane). This is an important design consideration that fundamentally decides how the devices are fabricated. In a traditional sandwich system, two flat electrodes will be printed or deposited separately. An intervening separator layer and electrolyte is placed between the electrodes. This is then sealed to prevent leakages or excess air or moisture getting into the cell. Some cells are then rolled into a cylindrical configuration in order to save space or fit a particular configuration.

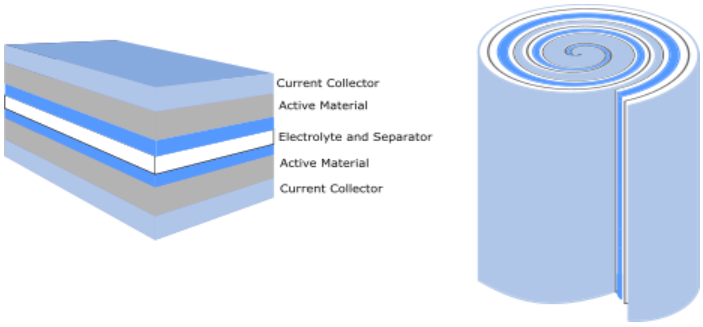

Figure 5.1: A typical sandwiched capacitor consisting of multiple layers of deposited material. The right -hand side shows the configuration taken when the same layers of sandwiched material are rolled into a cylindrical cell.

While the sandwiched structure provides a large electrode-electrolyte surface area on which to store charge, it does suffer from a number of drawbacks. The configuration is bulkier than planar devices, and the fabrication methods involved, requiring a number of assembly steps, mean that the devices themselves are difficult to include in integrated circuitry.[28,29] The planar, interdigitated design used in this work seeks to overcome some of these issues, and develop devices that can be seamlessly integrated into circuitry and larger devices. Interdigitated devices have been found to have a higher power density than multiplanar devices.[28–30] This is due to the fact that ions are transferred laterally between the electrode and the electrolyte, allowing for quicker ionic diffusion and without the interference of a separator or binders.

The interdigitated form allows for the electrodes to be placed much closer than would normally be allowed in a sandwiched, multi-planar device while still maintain safety as the electrodes do not come close in "pinch points" close to the edges that are common in sandwiched devices. Planar devices are also by their nature more compact. When deposited on flexible substrates this makes them ideal for requirements where flexible and thin storage solutions are required such as for wearable devices, flexible displays or smart-sensors.[31] When the electrolyte is appropriately encapsulated, interdigitated planar devices can be rolled and folded to match the form factor require with relative ease.[31] Interdigitated devices are also the simplest way to design a supercapacitor for production by inkjet printing. As both electrodes, and active material layers if needed, can be deposited in the same print pass, additional fabrication steps are limited, and there are fewer concerns with correctly aligning the overlapping electrodes as happens for a sandwiched device.

5.3 Inkjet Printing of MXene electrodes for supercapacitors

MXenes, and specifically $Ti_3C_2T_x$, boast electric properties that make them ideal for use as supercapacitor electrodes, possessing a high conductivity (~10000 S cm)[32] a good ability to store charge by intercalating ions,[33] and an ability to utilise metal redox reactions to store charge.[32] The combination of these three specific properties means that MXenes provide a very unique opportunity to produce a supercapacitor that requires only MXenes and an electrolyte to function. This would allow for the very rapid fabrication of large numbers of devices and would be particularly useful in minimizing the number of fabrication steps required for the production of larger scale integrated circuitry.

As such, a number of different MXene based inks were prepared in order to determine which solvent resulted in the most stable and effective material ink, and which of these inks would provide the best performing device.

5.3.1 Characterising the print parameters for MXenes dispersed in different organic solvents.

The MXene material was initially prepared in a manner similar to that as described in Chapter 1. The precursor MAX phase, Ti_3AlC_2 was etched to a MXene material by a combination of LiF and 9 M HCl. The resulting dispersion is centrifuged (1500 RPM, 423 x *g* 3 mins) to separate etched and non-etched material and the supernatant from this initial centrifugation is then repeatedly washed with DI water, shaken and centrifuged(1500 RPM, 423 x *g* 3 mins) in order to lower the pH of the supernatant. This is then filtered and dried, leaving just dried, powdered material, ready for dispersion into given solvents. This material is multi-layered and not well exfoliated at this point.

For organic solvents, the multi-layered material is initially dispersed into DI water, and shaken vigorously to separate the multi-layered flakes into few- or single layer $Ti_3C_2T_x$ flakes. This material is then centrifuged at a very high speed (10000 RPM) to separate the material from the DI water, which is then removed. The solvent of choice is then added to the sediment to re-disperse it. This dispersion is sonicated to separate the flakes once more, and then centrifuged so that only few- or single layer flakes remain. The sediment from these steps can be re-sonicated and re-dispersed

to increase the desired concentration, or more solvent can be added to lower the concentration.

The four organic solvents used in this work to disperse the material were Dimethylformamide (DMF), Dimethyl Sulfoxide (DMSO), Ethanol and N-Methyl-2-pyrrolidone (NMP). These solvents were primarily selected due to the long term stability of $Ti_3C_2T_x$ sheets when dispersed, showing stability up to 96 hours after initial dispersion without visible aggregation.[34]

The initial characterisation carried out was to determine if all 4 inks could be successfully printed. NMP as a printing solvent was used in unrelated experiments prior to this, and is generally regarded as a very good ink solvent due to the ease with which NMP droplets can be generated in our chosen printing system (Fujifilm Dimatix DMP 2850 materials printer). Intensive waveform development was not required for this ink, as previously used NMP waveforms and voltage parameters yielded well-formed droplets with little or no satellite droplet formation. The ethanol ink was found to initially not be printable. The calculated Z value for ethanol is 16.05, lying slightly outside the usually accepted range. The major outlier in terms of the physical properties of ethanol is its viscosity, which is very low compared to solvents usually used (1.07 mPa.s at 25°C)[35] These figures are only guidelines taken from the base solvents, and a full rheological characterisation is required to determine accurate surface energy and viscosity measurements. Jang *et al* reported a drastic lowering of the Z value of Ethanol based inks when mixed with ethylene glycol. The calculated Z of 4.74 brings the mixture into the commonly accepted printed range.[36] The reported surface tension values also approach 28 mN m^{-1}, which is a similar value to another well characterised ink, isopropanol (IPA) which is known to print in a very stable manner. The ratio of ethanol ink to ethylene glycol was 4:1, and after this step was taken, the ink was found to form stable droplets, similar to the previous NMP test.

The DMSO ink largely printed without need for much modification, using similar parameters to that of the NMP ink. The surface energies (43.54 mN m^{-1} and 40.79 mN m^{-1})[37] and viscosities (1.996 mPa.s and 1.65 mPa.s)[38] of both solvents are quite close, and so it would be expected that the inks would print in a similar manner. Some tuning was required to reduce satellite droplet formation and it should be noted that over long printing times, the DMSO ink appeared to clog or jam the print head faster than the NMP based inks did.

The final organic ink, DMF based was eventually printed although with low quality droplets. The low viscosity of this solvent (0.92 mPa.s) makes stable droplet formation very difficult. High driving voltages are required to generate stable droplets, and even those that are successfully generated are ejected at a much slower velocity than those generated by higher viscosity solvents. The table below gives an outline of the fluid properties of the solvents used in the initial printing tests.

Table 5.1: Summary of the physical properties and Inverse Ohnesorge number of each of the carrier solvents used for MXene inks in this work

Solvent	Density ($kg\ m^{-3}$)	Surface Energy ($mN\ m^{-1}$)	Viscosity (mPa.s)	Inverse Ohnesorge number (Z)
NMP	1028[39]	40.79[39]	1.65[39]	17.98453
DMSO	1100[40]	43.54[40]	1.996[40]	15.88875
DMF	948[40]	37.10[41]	0.92[42]	29.54017
Ethanol	789[43]	22.10[43]	1.07[43]	17.88383
Ethanol+Ethylene Glycol[44]	866	28.9	4.83	4.746466

It is important to note that these tests were carried out at relatively low ink concentrations (~ $0.1mg\ mL^{-1}$). The solvent exchange method of creating the organic inks means that concentration can be highly variable, depending on how much Organic solvent is added after the re-dispersion. The $Ti_3C_2T_x$ flakes are very stable in NMP, and high concentration inks, over 10 $mg\ ml^{-1}$, can be produced. The viscosity of the NMP based inks has been seen to increase to 12 mPa.s at the highest concentrations produced using this method. This will drastically affect the fluid properties of the ink, particularly the viscosity. These tests can be considered preliminary and a full treatment of the fluid properties of organic inks of varying concentrations is necessary.

With the material inks successfully jetted, the next stage of the process is to fabricate devices from each of the inks and to investigate their respective performances.

5.3.2: Substrate selection and device design for printed supercapacitors.

The devices printed for the testing of the performance of the MXene material inks are given in Figure 5.2. The pattern is a simple construction of a pair of parallel current collectors with a number of fingers extending from each into the intervening space.

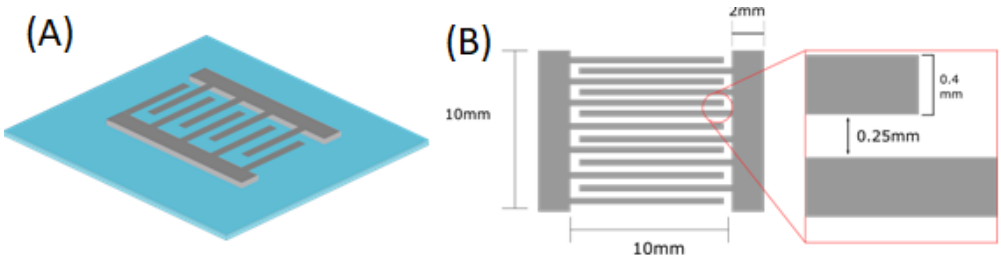

Figure 5.2: Interdigitated devices typical of those used in this work with (A) showing an illustration of the typical device on a substrate and (B) showing a schematic plan of the dimensions of the devices used for electrochemical testing of MXenes.

The dimensions provided in the above figure are the set machine dimensions, i.e the dimensions that the printer is instructed to output from the pattern design file. When actually deposited and measured, features will be larger than these set dimensions due to the spreading of the liquid. This can be controlled by droplet spacing, heating of the substrate and substrate selection, but the total dimensions will usually be slightly larger than those set. The fingers were set at a spacing of 250 µm from one another to provide a good density of interdigitations, which provides a higher power density.[28] If the fingers are placed too close together, shorting may occur when the liquids spread on impact with the substrate

For the initial device characterisations, a flexible AlO_x coated PET substrate was selected. There are a wide range of flexible polymer substrates available, however many have been seen to suffer from producing inconsistent films when used with inkjet printing. The primary reason for using this particular substrate was to achieve homogenous material depositions within the printed patterns. This was to ensure the most efficient use of the area of the device and the material deposited. Coffee staining (detailed in chapter 3) is the primary method through which homogenous deposition in inkjet printed devices is disrupted. The two primary ways to combat this are to use binary solvent systems combining a low and high volatility solvents to reduce the effect of the capillary flow or to use hydrophobic, porous or

patterned substrates to inhibit the initiation of the internal droplet flows and the spreading of the droplet itself.

The AlO_x substrate was used previously in the work of other groups[23,45] and was known to inhibit the effects of coffee staining and droplet spreading on the substrate. For all inks shown in the following tests a droplet spacing of 25 µm was deemed appropriate to form continuous films. This was the maximum spacing with which material could be deposited in a discrete manner. While lower spacing could provide a higher mass per printed pass, there was certain concern with this approach due to the high boiling point of the solvents being used. NMP, DMSO and DMF have boiling points of 202, 188, and 153 degrees ^{o}C respectively.[40,46,47] When low volatility solvents are used to print with very low droplet spacings, rather than forming distinct patterns, as the next layer is being deposited onto a system that is still wet or in the process of drying, the material can pool into larger droplets rather than forming the ordered pattern.

5.3.3: Printing and electrochemical testing of MXene inks

The AlO_x -coated PET was secured to the printer platen and the selected patterns were deposited with 25 print passes in total. The driving voltage was set to 16 V for all nozzles with the print height set to 250 µm and the droplet spacing set to 25 µm. The print platen was heated to 60^{o}C in order to aid drying, and 2 minutes delay was set between each printed layer of the device. An example of the printed devices is given in the figure below. The devices were left to dry on the platen for 3-4 hours in order to evaporate solvent. Ideally before testing there would be no solvent remaining within the devices, and to achieve this the devices would be baked. However the T_g, the glass transition temperature, of the coated PET (60 to 81^{O}C)[48,49] is far lower than the boiling point of all the organic solvents, with the exception of ethanol.

After drying to ensure the removal of most of the solvent, a H_2SO_4-PVA electrolyte was drop cast onto the device and spread to and even thickness. This was then covered with a strip of PET and the PVA was allowed to dry. Each device was cycled at a set of increasing scan rates from 10 mV s^{-1} to 1 V s^{-1} between 0 V and 0.5 V. The CV curves for these tests are given in Figure 5.3.

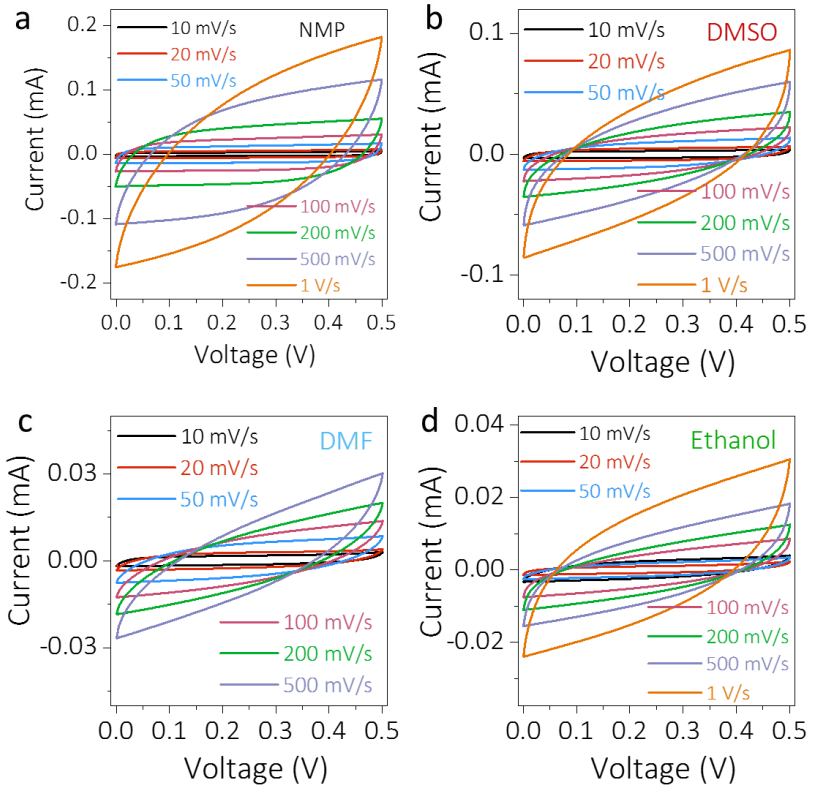

Figure 5.3: CV curves of printed devices with increasing scan rate for inks dispersed in (a) NMP, (b) DMSO, (c) DMF and (d) Ethanol.

A semi rectangular shape in the lower scan rate CV curves can be clearly seen, with the NMP and DMSO ink devices performing well up to the 200 mV s^{-1} scan rate. The rectangular shape exhibited by the curves at these scan rates show the devices are indeed functioning and exhibiting characteristic supercapacitive behaviour. Above 200 mV s^{-1} resistive behaviour is seen as the CV deviates from the semi-rectangular shape into a skewed shape associated with standard ohmic behaviour. Comparatively, the DMSO and NMP based inks provide the best current responses, with the NMP based ink showing the best overall performance. In addition to this, the NMP device appeared to be able to sustain higher scan rates than some of the others. The 500 mV s^{-1} scan for the NMP based device retained some of the rectangular characteristics before breaking down into a completely resistive response. The curves themselves are largely symmetric on charge and discharge, exhibiting no peaks or deviations, showing that the storage is highly reversible in this instance.

The rate dependence can be further examined by examining the changes in capacity as a function of scan rate as shown for the four different solvents in Figure 5.4.

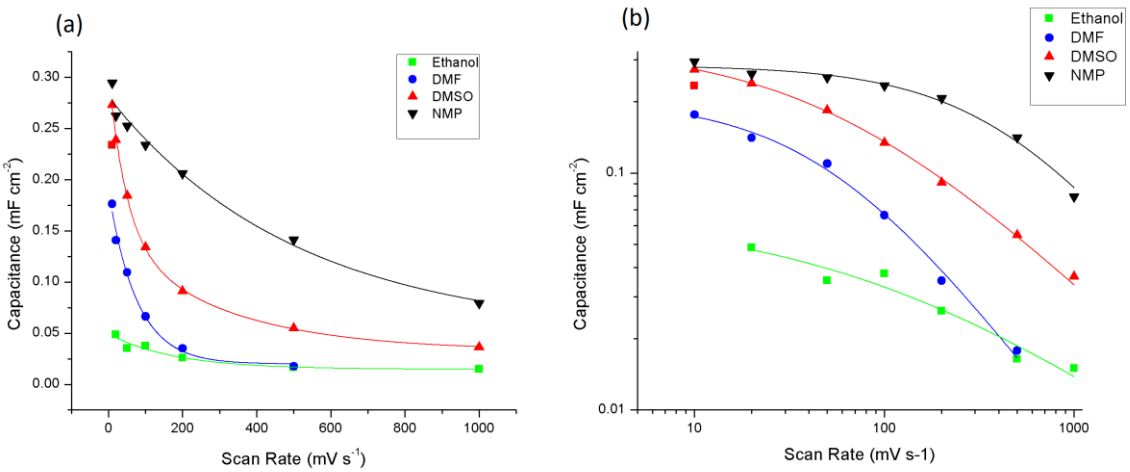

Figure 5.4: Areal capacitance as a function of scan rate (a) and a log-log plot of the areal capacitance versus scan rate (b).

The capacitance values for the DMSO and NMP inks begin at a similar level, with the DMSO devices rapidly falling off as the rate increases. NMP devices display the best rate performance of those tested. The rate has only a small effect on the Ethanol ink devices due mainly to the very small initial capacitance. The DMF ink devices show a lower initial capacitance than the NMP and DMSO which also rapidly falls away with increasing voltage rate. The NMP based devices retains 0.2 mF cm^2 by 200 mV s^{-1} compared to a value 0.0915 mF cm^{-2} compared to DMSO, the next best performing ink.

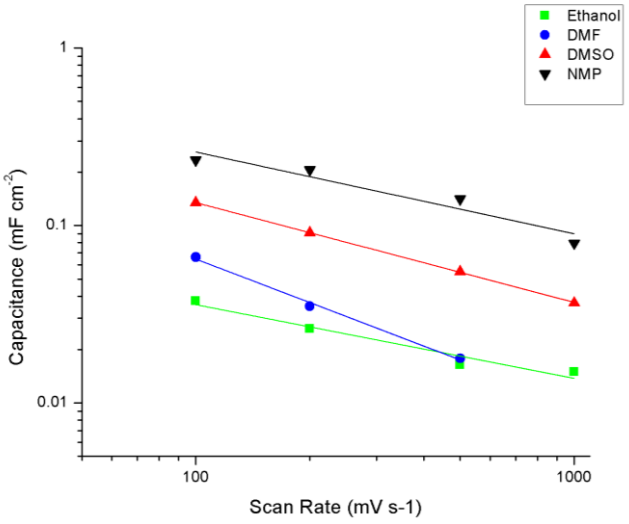

Figure 5.5: Log-Log graph of areal capacitance versus scan rate for printed devices at high scan rates.

A more informative view on how the capacitance changes with rate can be seen from the log-log plot in Figure 5.4 (b), and when the decay of capacitance is examined at high scan rates, as shown in Figure 5.5.

At high scan rates, the scan rate is seen to decay in a linear fashion, with the slope of these line calculated to be -0.46±0.09 for NMP, -0.4156±0.06 for Ethanol, -0.5628±0.0047 for DMSO and -0.81374± 0.05 for DMF. It is known that at high scan rates where areal capacitance is limited by ionic diffusion[50,51], $C/A \propto dV/dt^{-1/2}$. This is the behaviour that appears to be exhibited in the devices fabricated from NMP, Ethanol, and DMSO based inks. Interestingly the DMF ink devices sit between the expected slope ranges for determining ionic or resistance limiting behaviour, although it should be noted that the data set for these devices contain fewer points due to the failure of the devices at higher scan rates.

The observed response of the ethanol-based ink was low compared to the NMP (max current reached in non-resistive tests ~0.01 mA) but still remains of interest for a few reasons. The first reason is the ease with which ethanol is evaporated. Residual solvent remaining in the devices will affect the conductivity of the electrodes. This is particularly detrimental in a single material device such as the ones printed here where the material is functioning both as the charge storage medium and the current collector. While the Ethylene glycol additive does have a higher boiling point than the base ethanol solvent (198°C)[52] it forms only part of the dispersion and would still constitute a smaller amount of leftover solvent than the other inks. The second reason for retaining Ethanol as a candidate is due to its relative non-toxicity. NMP is known to cause developmental issues in offspring with repeated exposures to the parent [53,54], DMF is well known to cause severe liver toxicity and is a carcinogen.[55,56] DMSO is slightly different insofar as that it only causes mild skin irritation and remains non-toxic at low volumes[57], however it is very effective at penetrating cells and is often used as a drug delivery solvent in the pharmaceutical industry. This means that exposure to a DMSO based ink can carry the material within the ink through the skin and into the cells/bloodstream.[58,59]

While the highest performing device is usually the aim in materials science and energy storage, it is not always necessarily the best option. The advantage of this process is the ability to upscale and the ease of manufacture. Many of the potential uses for devices such as those shown in Figure 5.3 will be for applications requiring low energy but high power, such as in wearables, electronics integrated into fabrics

or in food packaging. In these situations, where very high energies and currents are not necessarily needed, and where the device itself is intended to be mass produced and disposed of, poorer performing devices but with much lower environmental and human impact would be preferred.

With NMP based inks initially selected as the best performing inks, a full characterisation of conductivity and thickness profiles of the materials was then conducted to determine the specific electronic and physical properties of the material and the inks.

5.3.4: Performance of devices as a function of deposited layers

By tuning the number of deposited layers for a device, it is expected that the device thickness and conductivity can be adjusted to suit differing power needs or form factors. On inspection with the printer camera and optical microscopes, very little visible coffee staining can be seen on the printed devices. Despite this, it is unlikely that the coffee staining has been completely suppressed by the AlO_x coated PET. Usually contact profilometry is used to determine the thickness of printed features. This process proved difficult with our chosen substrate. While the coated PET suppresses spreading and coffee staining very well, it does this at the expense of having a very high surface roughness, on the order of 500 nm. This makes discerning the height profiles of nanostructures deposited onto this substrate very difficult. The devices shown previously in Figure 5.3 were printed with the number of successive print passes, N=15. At this thickness the profilometer was not able to accurately determine the height profile of the lines which were obscured by the surface roughness. We can infer from this that the printed patterns were below 500 nm height. A practical issue with determining the height profile of the printed structures is the flexibility of the substrate itself. In order to achieve an accurate measurement, the substrate itself must be spread as flat as possible. While to the human eye it may appear to have been appropriately flattened, this may not be the case on the 10s of nm scale measured by the profilometer.

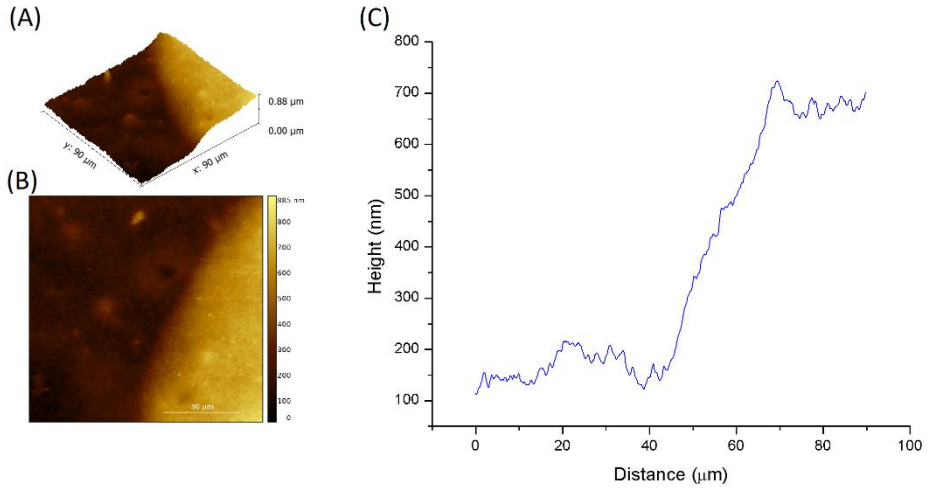

Figure 5.6: AFM scans of printed structured showing (A) an isometric overview of the edge of the printed line (B) a plan view of the area scanned, showing the roughness of the substrate and (C) the line scan through the printed structure. When the base height scanned for the substrate is subtracted from the total height, the structure is found to have a vertical height of 514 nm.

AFM was used to obtain more accurate height profiles of devices. Two devices were prepared for these tests, the first with 15 printed passes as was used for the initial electrochemistry tests and a second thicker device printed with 100 passes. The thicker device yielded a good AFM profile, showing the step height between the substrate and the top of the device being ~514 nm.

Similar scans of thinner devices were difficult to achieve mainly due to the plane correction required. This is largely as a result of the surface not being perfectly flat, a phenomenon that is even more disruptive to accurate measurements in AFM than it is in contact profilometry. In addition to this, the large surface roughness, on the order of 500 nm as measured through contact profilometery makes perfectly accurate height measurements at small number of print passes, *N,* difficult.

As it stands these thickness measurements at the very least infer that the thickness of the standard printed features (N=15 printed passes) is lower than 513 nm measured for the 100 printed passes features. This correlates quite well with the fact that reliable measurements could not be obtained from the profilometer, and that the standard film thickness is much lower than the surface roughness of the substrate itself. Optical and absorption-based methods of thickness determination such as white light interferometry (WLI), optical absorption spectroscopy (OAS) or ellipsometry may more effective means of determining thickness by examining the change in absorption and reflection properties of the material with increasing

deposited layers. In addition, more detailed AFM studies are required to obtain an accurate and reliable relationship between the printed film thickness and the number of printed passes. This will also entirely depend on the chosen concentration of ink, with NMP inks being stable enough to easily change the concentration through the adding of solvent or the removing of solvent during the solvent exchange process.

The effect of print pass number *(N)* for the NMP based ink was examined, and the resulting curves are given in Figure 5.7.

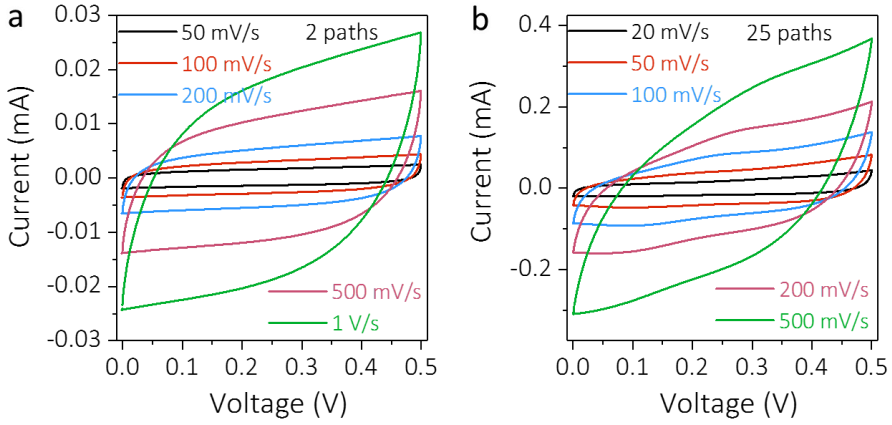

Figure 5.7: CV curves showing (a) the electrochemical response of a device fabricated with 2 printed passes of MXenes in NMP and (b) the response from a device fabricated from 25 printed passes.

The number of print passes drastically affects the current response of the devices. At *N*=2, the device shows a very similar response to those seen in the poorer performing inks in Figure 5.3, Ethanol-Ethylene Glycol and DMF. When the 500 mV s^{-1} curve in Figure 5.7 (b) is compared to the equivalent curve from Figure 5.3 (a), it is clear that the onset of resistive behaviour observed in the device occurs at a lower scan rate with a high value of *N* but both devices display a similar current response at the point that resistive behaviour is first observed (~0.1 mA).

The rate response of both the 2 printed pass and the 25 printed pass can also be examined in a similar manner to the devices prepared from different solvents. As seen in Figure 5.8, the areal capacitance decreases with increasing scan rate for both 2 pass and 25 pass devices. The decline in the 25 pass devices is slower than that of the 2 pass devices, with significant decline only beginning at scan rates higher than 100 mVs^{-1}

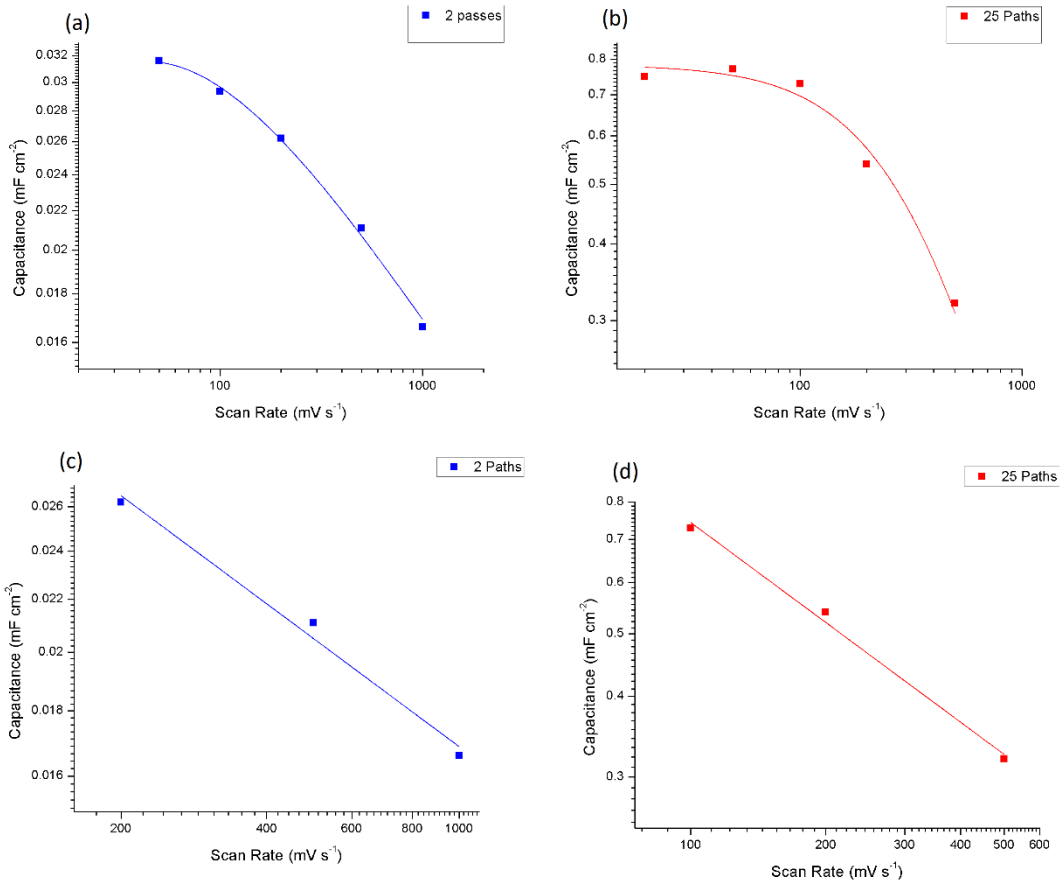

Figure 5.8: Log-log scale graphs showing rate dependence of (a) a two pass devices, (b) a 25 pass device, (c) a 2 pass devices at high scan rate and (d) a 25 pass device at high scan rate.

As observed in the tests conducted on devices fabricated from differing carrier inks, the relationship between log C (mF cm^{-2}) and log ΔV (mV s^{-1}) is linear at high scan rates indicating the influence of a power law. The slope of the linear graph sections is found to be -0.28 for the 2 path devices, and -0.5137 for 25 passes. This indicates diffusion limitations in the higher pass devices are the dominating effect on rate performance, although it is unclear how the rate performance is being affected in the lower pass devices. Resistance limitations are known to be demonstrated by a slope value of -1 from this type of plot.[50]

The conductivity of electrodes depending on N was also investigated, to see if material conductivity may play a part in this process. IV response of lines of varying N and their sheet resistance were calculated, as shown in Figure 5.9.

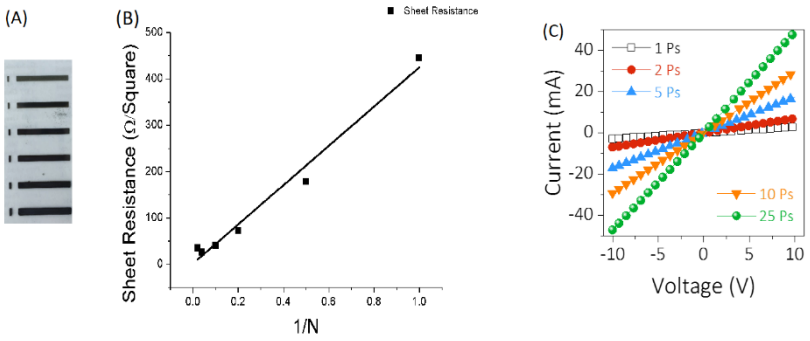

Figure 5.9: (A) Conductive tracks of increasing thicknesses printed to examine (B) sheet resistance as a function of number of printed layers and (C) how the IV response differs with number of printed layers N

The sheet resistance of MXene printed lines show the characteristic proportionality to the inverse of number of passes, $R_S \propto \frac{1}{N}$. The tests shown in both Figure 5.5 and Figure 5.6 suggest that that purely increasing the mass/thickness of the device is not necessarily the best method by which to improve the efficiency of energy storage. The resistive behaviour shown at increasing scan rates indicates limitations imposed by electron transport through the material or ion diffusion. The loss of medium and high rate capacity is a typical phenomenon observed in pseudo- and supercapacitive materials, since at higher rates the potential drop across the electrode due to the resistance of the material is higher. This restricts active material utilisation to a finite volume of active material around the current collector.[60,61] It is unknown how pronounced this particular effect is in this system due to the fact that the current collector is also functioning as the active material. As seen from the high rate graphs in both Figures 5.5 and 5.8, the slopes suggest the limitation in this case is that of ion diffusion. El Kady *et al* suggest that for interdigitated supercapacitor devices, maximising the number of fingers per unit area (in this case, resulting in narrower fingers with a smaller gap between them) results in a minimisation of the mean ionic diffusion length and increasing the amount of material exposed to the electrolyte.[28]

Nonetheless, the areal capacitance measured for the cells was impressive with the *N*=2 device showing an areal capacitance of 1.3 mF cm^{-2} and *N*=25 device showing an areal capacitance of 12 mF cm^{-2}. These values compare very favourably with similarly fabricated devices in recent publications.[62–64] While the capacitance values are very promising, one of the real advantages to this process is the ease and flexibility of the fabrication process. With the inkjet printing process, the design of

the devices can be changed very easily. The line width and line spacing can be very easily lowered, which if the process is indeed limited by some ionic diffusion, should increase the material utilisation and allow for higher rate capacity. This flexibility of device design is lacking in subtractive manufacturing methods such as photolithography and is difficult to achieve even in multiplanar printed devices.

5.3.5 Printed devices as part of a larger circuit and the effect of different substrates

To investigate how the printed devices would perform when deposited as part of a larger circuit, a set of four devices in parallel and in four devices in series were also produced in the same manner as before. Devices connected in series have the effect of broadening the voltage window that can be used the charge and discharge. This is of interest in this case as the voltage operating window of the symmetric MXene devices is quite low. One of the simplest methods by which the energy stored can be increased is by extending the voltage window. If the situation requires it, parallel devices can deliver a higher current response. The electrochemical responses of both sets of linked devices is given in Figure 5.7 below.

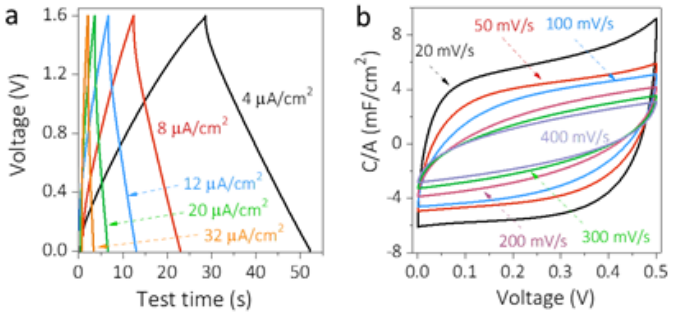

Figure 5.10: The electrochemical response of multiple devices printed as part of a larger circuit showing (a) the larger voltage window of 4 printed devices in series and (b) the normalised CV curve of 4 printed devices in parallel

Figure 5.10 (a) shows the Galvanostatic Charge-Discharge (GCD) curve for the 4 devices printed in series. It shows the broader Voltage window, operating effectively up to 1.6 V and demonstrating the reversible charge-discharge desired in a supercapacitive device. The normalised CV curves in Figure 5.10 (b) show us the characteristic square shapes are retained by the devices when printed in series. What these tests essentially underline is the flexibility of the process.

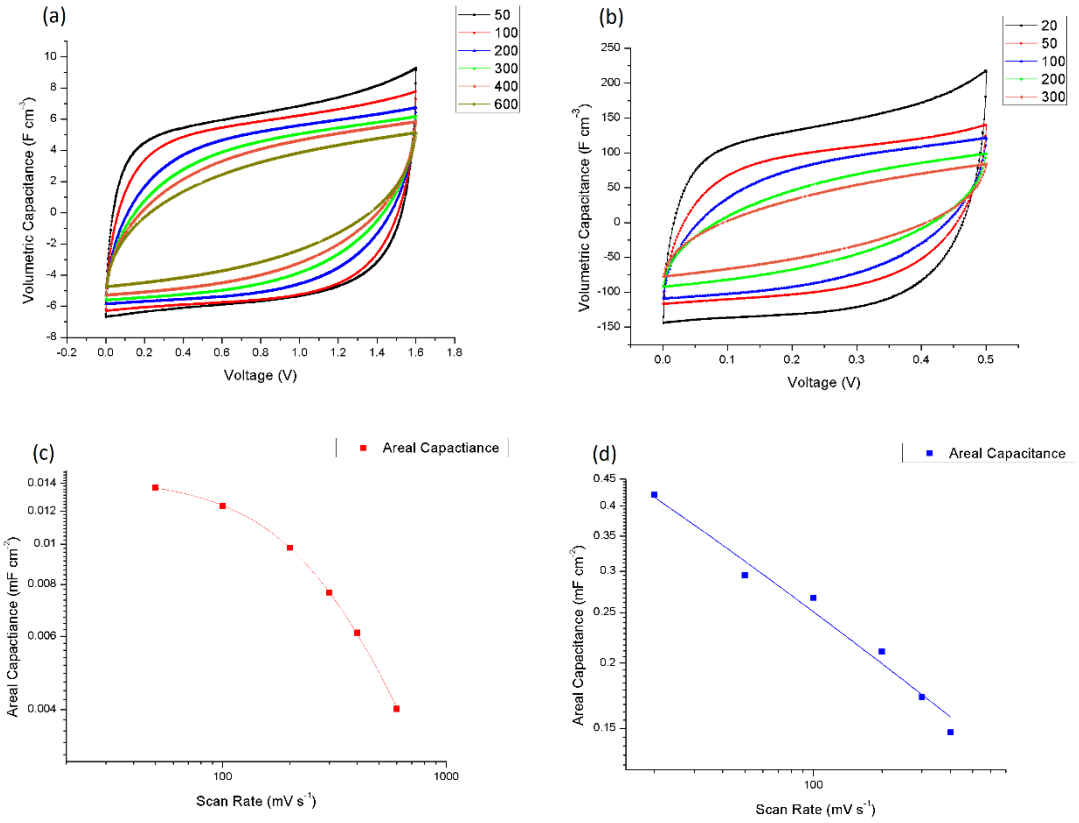

Figure 5.11: Graphs showing (a) the Volumetric capacitance of four devices in series at increasing scan rates, (b) the volumetric capacitance of four devices in parallel with increasing scan rates, (c) the rate performance of four devices in series and (d) the rate performance of four devices in parallel.

As seen in the graphs presented in Figure 5.11, when connected in series the devices maintain a reasonable volumetric capacitance over a much larger voltage window, while maintaining a similar rate performance to the standard single printed devices. When connected in parallel, the volumetric capacitance can be increased dramatically due to higher possible currents, although seemingly at the expense of some rate performance, as seen in Figure 5.11 (d). This further underlines the flexibility of this process as an approach for fabricating energy storage devices for a range of applications.

Devices can be easily fabricated in configurations that suit the specific need of the system in question, be it low form factor, high current or wider voltage windows. In addition, it shows that it is simple to fabricate larger circuits and devices using just inkjet printed components. The next step in this process is to attempt a fully printed integrated circuit. This can be achieved quite simply by swapping out the MXene inks and replacing them with insulating, or metallic inks where required.

A final test conducted was to see the compatibility of the printing process developed for MXene inks using different substrates. MXene devices were printed in the same manner as before on glass, untreated PET and Kapton. The resulting devices all displayed wetting issues and in-homogenous films not seen with the features printed on the coated PET. Wetting on glass was expected to be inconsistent and to display a high degree of coffee staining however, the difficulty in printing homogenous films on the PET and Kapton substrates was unexpected. While coffee staining on Kapton was not pronounced, a droplet spacing could not be reached where droplets did not pool and form disconnected patterns. This resulted in some of the printed fingers within the device being disconnected from the rest of the current collector.

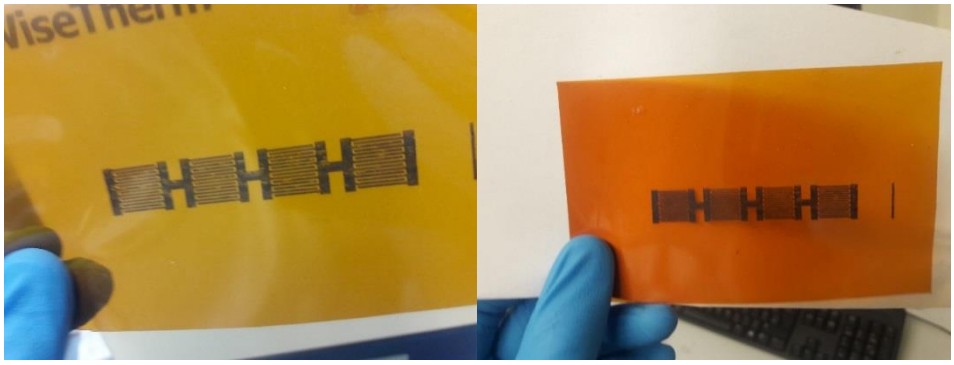

Figure 5.12: Sheet of Kapton with printed devices in series. As can be seen, the material is not deposited in a homogenous manner. While coffee staining effect does not disrupt the feature formation, the fingers and electrodes are still inconsistent and in places do not form fully connected films.

To combat the coffee staining and in-homogenous deposition seen on different substrates adjustments to the composition of inks must be made. The primary method of inhibiting coffee staining is by dispersing the material in a binary solvent suspension.[65–67] Despite the in-homogenous films produced, printing on Kapton continues to be an important goal due to its high thermal stability (T_g= 360 – 410 ^{O}C). This would allow for the printing of MXene devices alongside materials that require thermal treatment, such as metallic nanoparticle inks that require sintering to achieve higher conductivity. This would present MXenes as a material suitable for use both in single systems and in multi material systems, increasing their flexibility of use.

5.4 Multi-material printed systems for supercapacitors and circuits

While the previous section has demonstrated the effectiveness and versatility of MXenes as a current collector/active material in supercapacitor electrodes, it is not the only material that printed circuits and devices can be printed with. Different device and circuit demands will require different material combinations to meet them. One of the primary advantages of the additive manufacturing approach that Inkjet printing allows is the rapid swapping in and out of materials within a single printed device architecture. Different materials in different parts of a device or circuit is a simple matter of changing the pattern design and changing ink cartridges.

MXenes, as mentioned previously, display very high conductivity. This conductivity is high enough for the material to function both as a current collector and as the charge storing active material; however this is not the case for several active materials used in both battery and supercapacitors (Si, $LiFePO_4$, MnO_2). These materials therefore require a conductive current collector for the device to function effectively. Much as for MXenes, the best-case scenario is one where both current collector and active material can be printed directly onto flexible substrates in an easily changed pattern.

Initially, a highly concentrated Ag nanoparticle ink (Sigma Aldrich, Silver nanoparticle dispersion, 30-35 wt % in triethyleneglycol monomether ether) designed specifically for inkjet printing was selected as a current collector. This approach encountered difficulties however. For the Ag nanoparticles to achieve the desired conductivity, they must be sintered, ideally at a temperature $\geq 200\ ^{O}C$ but at a minimum of $100^{O}C$. This far exceeds the thermal stability of the substrates (PET and coated PET) that were to be used in testing.

The second obstacle encountered was in-homogenous printing of active material on top of the silver lines. The silver printed features displayed large print heights in comparison to other printed materials. At N=2 for silver, the height was measured to be 1300 nm by profilometry. When active material was deposited on these

features, most material migrated towards the edges of the Ag lines, at the contact point of the Ag and the substrate. It is unknown if this effect is caused by a mismatch in surface energies of the droplet containing the active material and the Ag tracks or is purely caused by the morphology of the printed lines. Regardless of the cause of this phenomenon, the effect is to limit the amount of active material in contact with the current collector and limit the used surface area of the devices. While an easy way to combat this effect would be to print the MnO_2 first, with the silver placed on tope, this would also limit the contact area between active material and electrolyte.

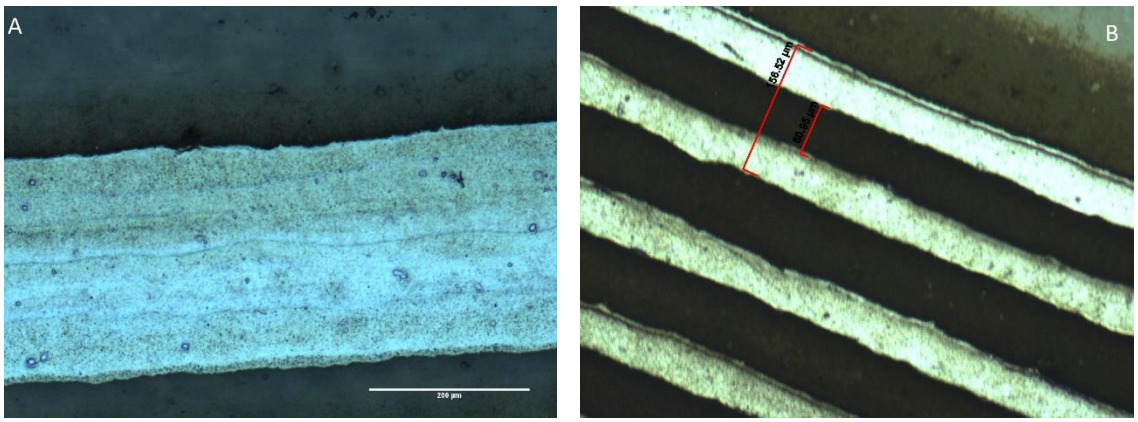

Figure 5.13: Ag printed lines on coated PET, with (A) showing MnO2 printed selectively on the printed line. The darker line at the Ag-substrate interface shows where the MnO2 has accumulated off the silver line. Image (B) shows a thicker layer of MnO2 deposited across the entirety of the device. Despite this, the material still does not adhere to the Ag lines and largely accumulates in the interstitial regions between the fingers.

As such different electrode materials were to be investigated. Maintaining a solution processed approach for ink formulation, the most promising current collector materials stand as graphene and carbon nanotubes (CNTs). Ideally conductive materials would be deposited in interdigitated patterns as before with active material (MnO_2 in this case) deposited in a thin layer on top of the current carrying electrodes. As has been seen from the initial tests with printed Ag inks, the morphology of the current collector is an important consideration for the final performance of the device. It is hoped that by using materials that form thin films, and have similar surface energies that thin, homogenous layers of both conducting and active materials can be deposited, although this is a process that needs a great deal of further work.

5.5 Conclusions

NMP based MXene inks have been shown to produce high quality planar energy storage devices that can be fabricated rapidly. A simple interdigitated device printed on a flexible coated PET substrate demonstrated excellent charge storage properties, with a 25 print pass device displaying an areal capacitance of 12 mF cm^{-2}. Despite the lack of metallic current collector and the interdigitated nature of the devices, the rate performance was found to be diffusion, rather than resistance limited in almost all cases. The device performances was further demonstrated when placed in series or in parallel with other printed components, verifying their effectiveness for use in larger integrated and printed circuitry. While the electric performance of the devices is important, the simplicity of the process should also not be overlooked. One of the primary advantages demonstrated in this work, is the ability to very quickly print devices that require only a single material and electrolyte to function. No further intensive chemical or thermal treatments are required. Utilising high concentration inks, devices can be printed with only 1 or 2 print passes, meaning the process is not only simple, it is also rapid. Furthermore, inks based on more environmentally friendly solvents that are less dangerous and cheaper were also utilised to create devices. While these inks do display decreased performance, they are nonetheless ideal for applications requiring lower power and energy outputs where people may be exposed to the device itself, such as in clothing or in food packaging.

Further engineering of the device parameters is predicted to yield higher power and energy densities by adjusting interdigitated finger thickness and separation. Inkjet printing, as an additive manufacturing process, allows for these parameters and the overall device structure to be easily changed and allow the devices produced to fit a range of morphologies depending on the intended use.

Bibliography

1. Yan, H. *et al.* A high-mobility electron-transporting polymer for printed transistors. *Nature* **457,** 679–686 (2009).

2. Chen, P. *et al.* Fully printed separated carbon nanotube thin film transistor circuits and its application in organic light emitting diode control. *Nano Lett.* **11,** 5301–5308 (2011).

3. Beecher, P. *et al.* Ink-jet printing of carbon nanotube thin film transistors. *J. Appl. Phys.* **102,** 1–7 (2007).

4. Lee, D.-H., Han, S.-Y., Herman, G. S. & Chang, C. Inkjet printed high-mobility indium zinc tin oxide thin film transistors. *J. Mater. Chem.* **19,** 3135 (2009).

5. Kelly, A. G. *et al.* All-printed thin-film transistors from networks of liquid-exfoliated nanosheets. *Science (80-.).* **356,** 69–73 (2017).

6. Lu, H. *et al.* Inkjet printed silver nanowire network as top electrode for semi-transparent organic photovoltaic devices. *Appl. Phys. Lett.* **106,** 093302 (2015).

7. Hu, G. *et al.* Black phosphorus ink formulation for inkjet printing of optoelectronics and photonics. *Nat. Commun.* **8,** 278 (2017).

8. Jung, J., Kim, D., Lim, J., Lee, C. & Yoon, S. C. Highly efficient inkjet-printed organic photovoltaic cells. *Jpn. J. Appl. Phys.* **49,** 05EB03 (2010).

9. Cherian, D., Mitra, K. Y., Hartwig, M., Malinowski, P. E. & Baumann, R. R. Fabrication of organic photo detectors using inkjet technology and its comparison to conventional deposition processes. *IEEE Sens. J.* **18,** 94–105 (2018).

10. Koppens, F. H. L. *et al.* Photodetectors based on graphene, other two-dimensional materials and hybrid systems. *Nat. Nanotechnol.* **9,** 780–793 (2014).

11. Hoth, C. N., Choulis, S. A., Schilinsky, P. & Brabec, C. J. High photovoltaic performance of inkjet printed polymer:Fullerene blends. *Adv. Mater.* **19,** 3973–3978 (2007).

12. Wu, Z. S., Parvez, K., Feng, X. & Müllen, K. Graphene-based in-plane micro-supercapacitors with high power and energy densities. *Nat. Commun.* **4,** 2487 (2013).

13. Pandolfo, A. G. & Hollenkamp, A. F. Carbon properties and their role in supercapacitors. *J. Power Sources* **157,** 11–27 (2006).

14. Tehrani, Z. *et al.* Large-area printed supercapacitor technology for low-cost domestic green energy storage. *Energy* **118,** 1313–1321 (2017).

15. Zhong, C. *et al.* A review of electrolyte materials and compositions for electrochemical supercapacitors. *Chem. Soc. Rev.* **44,** 7484–7539 (2015).

16. Chen, P., Chen, H., Qiu, J. & Zhou, C. Inkjet printing of single-walled carbon nanotube/RuO2 nanowire supercapacitors on cloth fabrics and flexible substrates. *Nano Res.* **3,** 594–603 (2010).

17. Ervin, M. H., Le, L. T. & Lee, W. Y. Inkjet-printed flexible graphene-based supercapacitor. *Electrochim. Acta* **147,** 610–616 (2014).

18. Le, L. T., Ervin, M. H., Qiu, H., Fuchs, B. E. & Lee, W. Y. Graphene supercapacitor electrodes fabricated by inkjet printing and thermal reduction of graphene oxide. *Electrochem. commun.* **13,** 355–358 (2011).

19. Xu, Y. *et al.* Inkjet-printed energy storage device using graphene/polyaniline inks. *J. Power Sources* **248,** 483–488 (2014).

20. Van Osch, T. H. J., Perelaer, J., De Laat, A. W. M. & Schubert, U. S. Inkjet printing of narrow conductive tracks on untreated polymeric substrates. *Adv. Mater.* **20,** 343–345 (2008).

21. Pech, D. *et al.* Elaboration of a microstructured inkjet-printed carbon electrochemical capacitor. *J. Power Sources* **195,** 1266–1269 (2010).

22. Kim, J., Kumar, R., Bandodkar, A. J. & Wang, J. Advanced Materials for Printed Wearable Electrochemical Devices: A Review. *Adv. Electron. Mater.* **3,** 1600260 (2017).

23. Finn, D. J. *et al.* Inkjet deposition of liquid-exfoliated graphene and MoS<inf>2</inf> nanosheets for printed device applications. *J. Mater. Chem. C* **2,** 925–932 (2014).

24. Torrisi, F. & Coleman, J. N. Electrifying inks with 2D materials. *Nat. Nanotechnol.* **9,** 738–739 (2014).

25. Torrisi, F. *et al.* Inkjet-printed graphene electronics. *ACS Nano* **6,** 2992–3006 (2012).

26. Wang, X. *et al.* Three-Dimensional Hierarchical GeSe $_2$ Nanostructures for High Performance Flexible All-Solid-State Supercapacitors. *Adv. Mater.* **25,** 1479–1486 (2013).

27. Zhao, X. *et al.* Carbon nanosheets as the electrode material in supercapacitors. *J. Power Sources* **194,** 1208–1212 (2009).

28. El-Kady, M. F. & Kaner, R. B. Scalable fabrication of high-power graphene micro-supercapacitors for flexible and on-chip energy storage. *Nat. Commun.* **4,** 1475 (2013).

29. Chmiola, J., Largeot, C., Taberna, P.-L., Simon, P. & Gogotsi, Y. Monolithic carbide-derived carbon films for micro-supercapacitors. *Science* **328,** 480–3 (2010).

30. Sun, G. *et al.* Layer-by-layer printing of laminated graphene-based interdigitated microelectrodes for flexible planar micro-supercapacitors. *Electrochem. commun.* **51,** 33–36 (2015).

31. Peng, L. *et al.* Ultrathin Two-Dimensional MnO $_2$ /Graphene Hybrid Nanostructures for High-Performance, Flexible Planar Supercapacitors. *Nano Lett.* **13,** 2151–2157 (2013).

32. Zhang, C. J. *et al.* Transparent, Flexible, and Conductive 2D Titanium Carbide (MXene) Films with High Volumetric Capacitance. *Adv. Mater.* **29,** 1702678 (2017).

33. Lukatskaya, M. R. *et al.* Cation intercalation and high volumetric

capacitance of two-dimensional titanium carbide. *Science (80-.).* **341,** 1502–1505 (2013).

34. Maleski, K., Mochalin, V. N. & Gogotsi, Y. Dispersions of Two-Dimensional Titanium Carbide MXene in Organic Solvents. *Chem. Mater.* **29,** 1632–1640 (2017).

35. Derby, B. Additive Manufacture of Ceramics Components by Inkjet Printing. *Engineering* **1,** 113–123 (2015).

36. Jang, D., Kim, D. & Moon, J. Influence of Fluid Physical Properties on Ink-Jet Printability. *Langmuir* **25,** 2629–2635 (2009).

37. Surface Tension of N-Methyl-2-pyrrolidone from Dortmund Data Bank. at <http://www.ddbst.com/en/EED/PCP/SFT_C284.php>

38. Dynamic Viscosity of N-Methyl-2-pyrrolidone from Dortmund Data Bank. at <http://www.ddbst.com/en/EED/PCP/VIS_C284.php>

39. 1-Methyl-2-pyrrolidinone, anhydrous, 99.5% | C5H9NO | Sigma-Aldrich. at <https://www.sigmaaldrich.com/catalog/product/sial/328634?lang=en&region=IE>

40. DIMETHYL SULFOXIDE | CAMEO Chemicals | NOAA. at <https://cameochemicals.noaa.gov/chemical/8559>

41. Surface tension values of some common test liquids for surface energy analysis. at <http://www.surface-tension.de/>

42. N,N-Dimethylformamide (DMF) Dynamic Viscosity - SpringerMaterials. at <https://materials.springer.com/thermophysical/docs/vis_c72>

43. ETHANOL | CAMEO Chemicals | NOAA. at <https://cameochemicals.noaa.gov/chemical/667>

44. Jang, D., Kim, D. & Moon, J. Influence of fluid physical properties on ink-jet printability. *Langmuir* **25,** 2629–2635 (2009).

45. Kelly, A. G., Finn, D., Harvey, A., Hallam, T. & Coleman, J. N. All-printed capacitors from graphene-BN-graphene nanosheet heterostructures. *Appl. Phys. Lett.* **109,** 023107 (2016).

46. N,N-DIMETHYLFORMAMIDE | CAMEO Chemicals | NOAA. at <https://cameochemicals.noaa.gov/chemical/3271>

47. MSDS - 1437202. at <https://www.sigmaaldrich.com/MSDS/MSDS/DisplayMSDSPage.do?country=IE&language=en&productNumber=1437202&brand=USP&PageToGoToURL=https%3A%2F%2Fwww.sigmaaldrich.com%2Fcatalog%2Fsearch%3Fterm%3DNMP%26interface%3DAll%26N%3D0%26mode%3Dpartialmax%26lang%3Den%26r>

48. Wang, Y., Wang, W., Zhang, Z., Xu, L. & Li, P. Study of the glass transition temperature and the mechanical properties of PET/modified silica nanocomposite by molecular dynamics simulation. *Eur. Polym. J.* **75,** 36–45 (2016).

49. Chen, D. & Zachmann, H. G. Glass transition temperature of copolyesters of PET, PEN and PHB as determined by dynamic mechanical analysis.

Polymer (Guildf). **32,** 1612–1621 (1991).

50. Higgins, T. M. & Coleman, J. N. Avoiding Resistance Limitations in High-Performance Transparent Supercapacitor Electrodes Based on Large-Area, High-Conductivity PEDOT:PSS Films. *ACS Appl. Mater. Interfaces* **7,** 16495–16506 (2015).

51. Bard, A. J. & Faulkner, L. R. *Electrochemical methods : fundamentals and applications*. (Wiley, 2001). at <https://www.wiley.com/en-us/Electrochemical+Methods%3A+Fundamentals+and+Applications%2C+2nd+Edition-p-9780471043720>

52. ETHYLENE GLYCOL | CAMEO Chemicals | NOAA. at <https://cameochemicals.noaa.gov/chemical/8660>

53. Solomon, H. M., Burgess, B. A., Kennedy, G. L. & Staples, R. E. 1-methyl-2-pyrrolidone (nmp): reproductive and developmental toxicity study by inhalation in the rat. *Drug Chem. Toxicol.* **18,** 271–293 (1995).

54. Lee, K. P., Chromey, N. C., Culik, R., Barnes, J. R. & Schneider, P. W. Toxicity of N-methyl-2-pyrrolidone (NMP): teratogenic, subchronic, and two-year inhalation studies. *Fundam. Appl. Toxicol.* **9,** 222–35 (1987).

55. Kim, T. H. & Kim, S. G. Clinical Outcomes of Occupational Exposure to N,N-Dimethylformamide: Perspectives from Experimental Toxicology. *Saf. Health Work* **2,** 97–104 (2011).

56. *Preventing Adverse Health Effects from Exposure to: Dimethylformamide (DMF)*. (1990). doi:10.26616/NIOSHPUB90105

57. Worthley, E. G. & Schott, C. D. The toxicity of four concentrations of DMSO. *Toxicol. Appl. Pharmacol.* **15,** 275–281 (1969).

58. and, A. A. G. & Anwar*, J. Modulating the Structure and Properties of Cell Membranes: The Molecular Mechanism of Action of Dimethyl Sulfoxide. (2007). doi:10.1021/JP073113E

59. Swanson, B. N. Medical use of dimethyl sulfoxide (DMSO). *Rev. Clin. Basic Pharm.* **5,** 1–33

60. Lu, Q., Chen, J. G. & Xiao, J. Q. Nanostructured Electrodes for High-Performance Pseudocapacitors. *Angew. Chemie Int. Ed.* **52,** 1882–1889 (2013).

61. Lanzi, O. & Landau, U. Effect of Sinter Fracture and Ohmic Resistance on Capacity Retention in the Nickel Oxide Electrode. *J. Electrochem. Soc.* **138,** 2527 (1991).

62. Li, L. *et al.* High-Performance Solid-State Supercapacitors and Microsupercapacitors Derived from Printable Graphene Inks. *Adv. Energy Mater.* **6,** 1600909 (2016).

63. Li, J. *et al.* Scalable Fabrication and Integration of Graphene Microsupercapacitors through Full Inkjet Printing. *ACS Nano* **11,** 8249–8256 (2017).

64. Wang, Y., Zhang, Y.-Z., Dubbink, D. & ten Elshof, J. E. Inkjet printing of δ-MnO2 nanosheets for flexible solid-state micro-supercapacitor. *Nano Energy*

49, 481–488 (2018).

65. Liu, Y., Cui, T. & Varahramyan, K. All-polymer capacitor fabricated with inkjet printing technique. *Solid. State. Electron.* **47,** 1543–1548 (2003).

66. Sefiane, K. Patterns from drying drops. *Adv. Colloid Interface Sci.* **206,** 372–381 (2014).

67. Park, J. & Moon, J. Control of colloidal particle deposit patterns within picoliter droplets ejected by ink-jet printing. *Langmuir* **22,** 3506–3513 (2006).

Chapter 6: Conclusions, outcomes and future work

In-situ TEM electrochemistry is a technique that can offer vital insights into how materials that are used in battery and supercapacitor systems store energy. How these materials change during the charging and discharging process is important for improving upon them. Information gathered during *in-situ* testing can help develop synthesis procedures, ideal material compositions or device morphologies. It provides a level of information, ranging from simple spectroscopic data to atomic structure changes that few other techniques or methods of analysis can provide. The ability to reasonably simulate the internal structure of an electrode immersed in a liquid electrolyte provides more relevant information on the structural changes that occur than *ex-situ* or *post mortem* testing.

In this work an effective means of depositing electrodes for use in an *in-situ* TEM electrochemistry apparatus was demonstrated. This process was conducted by utilising a combination of solution processed nanomaterial inks and inkjet printing. The liquid phase exfoliated inks allowed for numerous materials to be produced and dispersed in a range of solvents. These materials were then deposited onto the TEM electrochemical cell architecture. Narrow electrodes of active material can be deposited with a high accuracy and repeatability. The versatility of this process lies in the ability to print a very wide range of materials. Previously documented studies have been extremely material limited and forgo composite or mixed materials in their entirety. The inkjet printing approach to fabrication is not limited by these factors, making it an ideal production method for a wide range of electrode materials.

Testing of an MnO_2-graphene hybrid electrode in electrolyte allowed for the imaging of dendritic formations growing from the electrode through liquid and in real time. While the material mass was too low to generate observable CV signals above the base signal of the cell, the observed dendritic growth suggests that even for low mass electrodes the process works effectively. When the same procedure was used with a two-material cell, utilising $LiFePO_4$ and carbon, redox peaks were observed in ex-situ testing. Following on from this result, electrodes of Si nanoparticles with a

counter electrode of $LiFePO_4$ were scanned and imaged. Further work to increase the conductivity and mass is required for those tests.

The initial *in-situ* tests conducted in this work hold immense promise for analysing morphological changes in energy storage material. The process provides an avenue for qualitative electrochemistry and structural analysis of materials that is difficult to replicate by other means. Fundamentally, observing morphological changes, such as dendrite formation, is the primary aim of this work. This process aims help complete our understanding of the dynamic processes that occur within an energy storing system. Materials such as MnO_2 and Si have the potential to massively improve the capacity of devices and perhaps more importantly move the fabrication of batteries and supercapacitors towards a standard where less toxic, expensive and environmentally harmful materials are used. To meet industrial and commercial needs however, the materials still need to be improved. *In-situ* TEM electrochemistry, combined with inkjet printing and solution processed materials stands as a perfect means with which to improve and develop not just the materials detailed in this work but a massive range of nanomaterials.

The latter section of this work focussed on the next step required, once those materials have been optimised and improved. Inkjet printing stands as an effective means of rapidly producing planar energy storage devices on flexible substrates. In addition to this, when appropriate inks are selected, it can be used not just to print discrete devices, but whole integrated circuits. In this work, flexible, planar supercapacitors were produced by inkjet printing from a number of organic solvent-based inks. These devices displayed impressive charge storing ability with a 25 printed pass device with an NMP based ink yielding an areal capacitance of 12 mF cm^{-2}. Increasing amounts of material appear to reach some diffusion limited drop off in rate capability, and so the morphology and design of the devices must be considered to further increase capacity and rate performance

The ability to rapidly print components onto flexible substrates is vital for the production of lightweight storage systems for use in wearables, food packaging or other consumer products. Inkjet-printed MXene supercapacitors provide effective energy storage, in a compact form factor that can be manipulated and bent. The additive nature of Inkjet printing means the design of these devices can be changed for particular power and energy needs or to fit a specific device morphology.

To summarise, the combination of inkjet printing and LPE solution processed material has allowed for the accurate deposition of materials in two very different, but in the end fundamentally linked ways. When deposited on a small scale, on TEM electrochemistry cells, the material can be analysed to learn how changes in structure and chemistry can occur during the lifecycle of the material as it is charged and discharged. This allows for a refinement of material, be it through synthesis, or the addition of other materials to enhance energy storage or conductivity, or mechanical strength. Once the ideal material, or material combinations is found, this same deposition process can then be used to deposit the same inks in full scale, integrated devices.

At its core, this work has aimed to show that it is possible to accurately deposit multi-material systems onto prefabricated TEM cells to be electrochemically cycled within a TEM column. The importance of this process lies in how it can be adapted for different materials. The materials presented here, mainly Si nanoparticles and MnO_2, are just two of a multitude of materials that could be analysed in this manner. With further refinement, this platform can be used to provide accurate electrochemical, physical, and chemical information on a variety of materials. If the material can be dispersed in a solvent and printed, it can be analysed in this system. At this moment in time, the system is imperfect, but work shall continue to realise the potential of this technique as a robust analysis method within the field of energy storage devices.

Outlook and future work

The primary avenue of future experimentation that stems from this work is on materials for use in the *in-situ* TEM apparatus. Conductivity and mass problems inhibited the collection of quantitative electrochemical results in the sections dealing with MnO_2. Despite this, the observation of dendritic growth within the electrolyte represents a significant finding. It is therefore desired to continue these tests to find the root cause of this growth, which is unexpected in a pseudocapacitive system. Window stability has been the primary limiting factor in the length of experiments conducted within the TEM column. However as was seen in the tests for Si NPs, cells can be assembled and viewed in the TEM for up to 5 hours.

Therefore, repeating the measurements that resulted in dendritic growth is desired, potentially then adding more conductive additives to the electrode to increase the material utilisation and observe the potential dendritic growth through the entirety of the cell.

For battery materials, Si remains the primary material of interest at this stage; once again it is believed that the conductivity of the material is a limiting factor, and the primary reason why no volumetric expansion is observed during initial cycling tests. The future approach to imaging the Si particles is to combine them with a conductive additive such as graphene, CNTs or activated carbon. These materials, in addition to a polymer binder, can then be printed and cycled in the hope that the characteristic volumetric expansion can be observed. In addition to this, higher mass electrodes of additive free Si can be deposited and used in conjunction with a thicker spacer layer. While this may inhibit the resolution, it is hoped the higher mass of particles will create a better conducting network and force a larger amount of material into physical contact with the metallic electrode.

For MXene printed devices, the next planned step is to utilise textiles as substrates. While polymer substrates provide flexibility, a full integration of these devices into clothing textiles is the ultimate goal. This would allow for a fully integrated wearable electronic system without the flexibility limitations imposed by the polymer sheets. Work towards larger integrated circuitry on the coated PET shall continue. The devices presented in this work consist of supercapacitors printed in series or in parallel with one another. It is desired to expand this to combining these device with other printed components such as resistors, transistors or photovoltaics to produce fully printed usable circuit systems.

For multi-material devices, graphene and CNT based inks are the primary candidates to be used as current collectors in MnO_2 based pseudocapacitors. A full characterisation of conductivity and the effects on material utilisation are required to determine the amount of conductive material required to allow for a functioning MnO_2 based device.